Strojniški vestnik
Journal of Mechanical Engineering

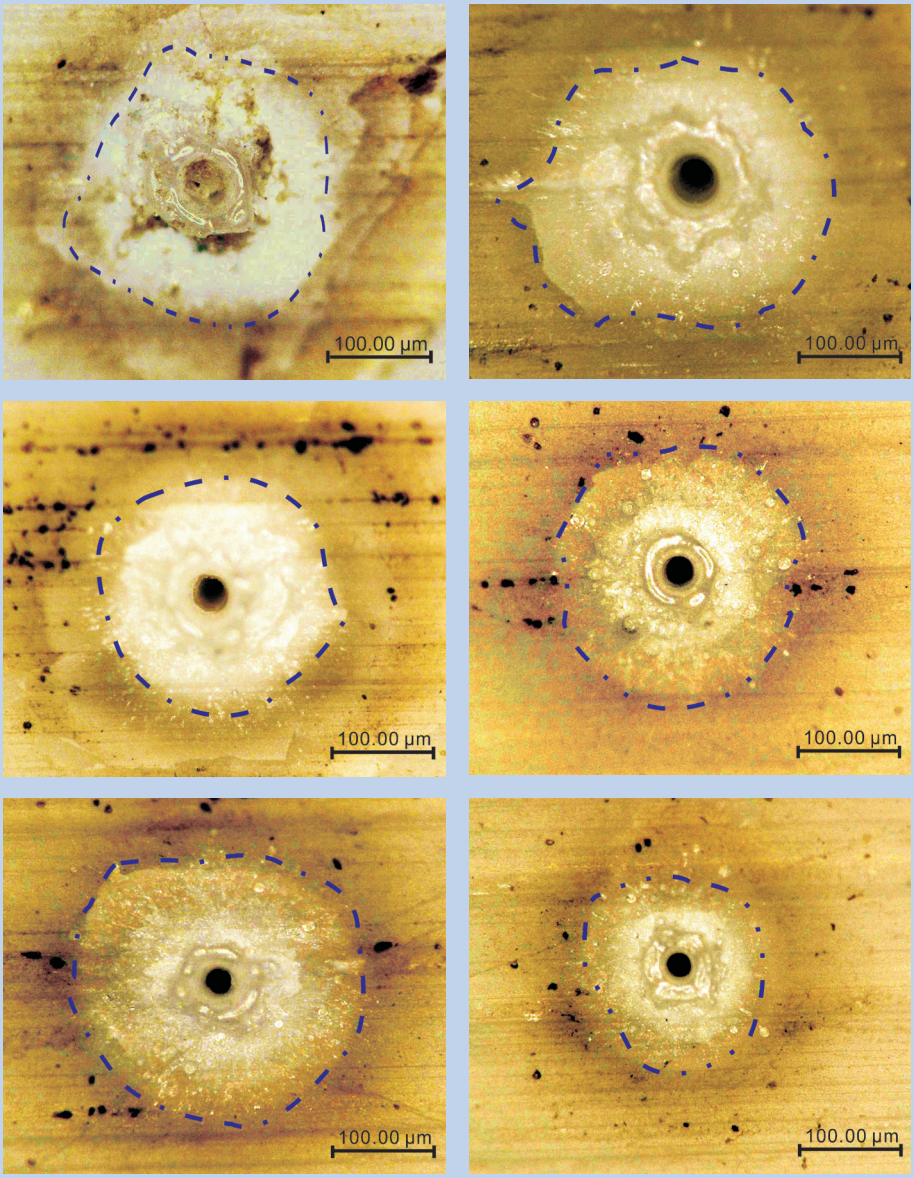

no. 12
year 2015
volume 61

Strojniški vestnik – Journal of Mechanical Engineering (SV-JME)

Aim and Scope
The international journal publishes original and (mini)review articles covering the concepts of materials science, mechanics, kinematics, thermodynamics, energy and environment, mechatronics and robotics, fluid mechanics, tribology, cybernetics, industrial engineering and structural analysis.
The journal follows new trends and progress proven practice in the mechanical engineering and also in the closely related sciences as are electrical, civil and process engineering, medicine, microbiology, ecology, agriculture, transport systems, aviation, and others, thus creating a unique forum for interdisciplinary or multidisciplinary dialogue.
The international conferences selected papers are welcome for publishing as a special issue of SV-JME with invited co-editor(s).

Editorial Office
University of Ljubljana, Faculty of Mechanical Engineering
SV-JME, Aškerčeva 6, SI-1000 Ljubljana, Slovenia
Phone: 386 (0)1 4771 137
Fax: 386 (0)1 2518 567
info@sv-jme.eu, http://www.sv-jme.eu

Print: Grafex, d.o.o., printed in 380 copies

Founders and Publishers
University of Ljubljana, Faculty of Mechanical Engineering, Slovenia
University of Maribor, Faculty of Mechanical Engineering, Slovenia
Association of Mechanical Engineers of Slovenia
Chamber of Commerce and Industry of Slovenia, Metal Processing Industry Association

President of Publishing Council
Branko Širok
University of Ljubljana, Faculty of Mechanical Engineering, Slovenia

Vice-President of Publishing Council
Jože Balič
University of Maribor, Faculty of Mechanical Engineering, Slovenia

Cover: The micro-topography of a single pulsed laser-induced crater with different average laser powers and defocus distances is presented. It was obtained by a new approach for laser-induced deterioration in the wet grinding of ZrO_2 ceramic. The comparative grinding experiment indicated that the strategy was effective. The normal and tangential grinding forces were with a maximum reduction of 59.2 % (62. 9%).

Courtesy: College of Mechanical Engineering, Hunan Institute of Science and Technology; Key Laboratory for High Efficiency and Precision Machining of Difficult-to-Cut Material of Hunan Province , China

ISSN 0039-2480

General information
Strojniški vestnik – Journal of Mechanical Engineering is published in 11 issues per year (July and August is a double issue).

Institutional prices include print & online access: institutional subscription price and foreign subscription €100,00 (the price of a single issue is €10,00); general public subscription and student subscription €50,00 (the price of a single issue is €5,00). Prices are exclusive of tax. Delivery is included in the price. The recipient is responsible for paying any import duties or taxes. Legal title passes to the customer on dispatch by our distributor.

Single issues from current and recent volumes are available at the current single-issue price. To order the journal, please complete the form on our website. For submissions, subscriptions and all other information please visit: *http://en.sv-jme.eu/.*

You can advertise on the inner and outer side of the back cover of the journal. The authors of the published papers are invited to send photos or pictures with short explanation for cover content.

We would like to thank the reviewers who have taken part in the peer-review process.

The journal is subsidized by Slovenian Research Agency.

Strojniški vestnik - Journal of Mechanical Engineering is available on http://www.sv-jme.eu, where you access also to papers' supplements, such as simulations, etc.

Contents

Strojniški vestnik - Journal of Mechanical Engineering
volume 61, (2015), number 12
Ljubljana, December 2015
ISSN 0039-2480

Published monthly

Papers

Strojniški vestnik - Journal of Mechanical Engineering 61(2015)12, 689-697
DOI:10.5545/sv-jme.2015.2794
Original Scientific Paper
Received for review: 2015-06-24
Received revised form: 2015-09-15
Accepted for publication: 2015-10-14

Laser-Induced Deterioration Grinding of Zirconium Oxide (ZrO_2) – Generation of Layer Patterns and Performance Evaluation

Xiaohong Zhang[1,2,*] – Zhaohui Deng[3] – Yinhui Ren[2] – Genyu Chen[2] – Wei Liu[3] – Gaofeng Zhang[4]

[1]Hunan Institute of Science and Technology, College of Mechanical Engineering, China
[2]Hunan University, College of Mechanical and Vehicle Engineering, China
[3]Key Laboratory for High Efficiency and Precision Machining of Difficult-to-Cut Material of Hunan Province, China
[4]Xiangtan University, College of Mechanical Engineering, China

Laser-induced deterioration was proposed for the wet grinding of zirconium oxide (ZrO_2) ceramic used in the dental, semiconductor and automotive industries. The mechanisms for laser induced deterioration and wet grinding of the deterioration layer were theoretically analysed, and the four key processing parameters that determine the micro-topography and distribution of the laser-induced crater were proposed, including the laser power density l_p, the defocus distance z, the laser spot overlap ratio U_s and the laser scanning track line overlap ratio U_l. Further, the forming mechanism of the single pulse-induced crater under different laser power densities, the defocus distance, and the interaction mechanisms between adjacent spots along the longitudinal and transverse directions were investigated. The optimal values of the key processing parameters were identified. To further evaluate the effect of laser-induced deterioration objectively, a comparative experiment was conducted under laser-induced deterioration wet grinding (LIDWG) and conventional grinding (CG) conditions. It was found that the procedure of laser-induced deterioration had a strong influence on the grinding results. The normal and tangential grinding forces for LIDWG condition were lower than for CG condition, with a maximum reduction of 59.2 % (62.9 %).

Keywords: laser-induced crater, deterioration layer, wet grinding, grinding force, zirconium oxide

Highlights

- *The research is focused on analysing the laser-induced deterioration wet grinding of zirconium oxide.*
- *A theoretical study of the micro-topography obtained by laser-induced deterioration under different processing conditions is done.*
- *A uniform distribution of deterioration craters is achieved based on the optimal processing parameters.*
- *An experimental study of the grinding force under different grinding conditions is conducted.*

0 INTRODUCTION

Major advances in the production and application of zirconium oxide (ZrO_2) have been achieved due to their superior properties, such as high thermal strength, hardness, wear resistance, chemical inertness, thermal stability, and high stiffness-to-weight ratio [1]. Diamond grinding and polishing of ZrO_2 have become the most widely used processes in the dental, semiconductor and automotive industries. With the increasing of demand for ZrO_2 products, the widespread use of these materials has been seriously restricted due to the low material removal rate and high processing cost that accounts for more than 75 % of the component cost. The problems associated with precision and efficiency in machining ZrO_2 ceramic have become a significant issue in the manufacturing industry. Rabiey et al. studied novel hybrid bonded diamond tools used to grind zirconium oxide [2]. It was achieved within a selected process window in combination with an elaborate oil cooling system, where material removal was mainly occurring within the ductile cutting mode. A self-sharpening effect of the tool can be observed, and the dressability of the tool further improved the grinding performance. Yan et al. used two-dimensional ultrasonic vibration grinding to machine nano-ZrO_2 and analysed surface quality with or without ultrasonic vibration [3]. The method can improve the surface quality and the life of the diamond wheel. Chen et al. discussed the grinding characteristics and removal mechanisms in the high-speed grinding of ZrO_2 [4]. It was found that the increasing wheel speed can reduce grinding forces due to the reduction of the maximum chip thickness. However, this research mainly focused on the improvement of machining efficiency. The material removal mode was dominated by brittleness removal. In these references, various experiments were carried out on different grinding parameters such as grinding wheel speed, table feed speed, grinding depth, workpiece speed to control surface roughness, residual stresses, and subsurface damage. The rapid blunting and wear of diamond abrasives on the wheel surface may cause frequent redressing and shorten the service life of the grinding wheel [5].

Grinding wheel topography changes during grinding. As a result, the efficiency of the grinding process and the quality of the workpiece are affected

*Corr. Author's Address: College of Mechanical Engineering, Hunan Institute of Science and Technology, China. jansbomb@126.com

negatively most of the time. Wheel wear may induce grinding burn and poor surface quality, even cause serious accidents [6]. Unfortunately, current approaches dealing with wheel wear are based on human experience. The dressing interval is roughly determined, usually by skilled operators. This induces two adverse impacts. Firstly, grinding wheel wear might already happen before the dressing process, which usually causes grinding quality problems. Secondly, if the dressing process is carried out ahead of wheel wear, the grinding efficiency is definitely reduced, and the abrasive materials are simultaneously wasted. Therefore, the material removal behaviour should be mainly plastic deformation and/or ductile removal [7]. Macro-brittle fractures and cracks generated in the grinding mode are not observed. Lower grinding depths and higher wheel speeds were proven to achieve the ductile removal mode. They can also reduce the grinding temperature and the grinding force. However, the disadvantages result in low productivity and high cost.

Laser-assisted machining takes the advantages of local heating and softening of the workpiece by a laser beam in front of the cutting tool. The technique changes the material's behaviour from brittle to ductile. Therefore, it allows difficult-to-machine materials to be machined with greater cutting depth [8] and [9]. In traditional laser-assisted grinding (LAG), the material is heated by a laser prior to the material removal location. Thus, the method permits high stock removal rates [10] and [11]. If the thickness of the heating layer is greater than the grinding depth, the crack may remain in the subsurface, which greatly affects the properties of the machined part. In particular, one of the key factors is the tool-beam distance where the laser beam is positioned to achieve a uniform temperature distribution at the cutting edge without burning the grinding wheel. For a shorter distance, the temperature might not be high enough, and the grinding wheel will be burnt. In contrast, for a longer distance, this process might cause serious surface/subsurface damage in the workpiece. An additional process such as polishing should be added to eliminate this damage. Additionally, the characteristics of traditional LAG limit the use of coolant and also cannot fundamentally eliminate surface/subsurface cracks due to heat accumulation [12] and [13]. These problems have become the bottleneck limiting the application of LAG [14] and [15].

In this paper, a strategy for laser-induced deterioration in the wet grinding of ZrO_2 ceramic has been proposed. Some key processing parameters that determine the micro-topography and distribution of the deterioration layer were discussed based on the forming mechanisms of the single pulse-induced crater and the interaction mechanisms between adjacent spot. A pulsed fibre laser was used to achieve the uniform distribution of deterioration craters by reasonably controlling the average laser power P_{avg}, the defocus distance z, the laser spot overlap ratio U_s and the laser scanning track line overlap ratio U_l. Then, a three-dimensional (3D) microscope with an ultra-large depth-of-field (ULDF) was used to observe the generation of single pulse-induced craters, and the arrangement and distribution of combinations of craters. In particular, the differences in grinding forces obtained under laser-induced deterioration wet grinding (LIDWG) and conventional grinding (CG) conditions were compared and discussed.

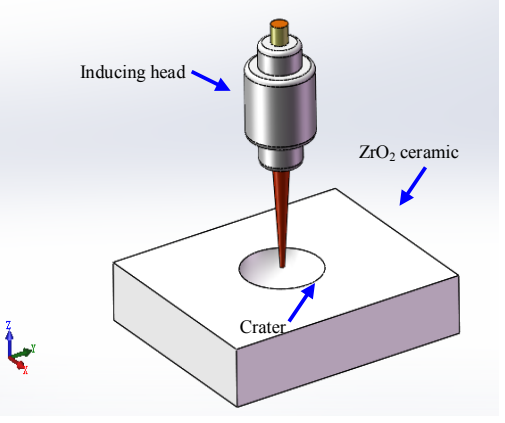

Fig. 1. *Schematic of laser induced deterioration*

The objective of LIDWG is to produce uniform deterioration layer patterns appropriate to a high efficiency grinding task. LIDWG involves two different sub-processes: deterioration and grinding. For conventional LAG, softening and grinding should be done simultaneously. However, for LIDWG, especially in order to integrate the advantages of grinding fluid, deterioration and grinding are performed in two distinct steps [16] and [17]. The first step of LIDWG is briefly illustrated in Fig. 1. As shown in Fig. 1, during the deterioration stage a pulsed incident laser beam was sent in the vertical direction of the workpiece surface. A significant fraction of the incident light energy was absorbed by the workpiece. High-temperature gradients can be caused by intense laser radiation [18]. A multi-axis numerical control (NC) system was applied to precisely control the laser beam while it scanned along the surface of the workpiece. It will lead to the emergence of the deterioration layer. Then, the deterioration layer

was formed within the surface/subsurface of the workpiece. The distribution of the deterioration layer can be made uniform by selecting optimum processing parameters. The laser power density becomes low, indicating that the laser energy is passing through the workpiece surface without forming the desired depth of the deterioration layer. The repeated scanning is necessary until the desired deterioration depth is reached. The mechanism of laser-induced deterioration is to heat, melt, and deteriorate the ceramic material; some of which will also be directly vaporized and decomposed. In contrast, if the laser power density is too high, excess heat will be transferred to the interior of the workpiece. The thermal stress gradient from the workpiece surface to the bottom of the chip is increased. It leads to thermal microcracks, which can severely affect the mechanical properties and surface integrity of the workpiece. In a word, the depth of the deterioration layer should not exceed the grinding allowance.

1 EXPERIMENTAL APPROACH AND PROCEDURE

1.1 Laser-Induced Deterioration Grinding

A cross-section micrograph of induced craters is shown in Fig. 2. H is the depth of the deterioration layer. For the same laser model, the micro-topography of single pulse-induced craters depends on the laser power density I_p and the defocus distance z. The three equations are utilized to calculate the values of the processing parameters including I_p, U_s and U_l.

$$I_P = \frac{4P_m}{\pi d_0^2 f \tau}, \tag{1}$$

$$U_S = \frac{d_0 - S}{d_0} \times 100\%, \tag{2}$$

$$U_L = \frac{d_0 - L}{d_0} \times 100\%. \tag{3}$$

For example, the value of I_p is determined by the four parameters, including average laser power P_{avg}, the pulse frequency f, the diameter of the laser spot on the workpiece surface d_0 and the pulse width τ. Similarly, the ZrO_2 ceramic surface topography generated by pulsed laser depends on the appropriateness of the micro-topography of single pulse-induced craters, the arrangement and distribution of a large number of craters, and the depth of the deterioration layer. The arrangement and distribution of a large number of craters are determined by two processing parameters: U_s and U_l. U_s is the overlap ratio of two adjacent laser spots in the same laser scanning track line. U_l is the overlap ratio of two adjacent scanning tracks on the surface of the workpiece. Considering that the thermal influence mechanism between two adjacent laser spots of different directions is similar, so U_s and U_l are set to equal. This means that three main processing parameters I_p, z, and U_s are very important for the quality of the laser-induced deterioration.

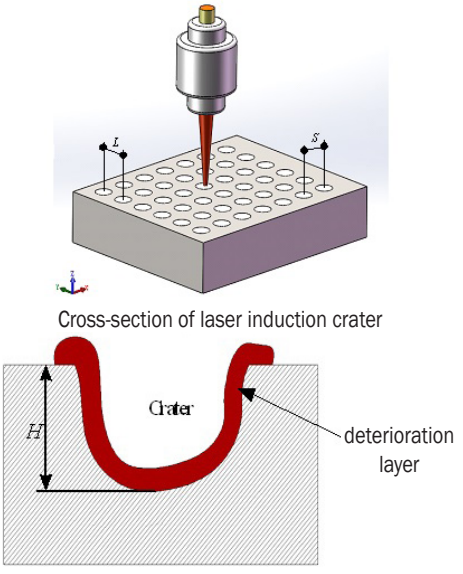

Fig. 2. *Schematic of the micro-topography and distribution of induced craters*

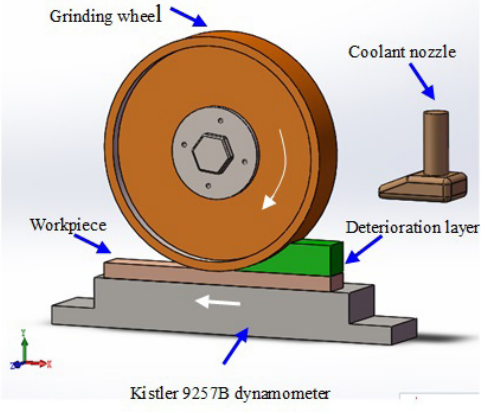

Fig. 3. *Schematic of wet grinding of the deterioration layer*

As shown in Fig. 3, the deterioration layer with a number of laser craters on the workpiece can be removed in the down-grinding mode. In contrast to the traditional grinding process of ZrO_2 ceramic, higher material grinding rates can be achieved. It is possible to avoid a bigger grinding force, a higher grinding temperature, grinding wheel wear, grinding

wheel wear-related or brittle removal mode-related errors. The kinematic parameters of wheel speed (V_s), grinding depth (a_p), and workpiece velocity (V_w) were designed to ensure the whole wet grinding stage could be of high efficiency and high quality.

1.2 Experimental Procedures

The experiment was conducted in two stages. The first stage was the laser-induced deterioration experiment for the ZrO_2 engineering ceramic specimens. The experimental parameters are listed in Table 1a). The deterioration layer surface micro-topography was measured using a 3D ULDF microscope (Model: VHX-S1000) to determine the optimal deteriorating parameters. The second stage was the wet grinding experiment, performed using the processing parameters in Table 1b. Grinding forces in both normal and tangential directions were measured using a dynamometer (Kistler Instrument Corporation, type Kistler 9257B) fixed on the machine table. Surface roughness was measured by a surface coarseness profiling instrument (Type Homel18000) made in Germany.

Table 1. *The experimental parameters of LIDWG*

a) Laser-induced deterioration	
Pulse frequency, f	70 kHz
Average laser power, P_{avg}	25 W to 50 W
Defocus distance, z	0 mm to 2 mm
Track line overlap ratio, U_s	–300 % to 80 %
b) Wet grinding	
Wheel speed, V_s	80 m/s
Grinding depth, a_p	10 μm to 50 μm
Workpiece velocity, V_w	50 mm/s

1.3 Experimental Apparatus and Materials

Fig. 4 shows the apparatus used for the pulsed laser-induced deterioration grinding. A compact pulsed ytterbium-doped fibre laser (Model: YLP-1/120/100/100-HC) was adopted in the experiment. This laser has an average power (P_{avg}) of 10 W to 100 W, a pulse frequency (f) of 50 kHz to 150 kHz, a pulse width (τ) of 210 ns, and a wavelength (λ) of 1,064 nm. The laser energy output has an approximately Gaussian distribution. The laser beam was transmitted to the inducing head with a standard isolator fixed on a 2D motorized translation stage (Model: 7STA01A), using a single-mode fibre, and is then focused using a lenticular lens with a focal length of 180 mm inside the inducing head. The beam struck the working surface of the ZrO_2 ceramic with a defocusing amount of 2 mm and a spot diameter (d_0) of approximately 180 μm. During the laser induced deterioration experiment, a gas nozzle with an inner diameter of 4 mm provided auxiliary lateral blowing air at a pressure of 0.1 MPa. The purpose is to remove any molten material and observe the micro-topography of induced craters easily.

Fig. 4. *a) The apparatus used for laser induced deterioration grinding; b) a detail*

Surface grinding experiments were employed in the down-grinding mode on a high-speed grinder (HGS-II 8000). The spindle is capable of running up to 8000 rpm. The grinding wheel was a diamond grinding wheel of type SDC80N100B. Grinding force signals were recorded by a personal computer via a data acquisition system and then filtered with LABVIEW software. The grinding wheel was dressed by an electroplated diamond roller dresser (Type S-DC-C-110×12×28) in down dressing mode. During grinding, a 3% solution of water-based coolant (Type W20) was applied. The ground surfaces were cleaned with alcohol.

The experimental specimens used in this paper are the ZrO_2 ceramic produced by Yixing Shanjia Company (China). The purity of the ZrO_2 ceramic is 95 %, with a density of 5900 kg/m³, Young's modulus of 200 GPa, a thermal conductivity of 3 W/(m·K), and hardness of 1400 HV. The dimensions of the workpiece are 20 mm × 30 mm × 10 mm.

2 RESULTS AND DISCUSSION

2.1 Laser Induced Deterioration Experiment

2.1.1 Impact of the Laser Power Density on the Micro-Topography

For laser-induced deterioration, the main purpose is to obtain the ideal deterioration layer on the top of the whole surface of ZrO_2 ceramic. Moreover, the distribution of the craters is uniform, and the thickness of deterioration layer is constant. The laser power density I_p and the defocus distance z belong to the most important processing parameters. They are closely related to the geometrical dimension and topography of the induced craters. That is to say, the quality and accuracy of laser induced deterioration are determined by the values of the laser power density and the defocus distance. Of course, it also determines the success or failure of the later period of wet grinding. As shown in Fig. 2, the four parameters were given as fixed values besides the laser power density I_p and the defocus distance z in order to analyse the influence mechanism more accurately. Therefore, to better understand the characteristics of laser-induced deterioration, a variety of trials were carried out by varying the laser power from 25 W to 50 W and the defocus distance from 0 mm to 2 mm for the pulse frequency of 70 kHz, the spot diameter of 0.18 mm and the pulse width of 210 ns.

Fig. 5 shows the micro-topography of a single pulsed laser-induced crater with different average laser powers and defocus distances. Due to the Gaussian nature of the laser beam, the temperatures at the center of the radiation zone exceed the melting temperature of the ZrO_2 ceramic. It can be found from Fig. 5a that when the average power was 25 W and the defocus distance was 2 mm, because of the low corresponding laser power density of 5.29×10^7 W/cm², a small portion of the ZrO_2 ceramic material in the radiation zone deteriorated and was removed mainly through melting, combined with vaporization. This resulted in a small single pulse-induced crater and low laser-induced deterioration efficiency. The

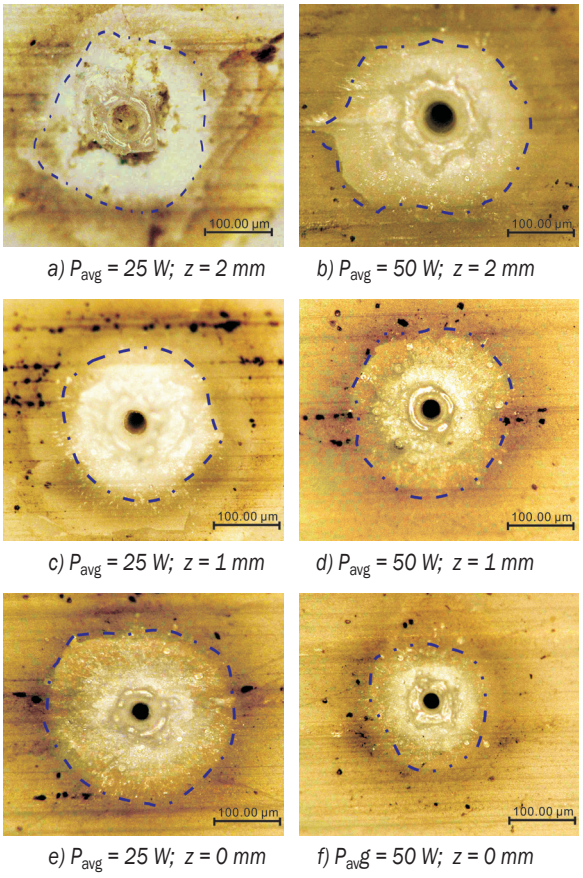

a) P_{avg} = 25 W; z = 2 mm b) P_{avg} = 50 W; z = 2 mm

c) P_{avg} = 25 W; z = 1 mm d) P_{avg} = 50 W; z = 1 mm

e) P_{avg} = 25 W; z = 0 mm f) P_{avg} = 50 W; z = 0 mm

Fig. 5. *The micro-topography of a single pulsed laser-induced crater*

volume and depth of the induced crater was especially trivial. The cause of this failure was the average power being lower and the defocus distance being larger. The temperatures at the center of the radiation zone reached the threshold of heating, melting, and deteriorating the ZrO_2 ceramic material. However, it was insufficient to form an adequate deterioration layer, leaving a shallow and small pit on the surface. As displayed in Fig. 5b, when P_{avg} reached 50 W, corresponding to the laser power density of 10.58×10^7 W/cm², a significant crater can be observed on the ZrO_2 ceramic surface. A larger volume of molten ZrO_2 ceramic spilled outward at greater speeds from the bottom of the crater. The melted material can form a recast layer. Its extension is clearly marked with a blue dotted line. As the defocus distance was gradually decreases within the range from 2 mm to 0 mm, as shown in Fig. 5c to f, the depth of craters increases and the width of craters decreases. When the defocus distance is set to 0, a crater of high depth-diameter ratio will be formed because of energy concentrated in a small

range of spot. The molten material is difficult to climb along the sidewalls of the hole and splash out of the pit. Thus, it is necessary to select a larger value for ensuring a removal area under a certain laser power. Therefore, the volume and depth of the single pulse-induced crater and the laser-induced deterioration efficiency gradually increased with the increasing of the laser power on the premise of a constant defocus distance. They gradually increased with the increasing of the defocus distance on the premise of a constant laser power. Fig. 5d shows that when the average laser power was further increased to 50 W and the defocus distance was set to 1 mm, the volume and depth of the single pulse-induced crater were relatively ideal.

Therefore, a defocus distance of 1mm and an average laser power of 50 W (P_{avg}) was optimal for the pulsed laser induced deterioration of the ZrO_2 ceramic. However, the interaction mechanism of two adjacent laser spots should be investigated, because an excessively high overlap ratio can cause an excessively thermal accumulation in the spot overlap zone. If the depth of the deterioration layer is less than the grinding allowance, it is allowed and beneficial for high efficient processing. Nevertheless, if it is greater than, it will be harmful and could directly cause serious surface damage, or even destroy it.

2.1.2 Impacts of the Overlap Ratios U_s on the Micro-Topography

The forming mechanism of the single pulse-induced crater under different laser power density can only be understood with the analysis of the impact of the laser power densities on the micro-topography. However, during the laser induced deterioration of the ZrO_2 ceramic, the laser outputs a series of laser pulse sequences. In order to achieve the uniform distribution of deterioration craters, improve the grinding efficiency, and reduce the material collapse and grinding wheel wear, it is necessary to reveal the interaction mechanism of two adjacent laser spots. Choosing a suitable laser spot overlap ratio of two adjacent laser spots U_s is the basis for generating the laser pulse-induced craters to cover the entire surface of the ZrO_2 ceramic. An excessively high overlap ratio should not be allowed. It can aggravate surface/subsurface cracks due to the heat accumulation effect. This results in the lower efficiency of laser induced deterioration or even the burning or scrapping of the workpiece.

Fig. 6 displays the micro-topography of laser-induced craters under different laser spot overlap ratio U_s. In the figure, a variety of trials was carried out

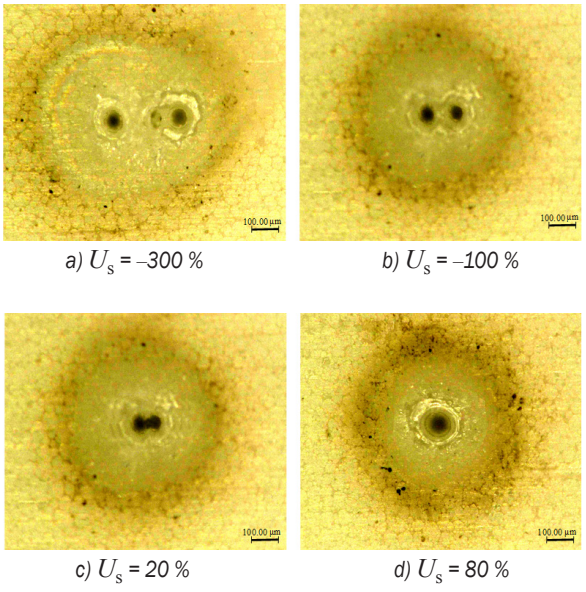

a) U_s = –300 % b) U_s = –100 %

c) U_s = 20 % d) U_s = 80 %

Fig. 6. *The micro-topography of laser-induced craters under different laser spot overlap ratio U_s*

by varying the overlap ratio from -300 % to 80 % for the laser power of 50 W and the defocus distance of 1 mm. Obviously, the lowest low-lying area is the center of the laser-induced crater, and the highest area is the recast layer locating around the crater. It can be found from Fig. 6a that when the laser spot overlap ratio was –300 %, there was no obvious influence between the two adjacent craters due to the far center distance. Fig. 6b shows that when the laser spot overlap ratio was –100 %, the single pulse-induced craters on the ZrO_2 ceramic were approximately dispersed distribution. The material between the two adjacent craters was not vaporized or deteriorated. It cannot reduce the difficulty of the subsequent grinding process. As shown in Fig. 6c, the single pulse-induced craters were connected. The straightness of the induced crater's boundary gradually improved, because a higher laser spot overlap ratio U_s caused increased arrangement density of the single pulse-induced craters and increased uniformity of the laser-induced deterioration efficiency of the ZrO_2 ceramic material in the radiation zone, thus improving the surface quality after deterioration. In particular, the recast layer around the second laser-induced crater was irregular. This phenomenon is attributed to the thermal effect caused by the first laser-induced process. Fig. 6d shows that when the laser spot overlap ratio was 80 %, only one crater can be observed, and its shape is elliptical. The main reason is due to the higher overlap ratio. This will result in a great reduction of

deterioration processing efficiency. Therefore, under the current experimental conditions, an overlap ratio of 20 % was optimal for the pulsed laser induced deterioration of the ZrO_2 ceramic.

2.1.3 Deterioration Experiment

It can be known from the above analysis that a suitable laser spot overlap ratio of two adjacent laser spots U_s only guarantees achieving the uniform distribution of deterioration craters in the same laser scanning track line. For the entire surface of the ZrO_2 ceramic, using a suitable overlap ratio of two adjacent scanning tracks U_l is the key procedure for generating a uniform distribution deterioration layer. Considering that the interaction mechanisms between adjacent spots along the longitudinal and transverse directions are approximately the same, the overlap ratios U_s and U_l are set to be equal. Fig. 7 displays the micro-topography of laser induced craters under laser spot overlap ratios U_s and U_l of 20 %. In order to observe clearly the result of the experiment, the number of the spot along the longitudinal direction was set to 2. It is indicated that a large area of the material was deteriorated, resulting in significant uniformity of deterioration layer distributions. The optimal result of the distribution of the deterioration layer can be achieved.

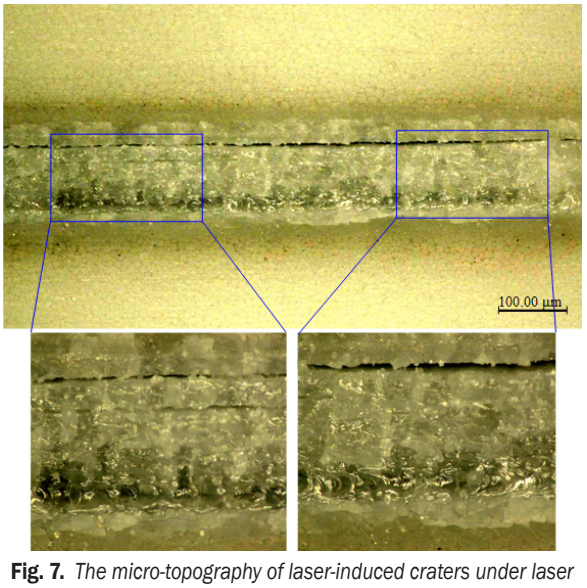

Fig. 7. *The micro-topography of laser-induced craters under laser spot overlap ratio Us and Ul of 20 %*

2.2 Wet Grinding of the Deterioration Layer Experiment

Finally, to further objectively evaluate the performance of laser-induced deterioration, a comparative experiment was conducted under CG and LIDWG conditions. The relationships between the normal and tangential grinding forces (F_t and F_n) to the grinding depth (a_p) during grinding were measured using a dynamometer (Kistler Instrument Corporation, type Kistler 9257B) fixed on the machine table, as shown in Fig. 8a and b, respectively. To better understand the characteristics of LIDWG, a variety of trials were carried out by varying the grinding depth from 10 µm to 50 µm for a workpiece velocity of 50 mm/s and a grinding wheel speed of 80 m/s.

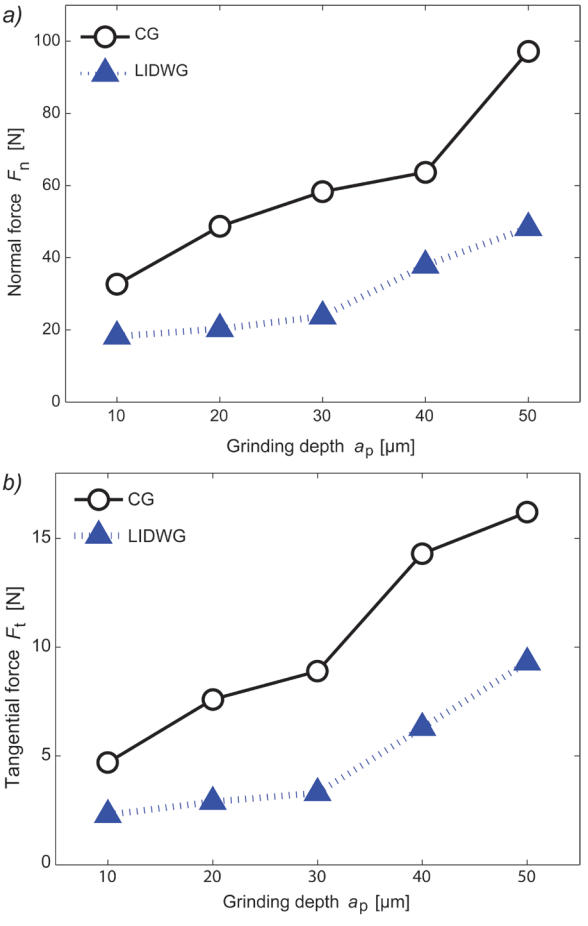

Fig. 8. *The relationship between the grinding force and the grinding depth under CG and LIDWG conditions, a) normal force, b) tangential force*

Fig. 8 shows that the normal and tangential grinding forces at the LIDWG condition were lower than at the CG condition. Furthermore, the normal and tangential grinding forces increased in response to increasing the grinding depth, as expected. This relationship should be attributed to the increasing in the non-deformed chip thickness at greater grinding depths. For the same grinding depth of 10 µm, the average normal (tangential) grinding forces for the

LIDWG condition were 44.2 % (51.1 %) lower than for the CG condition. Similarly, the average normal grinding forces for the LIDWG condition were 58.3 % (61.8 %) lower for a grinding depth of 20 μm and 59.2 % (62.9 %) lower for a grinding depth of 30 μm. The average normal grinding forces for the LIDWG condition were 40.5 % (55.9 %) lower for a grinding depth of 40 μm and 50.3 % (42.6 %) lower for a grinding depth of 50 μm.

A possible reason for this finding is the fact that the deterioration layer has some characteristics, such as loose structure and low strength, and it is also easy to be remove by grinding. In particular, the workpiece surface after laser-induced deterioration was not flat. Compared with CG condition, the amount of grinding removal material was smaller and similar to the intermittent grinding to some extent under LIDWG condition. When grinding a workpiece, the induced craters can result in a decreased contact area between the wheel and the workpiece. Simultaneously, it was found that the craters had the ability to store grinding fluid. This process caused less friction and contact, which eventually decreases the grinding force. In contrast, in the LIDWG condition the removal mode could be transited from a larger scale fracture mode to a smaller scale one. Especially when the grinding depth was less than the thickness of the deterioration layer, the brittle fracture mode could also be changed to a ductile flow. The diamond grinding wheel was not easily blunted. Consequently, less friction and better lubrication/cooling effect were produced between the surfaces of the grinding wheel and the workpiece, i.e., with smaller normal and tangential grinding forces.

3 CONCLUSIONS

In this study, a strategy for laser-induced deterioration in the wet grinding of ZrO_2 ceramic has been proposed. The mechanisms of laser induced deterioration and wet grinding of the deterioration layer were theoretically analysed. A series of laser-induced deterioration experiments and wet grinding experiments were performed on LIDWG and CG conditions, respectively. The uniform distribution of deterioration craters can be achieved by reasonably controlling the laser power density I_p, the defocus distance z, the laser spot overlap ratio U_s and the laser scanning track line overlap ratio U_l. The four key processing parameters ultimately determine the quality and accuracy of the deterioration layer, as well as the success or failure of the later period of wet grinding. The micro-topography of a single pulsed laser-induced crater with different average laser powers and different overlap ratios was measured using a 3D ULDF microscope. When the average laser power (P_{avg}) was 50 W and the corresponding laser power density (I_p) was approximately 10.58×10^7 W/cm², the pulsed laser induced deterioration of the ZrO_2 ceramic yielded satisfactory deterioration quality and less surface damage. The uniform distributions of laser-induced craters under different overlap ratios U_s and U_l is be achieved when their values were 20 %. The comparative grinding experiment indicates that the strategy has been proved effective. The normal and tangential grinding forces for the LIDWG condition were lower than for the CG condition, with a maximum reduction of 59.2 % (62.9 %) for the maximum average normal (tangential) grinding forces, separately. It was attributed to less friction and better lubrication/cooling effect on the basis of the removal mode transition and the ability of craters to store grinding fluid.

4 ACKNOWLEDGEMENT

The authors are grateful for the financial support from the National Natural Science Foundation of China (Grant No. 51405158) and the Open Foundation for High Efficiency and Precision Machining of Difficult-to-Cut Material of Hunan Province (Grant No. E21432). The first author would like to thank Mr. X.Y. Zhao for their experimental support and analysis assistance.

5 REFERENCES

[1] Xie, G.Z., Huang, H. (2008). An experimental investigation of temperature in high speed deep grinding of partially stabilized zirconia. *International Journal of Machine Tools and Manufacture*, vol. 48, no. 14, p. 1562-1568, **DOI:10.1016/j.ijmachtools.2008.06.002**.

[2] Rabiey, M., Jochum, N., Kuster, F. (2013). High performance grinding of zirconium oxide (ZrO2) using hybrid bond diamond tools. *CIRP Annals-Manufacturing Technology*, vol. 62, no. 1, p. 343-346, **DOI:10.1016/j.cirp.2013.03.073**.

[3] Yan, Y.Y., Zhao, B., Liu, J.L. (2009). Ultraprecision surface finishing of nano-ZrO2 ceramics using two-dimensional ultrasonic assisted grinding. *International Journal of Advanced Manufacturing Technology*, vol. 43, no. 5-6, p. 462-467, **DOI:10.1007/s00170-008-1732-x**.

[4] Chen, J., Shen, J., Huang, H., Xu, X.P. (2010). Grinding characteristics in high speed grinding of engineering ceramics with brazed diamond wheels. *Journal of Materials Processing Technology*, vol. 210, no. 6-7, p. 899-906, **DOI:10.1016/j.jmatprotec.2010.02.002**.

[5] Zhang, X.H., Yan, C., Chen, G.Y., An, W.K., Deng, Z.H. (2014). Experimental investigations of microcracks in laser induced cracking turning alumina ceramic. *Materials and*

Manufacturing Processes, vol. 29, no. 10, p. 1277-1283, **DOI:10.1080/10426914.2014.930884**.

[6] Uhlmann, E., Hoghé, T., Kleinschnitker, M. (2013). Grinding wheel wear prediction at double face grinding with planetary kinematics using analytic simulation. *International Journal of Advanced Manufacturing Technology*, vol. 69, no. 9-12, p. 2315-2321, **DOI:10.1007/s00170-013-5197-1**.

[7] Tsai, M.Y., Jian, S.X. (2012). Development of a micro-graphite impregnated grinding wheel. *International Journal of Machine Tools and Manufacture*, vol. 56, p. 94-101, **DOI:10.1016/j.ijmachtools.2012.01.007**.

[8] Ding, H., Shin, Y.C. (2013). Improvement of machinability of Waspaloy via laser-assisted machining. *International Journal of Advanced Manufacturing Technology*, vol. 64, no. 1-4, p. 475-486, **DOI:10.1007/s00170-012-4012-8**.

[9] Singh, G., Teli, M., Samanta, A., Singh, R. (2013). Finite Element Modeling of Laser-Assisted Machining of AISI D2 Tool Steel. *Materials and Manufacturing Processes*, vol. 28, no. 4, p. 443-448, **DOI:10.1080/10426914.2012.700160**.

[10] Westkamper, E. (1995). Grinding assisted by Nd:YAG lasers. *CIRP Annals-Manufacturing Technology*, vol. 44, no. 1, p. 317-320, **DOI:10.1016/S0007-8506(07)62333-6**.

[11] Kumar, M., Melkote, S., Lahoti, G. (2011). Laser-assisted microgrinding of ceramics. *CIRP Annals-Manufacturing Technology*, vol. 60, no. 1, p. 361-370, **DOI:10.1016/j.cirp.2011.03.121**.

[12] Mao, C., Tang, X.J., Zou, H.F., Huang, X.M., Zhou, Z.X. (2012). Investigation of grinding characteristic using nanofluid minimum quantity lubrication. *International Journal of Precision Engineering and Manufacturing*, vol. 13, no. 10, p. 1745-1752, **DOI:10.1007/s12541-012-0229-6**.

[13] Guo, B., Zhao, Q., Fang, X. (2014). Precision grinding of optical glass with laser micro-structured coarse-grained diamond wheels. *Journal of Materials Processing Technology*, vol. 214, no. 5, p. 1045-1051, **DOI:10.1016/j.jmatprotec.2013.12.013**.

[14] Kim, H.C., Ko, T.J. (2015). Verification of simulation of surface texturing on planar surface by grinding. *International Journal of Precision Engineering and Manufacturing*, vol. 16, no. 2, p. 225-231, **DOI:10.1007/s12541-015-0030-4**.

[15] Rabiey, M., Walter, C., Kuster, F., Stirnimann, J., Pude, F., Wegener, K. (2012). Dressing of hybrid bond CBN wheels using short-pulse fiber laser. *Strojniški vestnik - Journal of Mechanical Engineering*, vol. 58, no. 7-8, p. 462-469, **DOI:10.5545/sv-jme.2011.166**.

[16] Walter, C., Komischke, T., Kuster, F., Wegener, K. (2014). Laser-structured grinding tools – generation of prototype patterns and performance evaluation. *Journal of Materials Processing Technology*, vol. 214, no. 4, p. 951-961, **DOI:10.1016/j.jmatprotec.2013.11.015**.

[17] Grigoriev, S.N., Starkov, V.K., Gorin, N.A., Krajnik, P., Kopac, J. (2014). Creep-feed grinding: an overview of kinematics, parameters and effects on process efficiency. *Strojniški vestnik - Journal of Mechanical Engineering*, vol. 60, no. 4, p. 213-220, **DOI:10.5545/sv-jme.2013.1547**.

[18] Sušnik, J., Šturm, R., Grum, J. (2012). Influence of laser surface remelting on Al-Si alloy properties. *Strojniški vestnik - Journal of Mechanical Engineering*, vol. 58, no. 10, p. 614-620, **DOI:10.5545/sv-jme.2012.696**.

Strojniški vestnik - Journal of Mechanical Engineering 61(2015)12, 698-708

DOI:10.5545/sv-jme.2015.2781 Original Scientific Paper
Received for review: 2015-06-19
Received revised form: 2015-09-04
Accepted for publication: 2015-10-14

Automatic Recognition of Machinery Noise in the Working Environment

Primož Lipar* – Mirko Čudina – Peter Šteblaj – Jurij Prezelj
University of Ljubljana, Faculty of Mechanical Engineering, Slovenia

A necessity for the suitable recognition of different machinery and equipment based on the sound they generate is constantly present and will increase in the future. The main motivation for the discrimination between different types of machinery sounds is to develop algorithms that can be used not only for final quality inspection but for the monitoring of the whole production line. The objective of our study is to recognize the operation of the individual machine in a production hall, where background noise level is high and constantly changing. An experimental plan was designed and performed in order to confirm the hypothesis proposing that automatic speech recognition algorithms can be applied to automatic machine recognition. The design of the automatic machine recognition procedure used in our study was divided into three stages: feature extraction, training, and recognition (classification). Additionally, a traditional mel-frequency cepstral coefficient (MFCC) procedure was adjusted for machinery noise by using different filter compositions. Finally, two classifiers were compared, the k-NN classifier and the multivariate Gaussian distribution. The results of the experiment show that machinery noise features frequency cepstral coefficients (FCC) should be extracted by using linear filter compositions and processed with recognition algorithm based on the multivariate Gaussian distribution.

Keywords: machinery noise, machinery classification, *k*-NN classifier, multivariate Gaussian distribution classifier, frequency cepstral coefficients

Highlights

- *Implementation of automatic speech recognition algorithms for machinery noise classification.*
- *Optimization of MFCC filter banks for machinery noise.*
- *Application of multivariate Gaussian distribution as statistical modelling of machinery noise.*
- *Comparison of multivariate Gaussian distribution classifier with k-NN classifier.*
- *Experimental validation of proposed approach.*

0 INTRODUCTION

Automation of production started in early 1913 when Henry Ford invented the conveyor belt. Automation remains one of the main topics of engineering because it offers many benefits; it increases product quality due to the reduction of human error; it increases production volume, it protects human health via the automation of dangerous tasks, and ultimately any threat to life can be minimized. The automation of any process inherently depends on the feedback information from the process itself. Feedback information can be obtained by acquiring different signals from within the controlled system. The sound generated by the machinery can be used for feedback information as reported in numerous examples; Mechanical and electrical faults observed on induction motors have been classified using analysis of the acoustic data by using correlation and wavelet-based analyses for extracting necessary features from the acoustic data [1]. A new technique of acoustic-based diagnosis (ABD) for gearboxes based on near-field acoustic holography (NAH) and spatial distribution features of the sound field was presented in [2]. The fault diagnosis of bearings has been exploited through a machine learning approach by using acoustic signals acquired from the near field area of bearings in good and simulated faults. The descriptive statistical features were extracted from sound signals, and the important ones were selected using a decision tree (dimensionality reduction) [3].Vacuum cleaner motors quality end-test at the end of the manufacturing cycle have been presented in [4]. Efficient signal processing algorithms have been developed to detect and localize bearing faults, defects in fan impellers, improper brush-commutator contacts and the rubbing of rotating surfaces [4].

Sound is typically used for the end quality inspection of produced machinery. Experts learn with experience to listen to the sound of the operating machinery, and use it as an important source of information for the classification between flawless and faulty machines. However, human responsiveness and accuracy are sometimes insufficient for the real-time detection of a failure on produced machinery in mass production. Therefore, the need for suitable recognition of sound generated by the machinery is constantly present and will certainly increase in the future. The improvement of the recognition algorithms

*Corr. Author's Address: University of Ljubljana, Faculty of Mechanical Engineering, Aškerčeva 6, 1000 Ljubljana, Slovenia, primoz.lipar@fs.uni-lj.si

can further be used not only for end quality inspection but for monitoring the whole production line.

Recognition of different sounds has a long history, with its roots in 1952 when Bell Labs demonstrated the first automatic speech recognition (ASR) systems for small-vocabulary recognition of digits spoken over the telephone. After computers had grown in power during the 1960s, filter banks were combined with dynamic programming to produce the first practical recognizers, mostly for words spoken in isolation. In 1970 linear predictive coding (LPC) became a dominant ASR algorithm. During the 1980s, it was replaced with mel-frequency cepstral coefficients (MFCCs). During the 1990s, commercial applications evolved from isolated-word dictation systems to general-purpose continuous speech systems [5] and [6].

Since the mid-1990s, ASR has been largely implemented in commercial software. Medical reporting and legal dictation have been two applications driving the development of ASR, as well as the automation of services to the public over the telephone [5]. Applications of ASR methods were extended to environmental sound recognition in 1993. The MFCC parameterization method was implemented in combination with the class statistic classifier [7]. Significant progress on environmental sound recognition was achieved when MFCC parameterization was combined with the matching pursuit (MP) algorithm [8]. MFCC has been widely used in environmental sound recognition as well as its first and second derivatives in combination with other parameterization methods [9] and [10]. Available literature studies about industrial machine sound recognition are usually based on the Morlet wavelet parameterization approach [11] to [13]. Furthermore, MFCC can be used as a damage-sensing feature because its compactness and de-correlation characteristics make it particularly suited for statistical recognition applications. Attempts to use the MFCC parameterization method to extract features of industrial sounds to detect faults was already discussed in the literature [14] and [15], with no modification to the algorithms.

The objective of our study is to recognize the operation of an individual machine in a production hall where the background noise level is high and constantly changing. The knowledge transfer from ASR to machinery sound identification seems to be a reasonable choice due to the efficiency of speech and speaker identification. Human speech is more dynamic than the sound produced by machines. The time stability of non-natural sounds should even increase the identification efficiency. The purpose of this paper is to show that the pattern recognition and feature extraction methods used in ASR systems, after minor modifications, can be efficiently used to identify different machine sounds even in noisy environments. An experimental plan was designed and performed in order to confirm the hypothesis proposing that ASR algorithms can be applied for automatic machine recognition (AMR). The design of the AMR procedure used in our study was divided into three stages: feature extraction, training, and recognition (classification).

The procedure presented in this paper is used in the system for the automatic classification of noise events during environmental noise measurements [16]. The same procedure was also tested for detection of cavitation phenomena on kinetic pumps [17]. The influence of various rotor designs on the generated noise is also tested with the same procedure.

1 FEATURE EXTRACTION, TRAINING, AND RECOGNITION

Feature extraction is essential in the ASR and AMR due to the quality of training models. Likewise, pattern matching strongly depends on the quality of feature extraction methods. There are many different features of sound signals:

- **Temporal features** are computed from the waveform or the signal energy envelope: log-attack time, temporal decrease, temporal centroid, effective duration, zero-crossing rate, cross-correlation.
- **Energy features** refer to various energy contents of the signal: global energy, harmonic energy, and noise energy.
- **Spectral features** are computed from the short-time Fourier transform (STFT) of the signal: spectral centroid, spread, skewness, kurtosis, slope, decrease, roll-off point, variation, etc.
- **Harmonic features** are computed from the sinusoidal harmonic modelling of the signal: fundamental frequency, noisiness, odd-to-even harmonic ratio, tristimulus, deviation, centroid, spread, skewness, kurtosis, slope, decrease, roll-off point, variation.
- **Perceptual features** are computed using a model of the human hearing process: MFCC, first order derivative of MFCC (DMFCC), and second order derivative of MFCC (DDMFCC), loudness, specific loudness, sharpness, spread, roughness, and tonality [18].

To extract sound features from the sound signal with dynamic level changes, similar to speech, more

complex parameterization methods have to be used, as discussed in publications [19] and [20]. Most commonly used parameterization method in speech or speaker recognition systems is the MFCC method. It was used by many authors and, according to the literature survey, gives the best classification results in ASR. The time constant of features extraction is essential. In our application it turned out that the noise generated by the observed machinery is less dynamic than speech; therefore, the length of time window was set to 50 ms. Machinery sounds are usually generated by rotational movements that cause a harmonic form of noise. Machines have different sizes, operational conditions (speed and load), tasks, etc., thus leading to the different distribution of spectral energies. Frequency cepstral coefficient (FCC) parameterization is based on the deconvolution of spectral energies obtained from certain frequency ranges, thus making it a reasonable choice for machinery sound recognition.

1.1 Feature Extraction Based on the FCC Parameterization

The performance of FCC may be affected by the number of filters, the shape of filters, the way that filters are spaced and the way that the power spectrum is warped [21]. A chart diagram of FCC parameterization, as used in our experimental application, is shown in Fig. 1.

The basic FCC feature extraction procedure was performed by applying a standard mel filter, and additionally by applying two different filter scalings: linear and logarithmic.

To calculate the FCC, the signals are first divided into short time intervals. Hamming windowing is then applied and fast Fourier transformation (FFT) of each time window for the discrete-time signal $x(n)$ with length N is calculated. The magnitude spectrum $|X(k)|$ is now scaled in both frequency and magnitude, where k stands for the FFT index of frequency. First, the frequency is scaled using one of the filter banks $|H(k,m)|$. Then the logarithm is taken, according to Eq. (1):

$$X'(m) = \ln\left(\sum_{k=0}^{N-1}\left|X(k)\right|H(k,m)\right). \tag{1}$$

For $m = 1, 2, \ldots, M$, where M is the number of filters in a bank. Three different filter banks were used in our application; a mel scale filter bank, a linear filter bank, and a logarithmic filter bank. All three filter banks are based on a collection of triangular filters defined by the centre frequencies $f_c(m)$, as written in Eq. (2). Central frequencies are given in Eqs. (5), (6) and (10) for mel scale, linear scale and logarithmic scale respectively.

$$H(k,m) = \begin{cases} 0 & \text{for} \quad f(k) < f_c(m-1) \\ \dfrac{f(k) - f_c(m-1)}{f_c(m) - f_c(m-1)} & \text{for} \quad f_c(m-1) \le f(k) < f_c \\ \dfrac{f(k) - f_c(m+1)}{f_c(m) - f_c(m+1)} & \text{for} \quad f_c(m) \le f(k) < f_c(m+1) \\ 0 & \text{for} \quad f(k) \ge f_c(m+1) \end{cases}. \tag{2}$$

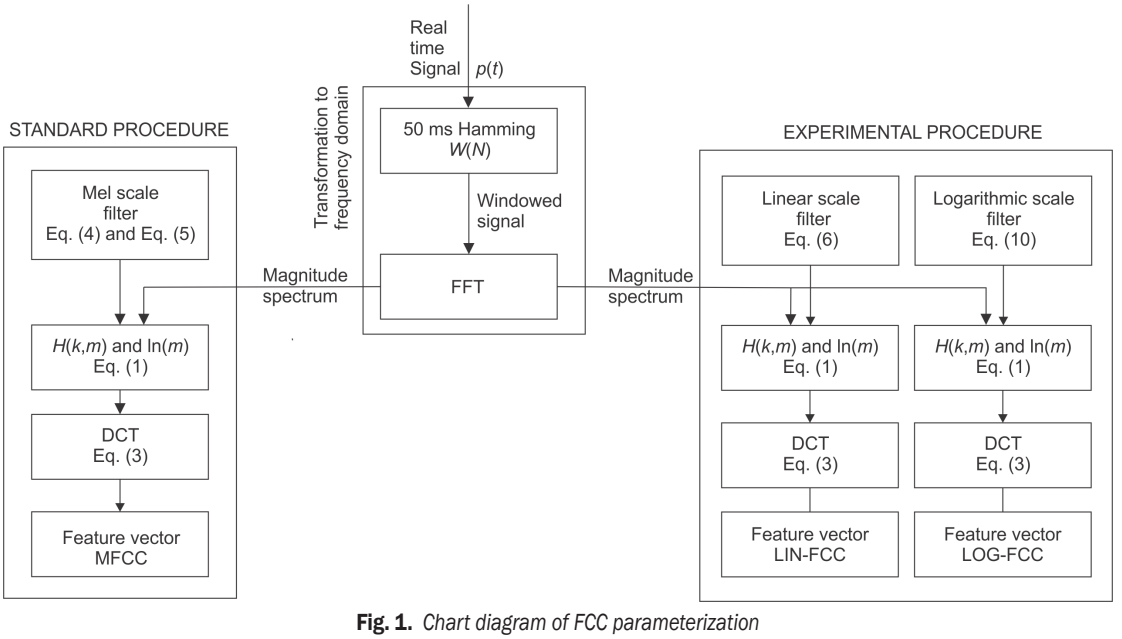

Fig. 1. *Chart diagram of FCC parameterization*

Three different types of FCCs (MFCC, lin-FCC and log-FCC) are obtained from filtered $X'(m)$ using Eq. (3):

$$c(l)=\sum_{m=1}^{M}X'(m)\cos(l\frac{\pi}{M}(m-\frac{1}{2})). \quad (3)$$

For $l=1,2,\ldots,12$, where $c(l)$ is the l^{th} FCC [22]. Three different types of filters influence the $c(l)$ through the filtered magnitude spectre $X'(m)$.

1.1.1 Mel Scale Filter

MFCCs are obtained from $X(m)$ which is filtered with a mel-scale filter bank. The centre frequencies of filters in the mel filter bank are computed by approximating the mel scale with:

$$\phi=2595\log_{10}\left(\frac{f}{700}+1\right), \quad (4)$$

which is a common approximation. Afterward, the fixed frequency resolution in mel scale is computed, corresponding to the logarithmic scaling of the repetition frequency, using $\Delta\phi=(\phi_{\max}-\phi_{\min})/(M+1)$. Therefore, $\phi_{\max}$ is the highest frequency of the filter bank on the mel scale, computed from $f_{\max}$ using Eq. (4), $\phi_{\min}$ is the lowest frequency in mel scale, and M is the number of filters in a bank. The centre frequencies on the mel scale are given by $\phi_c(m)=m\Delta\phi$ for $m=1,2,\ldots,M$ [22]. By using the inverse of Eq. (4), centre frequencies in Hz are obtained by:

$$f_c(m)=700(10^{\phi_c(m)/2595}-1). \quad (5)$$

The low-frequency limit and high-frequency limit of the individual filter in a bank are obtained by taking the central frequency of the previous and next filter. Because mel scale is adjusted to human speech and hearing, it provides good results in speaker/speech identification systems. Due to the temporal stability and linearity of machine sounds, it was essential to test the linear and the octave-based frequency scaling to calculate lin-FCCs and log-FCCs.

1.1.2 Linear Scale Filter

Central frequencies of the linear filter bank are obtained with the linear equation:

$$f_c(m)=f_{\min}\cdot\Delta f\cdot m, \quad (6)$$

for $m=1,2,\ldots,M$, where

$$\Delta f=\frac{f_{\max}\cdot f_{\min}}{(M+1)}. \quad (7)$$

Low filter frequencies are computed by using:

$$f_l(m)=f_{\min}\cdot\Delta f\cdot m, \quad (8)$$

for $m=0,1,\ldots,(M-1)$, and high filter frequencies are computed by using:

$$f_h(m)=f_{\min}\cdot\Delta f\cdot m, \quad (9)$$

for $m=2,3,\ldots,(M+1)$.

1.1.3 Logarithmic Scale Filter

Comparison of the results obtained by mel and linear filters with 1/n octave filters is not possible, because of the different number of filters in the collection. Therefore, logarithmic composition was used, due to its similarity with the central frequencies composition of the octave band filters. The central frequencies of such filters were calculated using this equation:

$$f_c(m)=10^{m\Delta f_{\log}+\log_{10}(f_{\min})}, \quad (10)$$

for $m=1,2,\ldots,M$, where $\Delta f_{\log}$ is calculated by:

$$\Delta f_{\log}=\frac{\log_{10}(f_{\max})-\log_{10}(f_{\min})}{M+1}. \quad (11)$$

Low frequencies of filters are calculated by:

$$f_l(m)=10^{m\Delta f_{\log}+\log_{10}(f_{\min})}, \quad (12)$$

for $m=0,1,\ldots,(M-1)$, and high filter frequencies by:

$$f_h(m)=10^{m\Delta f_{\log}+\log_{10}(f_{\min})}, \quad (13)$$

for $m=2,3,\ldots,(M+1)$.

1.2 Classification Using *k*-NN and MGD

The classification process of machinery into classes, based on generated sounds, is divided into two steps: training and testing. To train the algorithm and obtain the reference template, enough samples of generated sound should be available for each class. Extracted features from sound signals generated by known sources are used during the training procedure when the class reference template model is learning. In the second step, the sound signal from the unknown machine is matched with a stored reference template model, and classification decisions are made [23]. Two classification algorithms, which have diametrically opposed classification approaches, were tested: *k*-nearest neighbour (*k*-NN) and multivariate Gaussian distribution (MGD). MGD can be regarded as a single state Gauss Mixture Model (GMM). Simpler MGD was selected over the GMM, because it provides better results when adapting new data into the database [24].

1.2.1 k-NN Algorithm

The *k*-NN algorithm is one of prospective statistical classification algorithms used for classifying objects based on the closest training examples in the feature space. It is a lazy learning algorithm in which the *k*-NN function is approximated locally, and all computations are deferred until classification. No actual model or learning is performed during the training phase, although a training dataset is required. It is used solely to populate a sample of the search space with instances whose class is known. For this reason, this algorithm is also known as the lazy learning algorithm, which means that the training data points are not used to do any generalization, although all the training data is needed during the testing phase.

One of the advantages of the *k*-NN method in classifying the objects is that it requires only a few parameters to tune: *k* and the distance matrices, for achieving sufficiently high classification accuracy. Thus, in *k*-NN-based implementation, the best choice of *k* and distance metric for computing the nearest distance is a critical task. Generally, large values of *k* reduce the effect of noise on the classification but make boundaries between classes less distinct [25].

k-NN classification is based on measuring the Euclidean distance (Eq. (14)) between unknown sample vector $\mathbf{X}s$ and known sample vectors $\mathbf{X}_m = [X_1, X_2, ..., X_m]$ sorted in the database.

$$d_{sm} = \sqrt{\sum_{n=1}^{N} \left(x_{sn} - x_{mn}\right)^2}, \tag{14}$$

where index *n* is the size of observations and *m* is an index of the individual vector.

1.2.2 Multivariate Gaussian Distribution

The multivariate Gaussian distribution (MGD) is a generalization to two or more dimensions of the univariate Gaussian (or normal) distribution, which is often characterized by its resemblance to the bell shape. This algorithm is selected according to the statistical analysis of the reference feature vectors. The histogram of individual feature vector components indicates their Gaussian distribution. An additional advantage of the algorithm is its high computational speed. MGD is the Gaussian mixture model with a hypothetical mixture.

During preliminary studies individual vector components were identified to have the univariate Gaussian distribution with acceptable deviation. If the real-valued univariate random variable X is said to have the Gaussian distribution with mean μ and variance σ^2 (written as $X \sim N(\mu, \sigma^2)$), than its density function can be written as:

$$f(x \mid \mu, \sigma) = \frac{1}{(2\pi\sigma^2)^{1/2}} e^{-\frac{1}{2\sigma^2}(x-\mu)^2}, \tag{15}$$

where $-\infty < \mu < \infty$ and $\sigma > 0$. The vector-valued random variable $\mathbf{X} = [X_1, ..., X_r]^T$ is said to have multivariate Gaussian distribution with mean *r*-vector $\boldsymbol{\mu}$ and positive defined symmetric $(r \times r)$ covariance matrix Σ, if its density function is given by the curve;

$$f(\mathbf{x} \mid \boldsymbol{\mu}, \Sigma) = \frac{1}{(2\pi)^{-1/2} \left|\Sigma\right|^{-1/2}} e^{-\frac{1}{2}(x-\boldsymbol{\mu})^T \Sigma^{-1} (x-\boldsymbol{\mu})}, \tag{16}$$

$x \in \Re^r$. If $\mathbf{X}$ is a random *r*-vector with values within $\Re^r$, then its expected value is the *r*-vector:

$$\boldsymbol{\mu}_X = E(\mathbf{X}) = \left[E(X_1), \ldots, E(X_r)\right]^T = \left[\mu_1, \ldots, \mu_r\right]^T, \tag{17}$$

and the $(r \times r)$ covariance matrix of $\mathbf{X}$ is given by:

$$\begin{aligned} \Sigma_{XX} &= \operatorname{cov}(\mathbf{X}, \mathbf{X}) = E\left[(\mathbf{X} - \boldsymbol{\mu}_X)(\mathbf{X} - \boldsymbol{\mu}_X)^T\right] = \\ &= E\left[(X_1 - \mu_1, \ldots, X_r - \mu_r)(X_1 - \mu_1, \ldots, X_r - \mu_r)^T\right] = \\ &= \begin{pmatrix} \sigma_1^2 & \sigma_{12} & \cdots & \sigma_{1r} \\ \vdots & \ddots & \vdots & \\ \sigma_{1r} & \sigma_{r2} & \cdots & \sigma_r^2 \end{pmatrix}, \end{aligned} \tag{18}$$

where

$$\sigma^2 = \operatorname{var}(X_i) = E\left[(X_i - \mu_i)^2\right], \tag{19}$$

is the variance of X_i, $i = 1, 2, \ldots, r$, and

$$\sigma_{ij} = \operatorname{cov}(X_i, X_j) = E\left[(X_i - \mu_i)(X_j - \mu_j)\right], \tag{20}$$

is the covariance between X_i and X_j, $i, j = 1, 2, \ldots, r$ $(i \neq j)$ [26].

A covariance matrix (also known as dispersion matrix or variance-covariance matrix) is a matrix whose element in the *i*, *j* position is the covariance between the i^{th} and j^{th} elements of a random vector. Each element of a vector is a scalar random variable, either with a finite number of observed empirical values, or with a finite or infinite number of potential values specified by a theoretical joint probability distribution of all the random variables. Multivariate Gaussian distribution density exists when the symmetric covariance matrix is positive definite. A sample covariance can be calculated using following equation:

$$\sigma_{ij} = \frac{1}{N-1} \sum_{n=1}^{N} (x_{ni} - \mu_i)(x_{nj} - \mu_j), \tag{21}$$

where N is the number of samples of a X_i or X_j vector component.

2 EXPERIMENT

An experimental plan was designed to evaluate the hypothesis proposing that an ASR algorithm can be applied for AMR. A traditional FCC method from ASR was used to extract sound features from typical industrial and machinery sounds. The classification of feature vectors was performed by *k*-NN and MGD at different signal-to-noise ratios (SNRs). The industrial noise was mixed with machinery sounds as background noise to set the SNRs. All machinery signals were first pre-processed to assure equal energies. SNR was set to 7 dB and 2 dB below the signal level by mixing industrial noise having appropriate energy levels with sample signals. Five different machines and three different operations were included in the MSR. The classification performance was tested by applying different filter types and different numbers of filters to FCC calculations. Experiments were conducted for traditional mel scale filter banks, and for two additional filter banks: the Linear and Logarithmic filter banks. The experimental plan which was designed and performed is presented in Table 1.

Measurements of machinery sounds were performed in a laboratory environment. The experimental set-up is shown in Fig. 2, where the position of measured machines and microphone are constrained, as well as room dimensions. To test the robustness of the proposed algorithms, original sounds were mixed with background noise having three different sound pressure levels (SPLs). All machines sound SPLMs were set to equal levels. Background noise SPLBG was adapted to ensure three different SNRs. The reverberation time of the room was 0.8 s. Sounds of two different vacuum cleaners, jigsaw, compressor, and drill were recorded using a B&K microphone and M-audio sound card. Also, the sounds of the jigsaw cutting aluminium plate, drilling holes into a steel plate and grinding aluminium plate on a grinding machine were recorded to simulate different operations. One-minute sound samples were recorded without background noise and with a sampling frequency of 48000 Hz and 16-bit resolution. Background noise was recorded in the industrial hall to simulate a real industrial environment. Parameterization of sound samples and classification was done in a program written in LabVIEW. The program was designed to allow the user to change FCC parameters (time window length, overlapping, frequency range, filter type, and the number of filters). FCCs were extracted to 50 ms time windows of the signal with 40 % overlapping in a frequency range from 100 Hz to 8000 Hz.

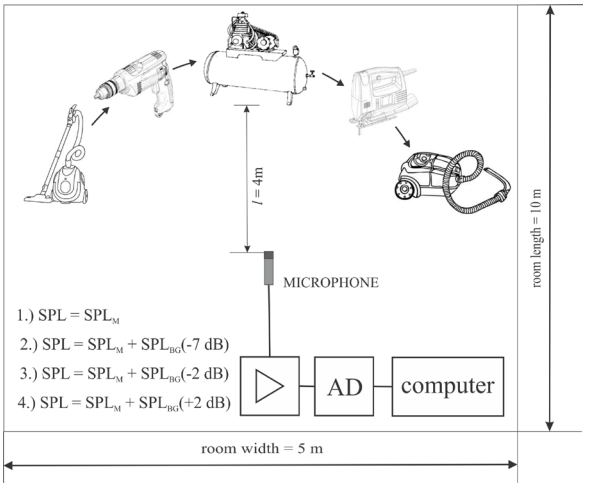

Fig. 2. *Experiment set-up scheme*

2.1 Database Design

Because the *k*-NN algorithm has no training mode, its database is just a compilation of vectors composed from FCCs, which result from pure machinery sound signals. In contrast, the MGD algorithm works only with the reference template models. FCCs of sound samples with no background noise were used in a training mode to build a MGD reference template model. The database for the MGD classifier

Table 1. *Parameters of experimental plan*

Parameter	1	2	3	4	5	6	7
Signal / noise	7 dB	2 dB	–2 dB	/	/	/	/
Filter size	3	6	12	18	24	30	36
Algorithm	k-NN	MGD	/	/	/	/	/
Filter type	mel	linear	Log	/	/	/	/
Machine type	compressor	vacuum cleaner 1	Jigsaw	drill	vacuum cleaner 2	/	/
Machinery operations	jigsaw cutting Al	drilling	Grinding	/	/	/	/

parameters is composed of mean value vector **μ**, the determinant of covariance matrix $|\Sigma|$ and inverse of covariance matrix Σ^{-1}.

If the covariance matrix is not full rank, then the multivariate normal distribution is degenerate and does not have a density. More precisely, it does not have a density with respect to the *r*-dimensional Lebesgue measure. In other words, the *r* dimensional MGD of vector **X** has density if the covariance matrix is positive definite i.e. feature vector components are independent. If non-diagonal covariances are zero valued, then the covariance matrix becomes a diagonal variance matrix.

In practice, the non-diagonal covariances of vector components are not necessarily zero valued. This can result in a negative matrix determinant. If its determinant is zero, the matrix becomes non-invertible. Eq. (16) indicates that the determinant of a covariance matrix must be positive. It is positive in the case of a diagonal variance matrix but not necessarily otherwise. Individual components of vector **X** have 12 coordinates (12 FCCs). An individual vector component was treated as the normally distributed univariate. If the 12 dimensional covariance matrix of vector **X** is positive definite than MGD density exists, otherwise we must reduce components to the number at which point the covariance matrix become positive definite. The MGD database size of the individual model depends on the size of a positively definite covariance matrix.

2.2 Classification

The MGD rate of machinery sound recognition was determined by applying the voting procedure, where the decision of affiliation is based on a maximum matching of the unknown feature vector with the reference template models. MGD was used as a parametric model of the probability distribution for FCC feature measurements. The MGD algorithm calculates the probability of affiliation for an unknown feature vector based on the stored models and votes for the one with the maximum probability. The *k*-NN algorithm is quite different from MGD. It simply measures the Euclidian distances between the unknown feature vector and those stored in the database and votes for the *k* minimum measured distances.

The experimental design included the analysis of both, the impact of the number of filters and different composition of filters on a classification performance. The experimental plan also compared the classification performance of two classifiers. Classification performances have been tested for two different SNRs to simulate real environmental conditions, where performance can be degraded due to all sorts of disturbances.

3 RESULTS AND DISCUSSION

Classification performance results from the *k*-NN and MGD classifiers for a different number of filters in the filter bank are shown in Table 2. The results are presented as an average of classification performance of five different machine sounds. Classification performance for 12 filters gives the best performance for all filter types, regardless of SNR. The obvious conclusion is that MGD provides better performance when SNR decreases, or when the background noise level increases. Regardless of the filter type, the MGD-based classification provides better performance than the *k*-NN based classification, when using an optimal number of filters.

Table 2. *MGD and k-NN classification results for different number and compositions of filters at two different SNR values*

	SNR	N filters	3	6	12	18	24	30	36
Mel	7 dB	MGD	78.56	80.27	**81.54**	63.70	75.48	74.23	55.44
		k-NN	79.78	81.15	**83.72**	82.02	79.35	76.26	72.96
	2 dB	MGD	61.26	63.57	**64.32**	53.26	60.36	60.92	46.04
		k-NN	55.26	57.68	**59.08**	58.05	57.73	57.11	49.60
Linear	7 dB	MGD	84.73	97.34	**98.92**	82.88	94.47	83.02	59.01
		k-NN	91.45	95.79	**97.46**	78.78	88.04	83.00	84.35
	2 dB	MGD	74.06	83.06	**79.74**	63.52	76.52	65.08	49.00
		k-NN	65.89	68.76	**71.03**	55.26	59.71	50.77	55.49
Logarithmic	7 dB	MGD	78.74	82.36	**83.04**	68.02	47.24	42.04	51.77
		k-NN	70.55	75.03	**75.74**	73.24	57.88	54.36	42.98
	2 dB	MGD	50.21	53.88	**54.98**	40.70	38.56	36.87	39.81
		k-NN	48.65	52.47	**54.03**	39.55	36.59	35.47	37.69

Fig. 3 summarizes the results for the optimal number of filters (12 filters) as given in Table 2. Classification performance of different filter compositions for the case of using a *k*-NN or MGD classifier is clearly evident from Fig. 3. The best recognition rates are achieved by using 12 linear filters with an MGD classifier. Its advantage was especially clear when SNR was reduced to only 2 dB. The reason relates to the standard deviation of individual feature vector components. The use of 12 filters gives the best decomposition of filtered magnitude spectrum energies with the lowest possible standard deviation of individual decomposed component. Standard deviations become higher if the number of filters is lower or higher than 12. Narrow standard deviation of individual vector components provides better results.

As the results in Table 2 and Fig. 3 show the average of classification performance, the results in Tables 3 and 4 show a matrix of the classification rates. Tested objects are labeled in the first column, and the classification results are given in rows. Results of classification with 12 linear filters used in combination with MGD classifier are presented in Table 3. One misclassification occurred when using this combination at SNR of 2 dB, when a jigsaw was classified as a compressor.

The *k*-NN algorithm provides similar results, also with one misclassification for SNR of 2 dB. FCCs of vacuum cleaner 1 were misclassified as a compressor, but the other test objects were classified correctly.

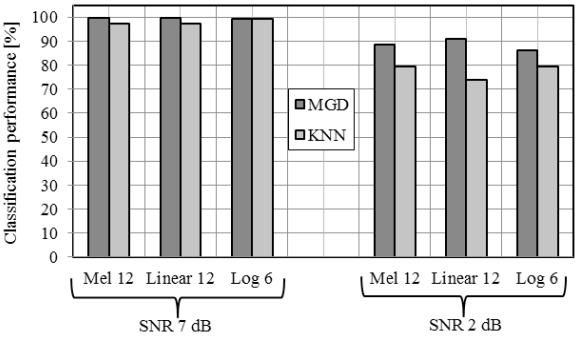

Fig. 3. *Impact of different filter compositions on classification performance of MVD and k-NN at SNR of 7 dB and 2 dB for machinery sounds*

Although *k*-NN is a simple algorithm and gives good classification results, it suffers from a few disadvantages in real-time applications. The *k*-NN algorithm requires a large database because all training feature vectors of all classes must be stored. Database size of feature vectors increases with the length of

Table 3. *Matrix of MGD classification performance at optimal FCC settings*

		Compressor	Vacuum cleaner 1	Jigsaw	Drill	Vacuum cleaner 2
Linear filters MGD classifier **SNR 7 dB**	Compressor	**100**	0	0	0	0
	Vacuum cleaner 1	0	**99.9**	0	0.1	0
	Jigsaw	4.8	0	**95**	0.2	0
	Drill	0	0.1	0.2	**99.7**	0
	Vacuum cleaner 2	0	0	0	0	**100**
Linear filters MGD classifier **SNR 2 dB**	Compressor	**100**	0	0	0	0
	Vacuum cleaner 1	0	**98.6**	0	0.2	1.2
	Jigsaw	**92.6**	0.1	3.5	3.8	0
	Drill	0	3.4	0	**96.6**	0
	Vacuum cleaner 2	0	0	0	0	**100**

Table 4. *Matrix of k-NN classification performance at optimal FCC settings*

		Compressor	Vacuum cleaner 1	Jigsaw	Drill	Vacuum cleaner 2
Linear filters *k*-NN classifier **SNR 7 dB**	Compressor	**100**	0	0	0	0
	Vacuum cleaner 1	0	**98.6**	0	0.2	1.2
	Jigsaw	0.5	0	**99.5**	0	0
	Drill	0	2.4	9.81	**87.79**	0
	Vacuum cleaner 2	0	0	0	0	**100**
Linear filters *k*-NN classifier **SNR 2 dB**	Compressor	**100**	0	0	0	0
	Vacuum cleaner 1	**89.29**	0	0	0	10.71
	Jigsaw	28.13	0	**78.87**	0	0
	Drill	0	2.8	20.62	**76.28**	0.3
	Vacuum cleaner 2	0	0	0	0	**100**

the training samples, as well as with the number of classes. The second disadvantage is its speed and accuracy, which are related with the determination of *k*-NN. The increase of the *k*-neighbours results in a decrease of the self-classification accuracy, in a decreased probability of misclassification, and in an increase of the computation time.

The influence of the number *k* (number of nearest neighbours) on the classification performance and computation time is evident from Fig. 4. Decreasing the *k* seems to be a reasonable choice according to the results shown on the graph, but it should be reconsidered. Finding the optimal *k* is essential for achieving good results in real applications.

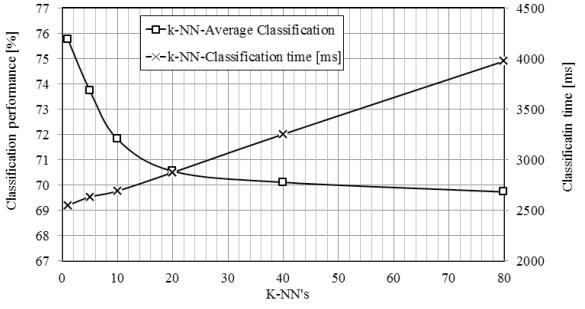

Fig. 4. *Impact of k-NN on classification performance and computation time at SNR of 2 dB*

Contrary to the *k*-NN-based classification, the MGD-based classification is faster, and its computation speed depends only on the number of reference template models (classes). The database for an individual class consists only of few statistical parameters. The small size of the database ensures a small storage size of the reference template model. The average classification time of 2000 feature vectors using MGD is 50 ms whereas *k*-NN is more than 2.5 s.

The results of the classification performance of different machinery operations using an optimal number of filters are summarized in Tables 5 and 6. A comparison of the classification performances of different filter types with MGD or *k*-NN classifier at different SNRs is depicted in Fig. 5. Best recognition rates were achieved by using 12 mel filters with *k*-NN classifiers when SNR was 7 dB. Decreasing SNR to 2 dB gives better results using a linear filter type with an MGD classifier. When SNR is reduced to –2 dB, the *k*-NN algorithm outperforms the MGD algorithm regardless of the filter type. Mel filter type gives the best performance at SNR of 7 dB and 2 dB using the *k*-NN algorithm, but at –2 dB classification performance gives better results using a linear filter type.

Results in Fig. 5 clearly indicate that best overall performance is achieved if a linear or male scale filter was used.

Results in Table 5 show the classification matrix rate achieved by applying an MGD classification algorithm where different machinery operations have to be recognized. The perfect classification was achieved with an SNR of 7 dB and 2 dB. Decreasing SNR to –2 dB led to a misclassification, in which a drilling operation was classified as the operation of grinding an aluminium plate.

Table 6 shows results for the *k*-NN recognition of machinery operations. Very good classification performance was achieved for all SNR values with perfect classification results.

Results show that methods used in ASR systems can be successfully applied in MSR systems and can achieve high recognition accuracy even in noisy

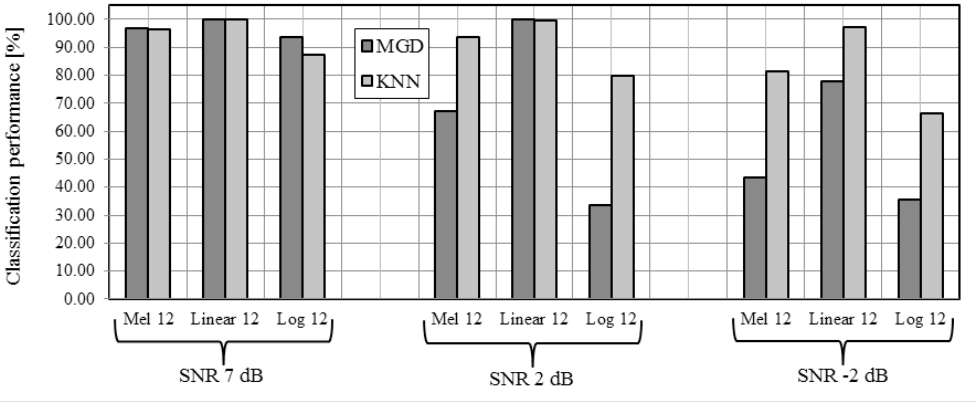

Fig. 5. *Impact of different filter compositions on classification performance of MGD and k-NN at SNR of 7 dB, 2 dB and -2 dB for different operational conditions of jigsaw*

conditions. A small modification of the FCC method and use of proper settings enables MSR working in real-time applications if the proper classifier is used.

Table 5. *Matrix of MGD classification performance at optimal FCC settings for different jigsaw operational conditions*

		Grinding	Drilling	Jigsaw - cutting
Linear-MGD classifier **SNR 7 dB**	Grinding	**100**	0	0
	Drilling	8.2	**90**	1.9
	Jigsaw - cutting	34.3	0.7	**65**
Linear-MGD classifier **SNR 2 dB**	Grinding	**100**	0	0
	Drilling	15.6	**79.4**	5
	Jigsaw - cutting	35.1	0.2	**64.7**
Linear-MGD classifier **SNR –2 dB**	Grinding	**99.9**	0	0.1
	Drilling	**49.7**	31.1	19.1
	Jigsaw - cutting	40	0	**60**

Table 6. *Matrix of k-NN classification performance at optimal FCC settings for different jigsaw operational conditions*

		Grinding	Drilling	Jigsaw - cutting
Linear-k-NN classifier **SNR 7 dB**	Grinding	**81.92**	16.67	1.42
	Drilling	0.11	**98.26**	1.63
	Jigsaw - cutting	2.61	29.25	**68.14**
Linear-k-NN classifier **SNR 2 dB**	Grinding	**75**	20.48	4.47
	Drilling	0	**92.7**	7.3
	Jigsaw - cutting	2.29	27.94	**69.77**
Linear-k-NN classifier **SNR –2 dB**	Grinding	**71.46**	20.59	7.95
	Drilling	0	**72.55**	27.45
	Jigsaw - cutting	0.65	25.65	**73.69**

4 CONCLUSIONS

A hypothesis proposing that automatic speech recognition algorithms can be applied for automatic machine recognition was tested. Two recognition algorithms (*k*-NN and MGD) were compared in combination with the FCC features extraction for three different SNRs. FCC feature extraction for automatic speech recognition based on a mel filter bank was modified through the modification of the filter bank. Two additional filter banks were developed to customize the FCC feature extraction for machinery-generated sound: linear and logarithmic. Performances of three different filter banks (mel, linear and logarithmic) were compared for the formation of feature vectors. Individual vector components were regarded to have univariate Gaussian distribution.

Experimental results confirm the hypothesis proposing that automatic speech recognition algorithms can be used for automatic machine recognition. The highest recognition rates of different machines classification were achieved by the MGD classifier in combination with linear filter type regardless of SNR. The results in Fig. 3 clearly show that a linear filter type in combination with MGD classifier should be used for machinery identification. However, classification performance of different machinery operations was better when using the *k*-NN algorithm in combination with male scale filter type, when SNR was low. When decreasing SNR to –2 dB, the linear filter type proves to be a better option.

Overall results of the experiment show that machinery noise features should be extracted using the proposed linear filter bank.

Despite the good classification results of different machinery operations, the *k*-NN might not be the best solution to use. Because it has no statistical model, it might not work well when a few more machinery operations would be added to an MSR procedure. Taking *k*-NN speed and database size into account, definitely makes the MGD algorithm more appropriate.

Algorithms of the proposed procedure are very fast, and the recognition can be performed in real-time. In further work, a full Gaussian mixture model should be tested for a further upgrade of machine classification performance.

The proposed procedure was already used in the system for the automatic classification of noise events during environmental noise measurements. It was also tested for the detection of cavitation phenomena on kinetic pumps and the quality inspection of suction units used in vacuum cleaners.

5 REFERENCES

[1] Germen, E., Basaran, M., Fidan, M. (2014). Sound based induction motor fault diagnosis using Kohonen self-organizing map. *Mechanical Systems and Signal Processing*, vol. 46, no. 1, p. 45-58, **DOI:10.1016/j.ymssp.2013.12.002**.

[2] Lu, W., Jiang, W., Yuan, G., You, L. (2013). A gearbox fault diagnosis scheme based on near-field acoustic holography and spatial distribution features of sound field. *Journal of Sound and Vibration*, vol. 332, no. 10, p. 2593-2610, **DOI:10.1016/j.jsv.2012.12.018**.

[3] Amarnath, M., Sugumaran, V., Kumar, H. (2013). Exploiting sound signals for fault diagnosis of bearings using decision tree. *Measurement*, vol. 46, no. 3, p. 1250-1256, **DOI:10.1016/j.measurement.2012.11.011**.

[4] Benko, U., Petrovic, J., Jurcic, D., Tavcar, J., Rejec, J. (2005). An approach to fault diagnosis of vacuum cleaner motors based on sound analysis. *Mechanical Systems and Signal Processing*, vol. 19, no. 2, p. 427-445, **DOI:10.1016/j.ymssp.2003.09.004**.

[5] O'Shaughnessy, D. (2008). Invited paper: Automatic speech recognition: History, methods and challenges. *Pattern Recognition*, vol. 41, p. 2965-2979, **DOI:10.1016/j.patcog.2008.05.008**.

[6] Furui, S. (2005). 50 years of progress in speech and speaker recognition research. *ECTI Transactions on Computer and Information Technology*, vol. 1, no. 2, **DOI:10.1121/1.4784967**.

[7] Goldhor, R.S. (1993). Recognition of Environmental Sounds. *IEEE International Conference on Acoustics, Speech, and Signal Processing*, p. 149-152, **DOI:10.1109/ICASSP.1993.319077**.

[8] Chu, S., Narayanan, S., Kuo, J. (2009). Environmental sound recognition with time-frequency audio features. *IEEE Transactions on Audio, Speech and Language Processing*, vol. 17, no. 6, **DOI:10.1109/TASL.2009.2017438**.

[9] Chachada, S., Kou, J. (2013). Environmental Sound Recognition: A Survey. *Signal and Information Processing Association Annual Summit and Conference*, **DOI:10.1109/APSIPA.2013.6694338**.

[10] Ntalampiras, S., Potamitis, I., Fakotakis, N. (2008). *New Directions in Intelligent Interactive Multimedia*. Springer, Berlin, Heidelberg, p. 147-153, **DOI:10.1007/978-3-540-68127-5_15**.

[11] Boela, Y., Grau, A., Pelissier, A., Sanfeliu, A. (2004). *Progress in Pattern Recognition, Image Analysis and Applications*. Springer, Berlin, Heidelberg, p. 287-295, **DOI:10.1007/b101756**.

[12] Kankar, P.K., Sharama, S.C. Harsha, S.P. (2011). Rolling element bearing fault diagnosis using wavelet transform. *Neurocomputing*, vol. 74, p. 1638-1645, **DOI:10.1016/j.neucom.2011.01.021**.

[13] Kakar, V.K., Kandpal, M. (2013). Techniques of acoustic feature extraction for detection and classification of ground vehicles. *International Journal of Emerging Technology and Advance Engineering*, vol. 3, no. 2, p. 419-426.

[14] Balsamo, L., Betti, R., Beigi, H. (2014). A structural health monitoring strategy using cepstral features. *Journal of Sound and Vibration*, vol. 333, p. 4526-4542, **DOI:10.1016/j.jsv.2014.04.062**.

[15] Marquez-Molina, M., Sanchez-Fernandez, L.P., Suarez-Guerra, S., Sanchez-Perez, L.A. (2014). Aircraft take-off noises classification based on human auditory's matched features extraction. *Applied Acoustic*, vol. 84, p. 83-90, **DOI:10.1016/j.apacoust.2013.12.003**.

[16] Prezelj, J. (2015). Patent SI 24518 A. *Sistem za avtomatski monitoring hrupa in za klasifikacijo virov hrupa v opazovanem okolju (Eng: System for Automatic Noise Sourvce Identification and Classification).* Slovenian Intellectual Property Office, Ljubljana.

[17] Čudina, M., Prezelj. J. (2009). Detection of cavitation in situ operation of kinetic pumps: effect of cavitation on the characteristic discrete frequency component. *Applied Acoustics*, vol. 70, no. 9, p. 1175-1182, **DOI:10.1016/j.apacoust.2009.04.001**.

[18] Peeters, G., Rodet, X. (2002). Automatically selecting signal descriptors for sound classification. *International Computer Music Conference*, Goteborg.

[19] Islam, R., Rahman, F. (2009). Codebook design method for noise robust speaker identification based on genetic algorithm. *International Journal of Computer Science and Information Security*, vol. 4, no. 1.

[20] Ganchev, T. (2011). *Contemporary Methods for Speech Parameterization*. Springer, New York, Dordrecht, Heidelberg, London, **DOI:10.1007/978-1-4419-8447-0**.

[21] Zheng, F., Zhang, G., Song, Z. (2001). Comparison of Different Implementation of MFCC. *Journal of Science & Technology*, vol. 16, no. 6, p. 582-589, **DOI:10.1007/BF02943243**.

[22] Sigurdsson, S., Petersen, K.B., Lehn-Schioler, T. (2006). Mel frequency coefficients: An evaluation of robustness of MP3 encoded music. *Proceedings of the 7th International Conference on Music Information Retrieval*.

[23] Muda, L., Begam, M. Elamvazuthi, I. (2010). Voice recognition algorithms using mel frequency cepstral coefficient (MFCC) and dynamic time warping (DTW) techniques. *Journal of Computing*, vol. 2, no. 3, p. 138-143.

[24] Mengusoglu, E. (2015). Speaker model adaptation based on confidence score. *Tehnički vjestnik - Technical Gazzete*, vol. 22, no. 4, p. 873-878, **DOI:10.17559/TV-20140120095957**.

[25] Saini, I., Singh, D., Khosla, A. (2013). QRS detection using k-nearest neighbor algorithm (KNN) and evaluation on standard ECG database. *Journal of Advance Research*, vol. 4, p. 331-334, **DOI:10.1016/j.jare.2012.05.007**.

[26] Izenman, A.J. (2008). *Modern Multivariate Statistical Techniques*. Springer Science+Buisiness Media, New York, **DOI:10.1007/978-0-387-78189-1**.

Strojniški vestnik - Journal of Mechanical Engineering 61(2015)12, 709-713
DOI:10.5545/sv-jme.2015.2733
Original Scientific Paper
Received for review: 2015-06-05
Received revised form: 2015-09-03
Accepted for publication: 2015-10-14

Evaluation of the Coulomb Friction Coefficient in DC05 Sheet Metal Forming

Gillo Giuliano*
University of Cassino, DICeM, Italy

This paper describes the identification of the Coulomb friction coefficient for sheet metal forming using a comparison between numerical and experimental results. Using finite element method, the work examines some aspects of the Erichsen test in order to measure the interfacial friction. Preliminary results on the evaluation of a typical tool-workpiece interface are shown for a stainless steel punch vs. a DC05 sheet metal.

Keywords: Coulomb friction coefficient, sheet metal forming, finite element method, Erichsen test

Highlights

- *The proposed method examines the Coulomb friction coefficient for sheet metal forming by using the finite element method and experimental results of the Erichsen test.*
- *Experiments were conducted with a stainless steel punch and DC05 steel sheet metal.*
- *Specimens were tested in a non-lubricated condition as well as using Grease LB4.*
- *The numerical-experimental comparison can be considered to be in good agreement especially if using Grease LB4.*

0 INTRODUCTION

During the sheet metal-forming processes, whenever the tools and the workpiece are in contact, tangential frictional forces between the sheet metal and the tools are generated. Since the metal flow, the product's cost and quality, and die wear are affected by friction, its effects must be reduced by means of lubricants [1].

In order to accurately analyse sheet metal-forming processes, finite element method analysis (FEM) is mostly used. FEM analysis require this modelling of metal sheet's mechanical properties and friction between the sheet and the tools used for the forming process. Among the various models of friction described in literature [2], Coulomb's friction model is the most suitable in cold forming process and when sheet and tools interact significantly.

In this paper, commercial finite element software MSC.Marc is used; it defines friction forces as follows:

$$f_t \leq -\mu f_n t, \tag{1}$$

where f_t is the tangential force, f_n the normal pressure, μ the friction coefficient and t the tangent unit vector [3].

The mechanical properties of the sheet have been obtained by means of a standard test at room temperature [4]. The material's constitutive equation is:

$$\sigma = K\varepsilon^n, \tag{2}$$

where K is the strength coefficient and n is the strain-hardening exponent.

In order to calculate the friction coefficient, Erichsen's standard test is applied, which, unlike the ones commonly used [5] to [9], is much simpler; moreover, with this test it is possible to determine the properties of the sheet material, as shown in [10].

In [10] to [13] it was shown that the main test output is represented by d/d_0 where d_0 is the distance between the punch axis and the blankholder's internal surface, whereas d is the distance between the fracture line and the blankholder's internal surface (see Fig. 1a).

The original distance criterion introduced in [10] to [13], being independent of the values of the material constants, simplifies determining the value of the friction coefficient.

In [12], the influence of the friction on the results of the Erichsen test was analysed. Two types of aluminium alloys were selected as the experimental materials. It was seen that lubrication does not considerably affect the load-displacement curve, whereas it causes a noticeable increase in the ratio d/d_0 and a reduction in the thickness evaluated at the apex of the specimen. In general, it can be said that lubrication increases formability under biaxial stretching conditions.

In this paper, Erichsen test experiments were conducted with a stainless steel punch and DC05 steel sheet metal in order to evaluate the friction coefficient. DC05 is non-ageing, low carbon steel, which is especially suited for deep drawing and for particular applications, such as automotive components and body panels, components for building, domestic

*Corr. Author's Address: University of Cassino, DICeM, via Di Biasio, 43, 03043 Cassino, (FR) Italy giuliano@unicas.it

Table 1. *Chemical composition and mechanical properties of DC05*

Engineering properties					Chemical composition			
Re max [N/mm²]	Rm [N/mm²]	All% min		Vickers hardness max	C % max	P % max	S % max	Mn % max
		A80	A50					
180	270÷330	40	42	100	0.06	0.025	0.025	0.35

appliances, etc. The engineering properties and the chemical composition of the studied steel are given in Table 1. Specimens are tested in non-lubricated condition as well as using Grease LB4.

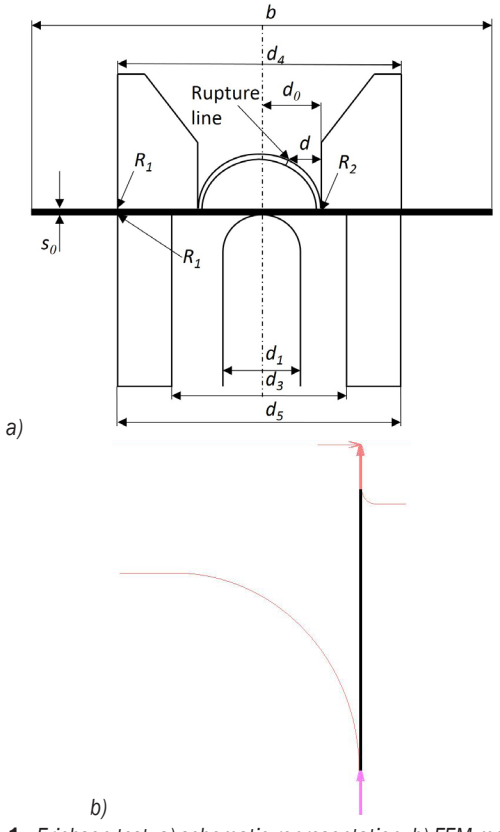

Fig. 1. *Erichsen test; a) schematic representation, b) FEM model*

1 FEM MODELLING

In this paper, two types of tests were simulated using the commercial finite element software MSC.Marc. Fig. 1a shows the schematic diagram of the tools used in the test. The size of the tools, marked with the letter A_0 in Table 2, is relative to a standardized Erichsen test [14]. A second series of tests was performed using amplified tools size (indicated by the letter A_1 in Table 2) and obtained by multiplying the geometry A_0 by a factor of 5.

Fig. 1b shows the fem schematization of the problem analyzed by geometry A_1, but it can also represent geometry A_0. Since the model is axisymmetric, only half of the cross-section is represented. With geometry A_1, the deformable sheet is discretized in 1312 elements ordered in four rows with 1645 nodes. Geometry A_0 uses 384 elements in four rows with 485 nodes. Element type is a four-node, isoparametric, arbitrary quadrilateral written for axisymmetric applications (15). It is hypothesized that the sheet material has a rigid-plastic behaviour according to the model presented in Eq. (2).

Table 2. *Symbols and designations*

Symbol	Designation	Dimension [mm] Standard test	
		A_0	A_1
s_0	Thickness of the test piece	0.7	0.7
b	Diameter of the test piece	90	450
d_0	Inner radius of the blankholder	13.5	67.5
d_3	Diameter of the die	16.5	82.5
d	Distance projected on the initial surface of the sheet and measured between the rupture line and the inner surface of the blankholder		
d_1	Diameter of the spherical end of the punch	20	100
d_4	Outside diameter of the blankholder	55	275
d_5	Outside diameter of the die	55	275
R_1	Outside corner radius of the die and the blankholder	0.75	3.75
R_2	Inside corner of the blankholder	0.75	3.75

Fig. 1b highlights two rigid bodies (punch and die are considered to be rigid bodies thus not influenced by mechanical stress in the forming process), the sheet (whose discretization is too thick to be represented) and boundary conditions. Notably on the symmetry axis, the nodes are characterized by a zero displacement in the orthogonal direction to the symmetry axis. The blankholder is not represented, but its effects are replaced by displacement boundaries at nodes placed in the sheet periphery.

The Coulomb friction model is used between the sheet and the tools surfaces.

FEM analysis is used to determine the influence of the K, n and μ parameters on the Erichsen test results in terms of thickness distribution and locus of

thinning. K value ranges between 100 MPa and 1000 MPa, n and μ vary in the range 0 to 0.5. The results are highlighted using the strain distribution in the finished component.

2 EXPERIMENTAL

The Erichsen test, schematically shown in Fig. 1, is a stretch forming test. It is carried out using a machine specially projected in Cassino University. The punch and the die have been realized in stainless steel.

An Erichsen test on DC05 sheet metal is analyzed. The specimens, of circular shape, were obtained by laser cutting, and are characterized by a diameter equal to 92 mm and a thickness of about 0.7 mm. Fig. 2 shows an undeformed specimen and a specimen deformed in the non-lubricated condition.

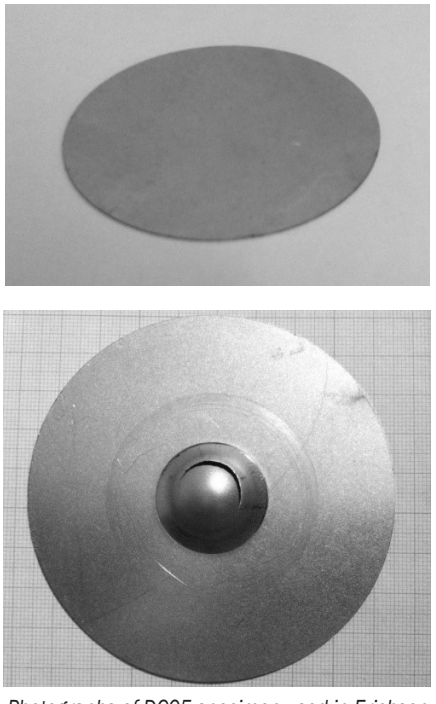

Fig. 2. *Photographs of DC05 specimen used in Erichsen test; a) undeformed specimen, b) deformed specimen*

The test consists of the deformation of a circular sheet clamped between the die and the blankholder by a force of 10 kN, through a spherical punch. The sheet is deformed until a fracture line is reached. The punch displacement once the break is obtained represents, in millimetres, Erichsen index, which is a measure of the sheet formability.

The testing machine **[10]** to **[12]** comprises a workbench on which was set the die containing the circular sheet metal to be tested. The punch was mounted on a vertically-translating machine's crossbeam. The translation movement is produced by two large screws connected to an electric motor through a chain. After a rapid acceleration phase of the beam, the punch pushes the sheet at a constant speed until the break is reached.

At any given moment, by using a laser and a load cell, the pair of load-displacement points is recorded.

To investigate the effect of friction on formability, DC05 specimens are tested both in a non-lubricated condition and using Grease LB4 (lithium grease containing solid lubricant MoS_2) manufactured with RS 200 motor oil. Black in colour it is used as an alternative to graphite grease for industrial applications.

Tests have been repeated five times and have been carried out at a speed of 0.27 mm/s. Erichsen index (EI), the thickness measured at the specimen apex, s and distance between the fracture line and the blankholder's internal surface, d, were recorded in every test. EI was measured with a measuring laser, s with a digital comparator and d, represented in Fig. 1a, was obtained via a CAD reconstruction of the specimen, as shown in **[12]**.

3 RESULTS AND DISCUSSION

The results of numerical simulations, in terms of thickness and locus of thinning, are independent from the value of K adopted (K ranges between 100 MPa and 1000 MPa).

For n equal to 0.5, Fig. 3, which refer to the results obtained by using the geometry A_1 (punch stroke of 50 mm) but are also indicative of the tests made at geometry A_0, show the values assumed by the principal strains on the top surface of the sheet metal.

In the lubricated condition ($\mu = 0$), the maximum strain (meridional strain) is almost constant in the contact zone between the sheet and the punch while the intermediate strain (circumferential strain) decreases. Therefore, the strain along the thickness (minimum strain) is minimum on the axis of symmetry and increases moving away from the centre. In the non-lubricated condition ($\mu > 0$), the circumferential strain is slightly significant while the meridional strain increases up to the point where it locates the strain then decreases by moving further from the centre.

Fig. 4 relative to geometries A_0 and A_1 shows the distance d, versus the punch displacement for different values of the friction coefficient (d is the distance between the fracture line and the blankholder's internal surface, see Fig. 1a). In **[11]**, it was found that if the friction coefficient is fixed, the parameter n has

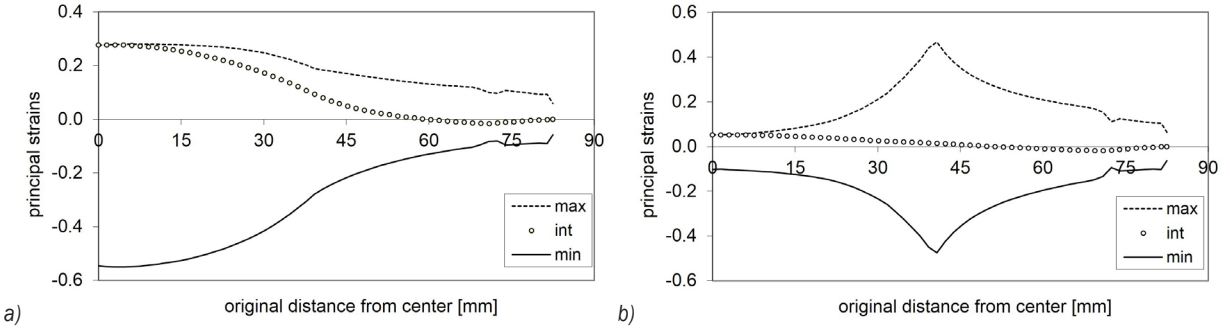

Fig. 3. *Geometry A_1: principal strains profile in different conditions of lubrication (n = 0.5); a) lubricated condition (μ = 0); and b) non-lubricated condition (μ = 0.3)*

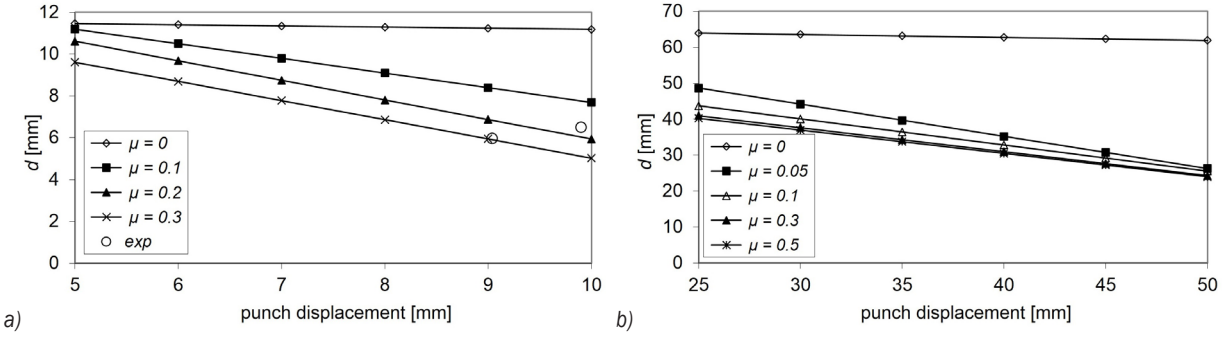

Fig. 4. *Relation d-punch displacement when varying the friction coefficient; a) A_0 geometry and b) A_1 geometry*

little effect on the results. Therefore, the results shown in Fig. 4 may also be considered independent from the value of strain hardening coefficient [11].

Fig. 4b shows that, for the geometry A_1, in the lubricated condition ($\mu = 0$) the thinning is localized near the apex of the specimen (d is constant). In addition, it is noted that, in the non-lubricated condition ($\mu > 0$), the region where the thinning is located moves away from the apex of the sheet (d decreases) increasing the stroke of the punch and is not very dependent on the friction coefficient. In contrast, the figure relative to geometry A_0 (Fig. 4a) shows a greater sensibility to the value assumed by the friction coefficient. Therefore, to determine the friction coefficient the configuration A_0 will be used.

The friction developing between the punch and the sheet exerts a great influence on test results. To reduce the effects of the friction in experimental activity, a series of tests were conducted by interposing Grease LB4 between the two surfaces in contact.

Table 3 presents the results obtained in the different test conditions. The variables s, d and EI (Erichsen index) are represented in Fig. 1. Table 3 shows that:

- the value of the thickness, s, measured at the end of the test at the specimen apex, is strongly influenced by lubrication conditions. Indeed, the presence of the lubricant facilitates the sliding of the punch on the sheet, favouring its thinning. The numerical modelling of this process has made it possible to determine that the meridional strain (maximum strain), in lubrication condition, is distributed in a decreasing trend from the centre to the edge of the specimen (Fig. 3). The absence of lubricant changes the meridional strain distribution, shifting the maximum value far from the apex of the specimen in a position that varies with the value of the friction coefficient between the punch and the sheet itself. The minimum thickness value of the specimen and, therefore, the region of the sheet that will be subject to break after the end of the test are associated to the zone of maximum meridional strain;
- the distance, d, tends to increase in the case of lubrication, the rupture line moving to the apex of the specimen;
- the value of the Erichsen index (EI) is high in the lubricated test because the sheet is subjected to uniform strain distribution.

Table 3. *Erichsen test results for non-lubricated condition (absence of lubricant) and for lubricated condition (Grease LB4)*

	Non-lubricated condition	Lubricated condition
s [mm]	0.63	0.55
d [mm]	5.95	6.49
EI [mm]	9.04	9.90

For the evaluation of the friction coefficient we refer to the results reported in Fig. 4a.

Fig. 4a shows the FEM results, based on the distance, d, and obtained with different friction coefficients. The comparison with the results of the real sheet metal process allows determination of the corresponding friction coefficient.

Through the FEM results shown in Fig. 4a, it is possible to determine the relation d–μ once the punch displacement is set. Since in Fig. 4a the lines of different friction coefficients are unparalleled, the determined relations differ when varying the punch displacement.

The Coulomb friction coefficient is equal to 0.29 and 0.17 in non-lubricated condition and using Grease LB4, respectively. These values have been used to simulate the Erichsen test. The numerical simulation underestimates the experimental value of the thickness at the apex of the specimen providing a percentage error at the end of the test of 14 % and 9 % in non-lubricated and lubricated conditions, respectively. Conversely, the distance d is overestimated by 12 % and 2 % respectively.

4 CONCLUSIONS

Through geometry A_0 (standard Erichsen test), an experimental-numerical process was used to determine the Coulomb friction coefficient in the punch/sheet interface.

In this paper, experiments were conducted with a stainless steel punch and DC05 steel sheet metal using the forming apparatus designed at the Laboratory of Cassino University. Specimens were tested in a non-lubricated condition as well as using Grease LB4.

The Coulomb friction coefficient was 0.29 in non-lubricated conditions and 0.17 when Grease LB4 lubricant was used. Two numerical simulations of the Erichsen test were conducted through such values of friction coefficient. Comparing the experimental results with those of the numerical simulation, the latter, in terms of thickness measured at the specimen apex, are underestimated (with an error of 14 % and 9 % respectively in non-lubricated and lubricated conditions) while in terms of distance, d, they are overestimated (with an error of 12 % and 2 % respectively). Thus, the numerical-experimental comparison can be considered to be in good agreement especially, if using Grease LB4.

5 REFERENCES

[1] Kalpakjian, S., Shmid, S.R. (2009). *Manufacturing Engineering and Technology*. Prentice Hall, Upper Saddle River.

[2] Joun, M.S., Moon, H.G., Choi, I.S., Lee M.C., Jun B.Y. (2009). Effects of friction laws on metal forming processes. *Tribology International*, vol. 42, no. 2, p. 311-319, **DOI:10.1016/j.triboint.2008.06.012**.

[3] MSC.Marc (2005). *User Information, A*, MSC Software Corporation, Newport Beach.

[4] Davis. J.R. (2004). *Tensile Testing*. ASM International, Ohio.

[5] Sofuoglu, H., Rasty, J. (2000). On the measurement of friction coefficient utilizing the ring compression test. *Tribology International*, vol. 32, no. 4, p. 327-335, **DOI:10.1016/S0301-679X(99)00055-9**.

[6] Sutcliffea, M.P.F., Combarieu, R., Montmitonnet, P. (2004). Effect of additives on friction during plane strain compression of aluminium strip. *Wear*, vol. 257, no. 9-10, p. 1071-1080, **DOI:10.1016/j.wear.2004.07.001**.

[7] Yoon, E., Kong, H., Kwon, O., Oh, J. (1997). Evaluation of frictional characteristics for a pin-on-disk apparatus with different dynamic parameters. *Wear*, vol. 203-204, p. 341-349, **DOI:10.1016/S0043-1648(96)07365-6**.

[8] Cho, H., Altan, T. (2005). Determination of flow stress and interface friction at elevated temperatures by inverse analysis technique. *Journal of Material Processing Technology*, vol. 170, no. 1-2, p. 64-70, **DOI:10.1016/j.jmatprotec.2005.04.091**.

[9] Lam, Y.C., Khoddam, S., Thomson, P.F. (1998). Inverse computational method for constitutive parameters obtained from torsion, plane strain and axisymmetric compression test. *Journal of Material Processing Technology*, vol. 83, no. 1-3, p. 62-71, **DOI:10.1016/S0924-0136(98)00029-6**.

[10] Giuliano, G. (2013). AA5083 Aluminium alloy constants identification through inverse analysis of the Erichsen test. *Applied Mechanics and Materials*, vols. 271-272, p. 208-211, **DOI:10.4028/www.scientific.net/AMM.271-272.208**.

[11] Giuliano, G. (2012). Influence of the metal sheet parameters on the results of the Erichsen test. Applied Mechanics and Materials, vols. 217-219, p. 2444-2447, **DOI:10.4028/www.scientific.net/AMM.217-219.2444**.

[12] Giuliano, G., Samani, F. (2013). Effect of lubrication on the Erichsen test. *Applied Mechanics and Materials*, vols. 365-366, p. 425-428, **DOI:10.4028/www.scientific.net/AMM.365-366.425**.

[13] Giuliano, G. (2013). Evaluation of the Coulomb friction coefficient by the Erichsen test. *Applied Mechanics and Materials*, vols. 365-366, p. 1190-1193, **DOI:10.4028/www.scientific.net/AMM.365-366.1190**.

[14] ISO 20482 (2003). *Erichsen cupping test*, International Organization for Standardization, Geneva.

[15] MSC.Marc, (2005). *Element Library, B*. MSC Software Corporation, Newport Beach.

Strojniški vestnik - Journal of Mechanical Engineering 61(2015)12, 714-720

DOI:10.5545/sv-jme.2015.2717 Original Scientific Paper
Received for review: 2015-05-29
Received revised form: 2015-09-15
Accepted for publication: 2015-11-09

Prediction of Laser Cut Quality for Tungsten Alloy Using the Neural Network Method

Simon Klancnik[1] – Derzija Begic-Hajdarevic[2,*] – Matej Paulic[1] – Mirko Ficko[1] – Ahmet Cekic[2] – Maida Cohodar Husic[2]

[1]University of Maribor, Faculty of Mechanical Engineering, Slovenia
[2]University of Sarajevo, Faculty of Mechanical Engineering, Bosnia and Herzegovina

The cut quality is of great importance during the laser cutting process. The quality of laser cut mainly depends on an appropriate selection of process parameters. In this paper, the effect of process parameters was analysed on the laser cut quality of an uncommon alloy, the tungsten alloy (W ≈ 92.5 % and the remainder Fe and Ni) sheet with thickness of 1 mm. This alloy has a wide application in different industrial areas, e.g. in medical applications, the automobile sectors, and the aircraft industry. This paper introduces a developed back-propagation artificial neural network (BP- ANN) model for the analysis and prediction of cut quality during the CO_2 laser cutting process. In the presented study, three input process parameters were considered such as laser power, cutting speed and assist gas type, and two output parameters such as kerf width and average surface roughness. Amongst the 42 experimental results, 34 data sets were chosen for training the network, whilst the remaining 8 results were used as test data. The average prediction error was found to be 5.5 % for kerf width and 9.5 % for surface roughness. The results of the predicted kerf width and surface roughness by the BP-ANN model were compared with experimental data. Based on the results of the study, it was shown that the proposed artificial neural network model could be a useful tool for analysing and predicting surface roughness and kerf width during CO_2 laser cutting processes.

Keywords: laser cutting, cut quality, artificial neural network, tungsten alloy

Highlights

- *Influence of process parameters on cut quality in CO_2 laser cutting of tungsten alloy.*
- *Development of BP-ANN model for prediction of kerf width and surface roughness for CO_2 laser cutting process.*
- *Proposed ANN model is adequate for prediction of laser cut quality.*
- *The type of assist gas has the most significant effect on the laser cut quality especially on the kerf width in CO_2 laser cutting of tungsten alloy.*

0 INTRODUCTION

Laser beam machining is a thermal energy-based advanced machining process during which material is removed by melting and/or vaporisation. Interest in predicting the materials' removal phenomena has existed since the beginning of the exploitation of laser beams for cutting. The laser cutting process can be applied to a wide range of materials using different technological procedures. Modelling based on an analytical solution is usually centred on certain assumptions and is sometimes unable to solve the whole system in practical cases [1]. The focus was firstly on the modelling of the process, which is difficult to model because of the high numbers and substantial varieties of influential parameters. Secondly, attention was focused on the results of cutting such as geometry of kerf and correspondingly cut quality. No general model was established because of the many process parameters and very different physical processes which are present during the laser cutting process. Despite this, users need solutions for predicting possible economic exploitations of the laser cutting process. Artificial neural network, fuzzy expert systems, genetic algorithms are common for the production of machining models [2] to [4]. Artificial intelligence methods mostly use experimental data for generating models [1]. In regard to the cut quality according to the input parameters, the work is going in the direction of researching uncommon materials or analysing the cuttings of different cut shapes such as wedge surfaces. A special point of interest is analysing the cut surface roughness and kerf shape [5].

Further analyses of interest are especially uncommon materials and alloys where the common knowledge is inapplicable [6]. The effects of laser power, cutting speed and oxygen assist gas pressure on the cut qualities in CO_2 laser cutting of tungsten alloy were analysed in [7]. Regression analysis has been used for the developments of empirical models able to describe the effects of the process parameters on the CO_2 laser cut qualities of the Inconel 718 nickel – based super alloy [8]. In [9] regression models were developed for kerf taper and surface roughness after laser cutting of titanium alloy where the factors are determined by genetic algorithms. The fuzzy expert system was used to predict the laser cut quality of Incoloy alloy 800, the input parameters

*Corr. Author's Address: Univeristy of Sarajevo, Mechanical Faculty, Vilsonovo setaliste 9, Sarajevo, Bosnia and Herzegovina, begic@mef.unsa.ba

of the prediction system in [5] are power, assist gas pressure and cutting speed and the output parameters are surface roughness and dross inclusion. Multiple regression analysis is used for predicting the surface roughness and widths of heat-affected zones during the CO_2 laser cutting of alloy steels using nitrogen as assist gas [10]. A multiple regression analysis and an artificial neural network are used to predict the depths of the cutting line, widths of heat affected zone and cutting line during the laser cutting of epoxy and copper-compounded epoxy [11]. The predicting model includes three input parameters such as current, frequency and cutting speed. At the end, a genetic algorithm is implemented to optimise the parameters for faster cutting speed and least heat-affected zone. A neural network is introduced to classify the striation patterns of the cut surfaces during CO_2 laser cutting of the wedge surfaces [12]. The work is also extended in the modelling and experimenting of laser cutting porous material, correspondingly of aluminum foam [13]. Models for predicting cut quality or kerf shape are based on factorial analysis in [8] or genetic algorithms in [9] and [11], neural networks in [11] and [12] and fuzzy expert systems in [5].

However, we did not find in the literature many studies that had considered the CO_2 laser cutting of refractory materials. For this reason, in the presented study, a back-propagation artificial neural network model has been applied for predicting the cut quality during the CO_2 laser cutting of tungsten alloy sheet. The important quality characteristics related to laser cutting of sheets are kerf width, surface roughness, heat affected zone [14]. Kerf width and average surface roughness have been considered as quality characteristics in this paper.

Section 1 describes experimental setup, Section 2 presents a BP-ANN-based model for predicting quality characteristics, and Section 3 presents the results and discussion. The conclusion is given in Section 4.

1 EXPERIMENTAL SETUP

The experiments were carried out on a Rofin CO_2 laser system (model DC020) with a nominal output power of 2000 W in CW mode at a wavelength of 10.6 μm with a high quality beam (beam quality factor K = 0.95). The experimental investigations were conducted at the University of Applied Science Jena in Germany. Tungsten alloy (W ≈ 92.5 % and the remainder Fe and Ni) sheet with thickness of 1mm was used for experimentation. The products manufactured of the tungsten alloy sheets have found new possibilities for applications within different industrial areas, e.g. in medical applications, the automobile sectors, and the aircraft industry. The laser beam was focused using a ZnSe focusing lens with focal length of 127 mm. Diameter of focusing lens was 38.1 mm. The laser spot diameter at the focal point is measured to be about 0.21 mm, it is applied the inclined plane method. Assist gas was used coaxially with the laser beam via a 2 mm exit diameter nozzle. Focus position, nozzle stand of distance (stand-off) and assist gas pressure were kept constant throughout the main experimentation. The optimal values of these process parameters were selected based on a previous experimental study [15] for each of assist gasses (oxygen, nitrogen and air). A full cut, with an acceptable kerf width, cutting edge striations and dross to a minimum; were the criteria of selecting optimal values of these parameters. Three input process parameters were selected for analysis at the presented study. These are laser power, cutting speed and assist gas type. The working range of cutting speed was selected based on a previous experimental study [15] for each assist gas type and a certain laser power. The range of process parameters utilised is summarised in Table 1. Testing the effect of one parameter on the cut quality requires the variation of one parameter whilst keeping the other two parameters at the pre-selected values.

The controlled parameters were the top surface kerf width and the surface roughness. Visual inspections of each cut were carried out to ensure that no pitting and burrs were present within the cut areas. The sample geometry of the measurements taken are shown in Fig. 1.

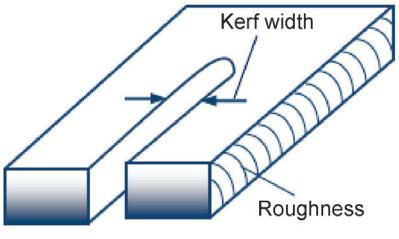

Fig. 1. *The sample geometry*

Table 1. *Input process parameters and their levels used in the experiments*

Assist gas type	Laser power [W]	Cutting speed [mm/min]	Gas pressure [bar]	Focus position [mm]	Stand-off [mm]
Oxygen	1500 to 2000	3000 to 6000	12.5	-0.5	1
Nitrogen	1500 to 2000	1000 to 2250	15	-0.5	0.75
Air	1500 to 2000	2000 to 4500	15	-1	1

Surface roughness on the cut edge was measured in terms of the average roughness R_a, using a Taylor-Hobson stylus instrument. Roughness was measured along the length of a cut approximately in the middle of the thickness. Five consistent surface roughness values of each sample were measured and an average value was calculated for each sample.

The kerf width was measured using a Stemi optical microscope fitted with a video camera and a zoom lens. Kerf width was measured in the microscope images of each sample at five different places and an average value was calculated for each sample.

2 BACK-PROPAGATION ARTIFICIAL NEURAL NETWORK BASED MODEL

A multilayer feed-forward neural network with back-propagation algorithm (BP-ANN) was used to model the laser cutting process. BP-ANN is one of the more widely used artificial neural networks. It is constructed of an input layer, output layer and one

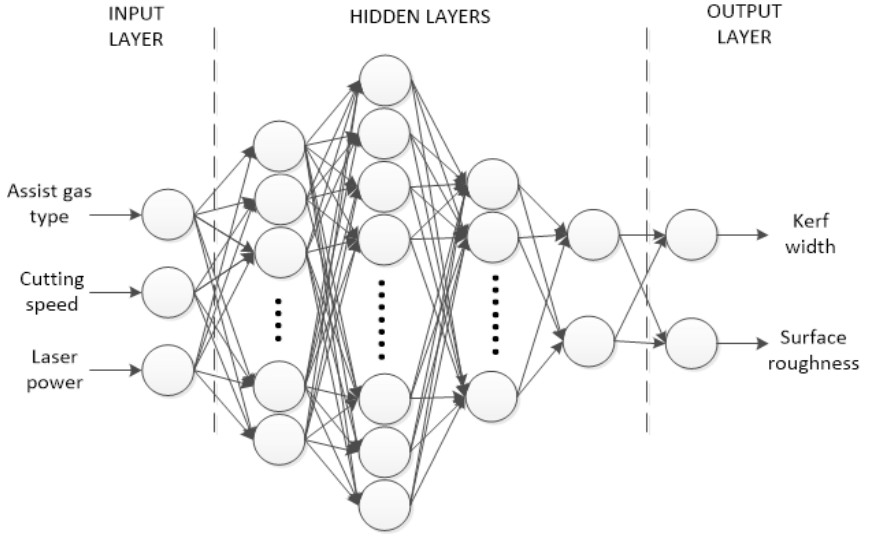

Fig. 2. *Back-propagation artificial neural network used for predicting kerf width and surface roughness*

Table 2. *Experimental data used as training database*

No.	Assist gas type	Power [W]	Speed [mm/min]	Kerf [mm]	Ra [μm]	No.	Assist gas type	Power [W]	Speed [mm/min]	Kerf [mm]	Ra [μm]
1	Oxygen	2000	3000	0.35	7.73	18	Nitrogen	1750	1000	0.20	5.33
2	Oxygen	2000	3500	0.34	722	19	Nitrogen	1750	1500	0.19	5.57
3	Oxygen	2000	4000	0.34	7.18	20	Nitrogen	1750	2000	0.18	6.56
4	Oxygen	2000	5000	0.29	6.01	21	Nitrogen	1500	1000	0.17	5.82
5	Oxygen	2000	6000	0.27	3.73	22	Nitrogen	1500	2000	0.19	4.97
6	Oxygen	1750	3000	0.34	7.78	23	Air	2000	2000	0.24	7.17
7	Oxygen	1750	3500	0.33	8.22	24	Air	2000	3000	0.23	4.66
8	Oxygen	1750	4500	0.32	6.25	25	Air	2000	3500	0.23	4.50
9	Oxygen	1750	5000	0.27	7.13	26	Air	2000	4000	0.23	3.52
10	Oxygen	1750	5500	0.31	5.97	27	Air	2000	4500	0.23	2.77
11	Oxygen	1500	3000	0.35	7.75	28	Air	1750	2000	0.24	5.46
12	Oxygen	1500	3500	0.32	7.58	29	Air	1750	2500	0.23	3.95
13	Oxygen	1500	4000	0.29	6.79	30	Air	1750	3000	0.23	3.80
14	Oxygen	1500	4500	0.28	6.02	31	Air	1750	4000	0.23	3.77
15	Nitrogen	2000	1000	0.20	5.41	32	Air	1500	2000	0.24	5.24
16	Nitrogen	2000	1500	0.19	5.92	33	Air	1500	3000	0.22	4.04
17	Nitrogen	2000	2250	0.19	7.14	34	Air	1500	3500	0.23	2.76

or more hidden layers. Using a back-propagation algorithm, the weights and biases were adapted to minimise the mapping error.

In the presented study, the neural network was used with an input layer having three neurons, four hidden layers with 8-15-5-2 number of neurons in each of the hidden layers and an output layer with two neurons, as shown in Fig. 2. This configuration was found to be the most suitable network architecture with the lowest mean prediction error [%] for our problem. The appropriate architecture for the artificial neural network was selected through an exhaustive examination of a number of network configurations. This was accomplished by changing the number of hidden layers and number of neurons in the hidden layer. Three input variables, namely: assist gas type (oxygen, nitrogen or air), laser power [W] and cutting speed [mm/min] and two output variables namely: surface roughness [μm] and kerf width [mm] are used in the developed model, see Fig. 2. Experimental data were used to train the network. Amongst the 42 experimental results, 34 data sets were chosen for training the network (Table 2), whilst the remaining 8 results were used as test data (Table 3). All the data sets variables were normalised between 0 and 1, except for assist gas where the values were for Oxygen 0, Nitrogen 0.5 and for Air 1.

Table 3. *Experimental data used as testing database*

No.	Assist gas type	Power [W]	Speed [mm/min]	Kerf [mm]	Ra [μm]
1	Oxygen	2000	4500	0.31	6.14
2	Oxygen	2000	5500	0.27	4.49
3	Oxygen	1750	4000	0.32	6.80
4	Nitrogen	2000	2000	0.18	6.23
5	Nitrogen	1500	1500	0.18	5.41
6	Air	2000	2500	0.24	4.92
7	Air	1750	3500	0.22	3.33
8	Air	1500	2500	0.23	3.30

3 RESULTS AND DISCUSSION

In order to assess the network properly only 116 epochs of learning were sufficient for training. The network should be learnt to approximate but not to fit exactly the showed pattern just in the case of predicting future reliable results when the range of the input signals changes slightly. That is the reason why the number of training epochs should not be too high.

During the network learning the neurons covered various activated positions. Some neurons were activated more than others. The changes in activities of the neurons were important because they showed the behaviour of the network and the different values of the connections' weights. The higher was the value of the weight the stronger the influences and impacts on the neuron. In the created network the bias value

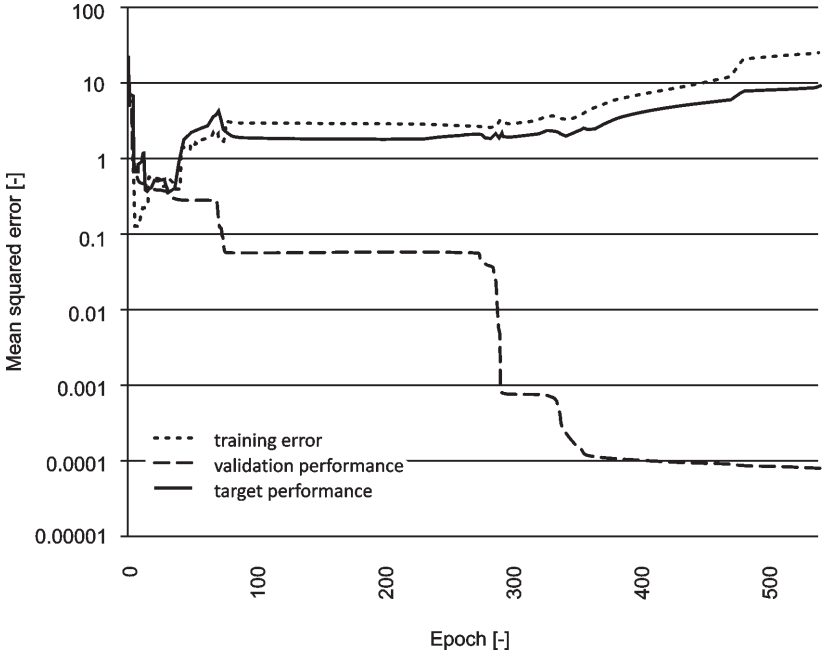

Fig. 3. *Training performance of BP-ANN*

was very important when relating to the training process. Bias is a neuron in which the activation function is permanently set at 1. Just as with other neurons, a bias connects to the neurons in the layer above via a weight which is often called threshold.

Despite the fact that the size of the training data set is not very large (34 samples) the performance of the BP-ANN whilst training was good, as shown in Fig. 3. The results of BP-ANN modelling (learning - training) are displayed in Figs. 4 and 5.

The modelling seemed to be quite promising when we were concerned that the average training error of kerf width was 3.69 % and the average training error of surface roughness was 4.45 %. In the prediction step the dispersion between experimental and predicted values was quite small. The average prediction error of kerf width was 5.5 % and the average prediction error of surface roughness was smaller than 10 %. The results of BP-ANN predictions for each test sample are shown in Figs. 6 and 7.

4 CONCLUSION

In the presented study, artificial neural network was used for predicting kerf width and surface roughness during the CO_2 laser cutting of tungsten alloy sheet. It is evident that the prediction error of kerf width is smaller than the prediction error of surface roughness

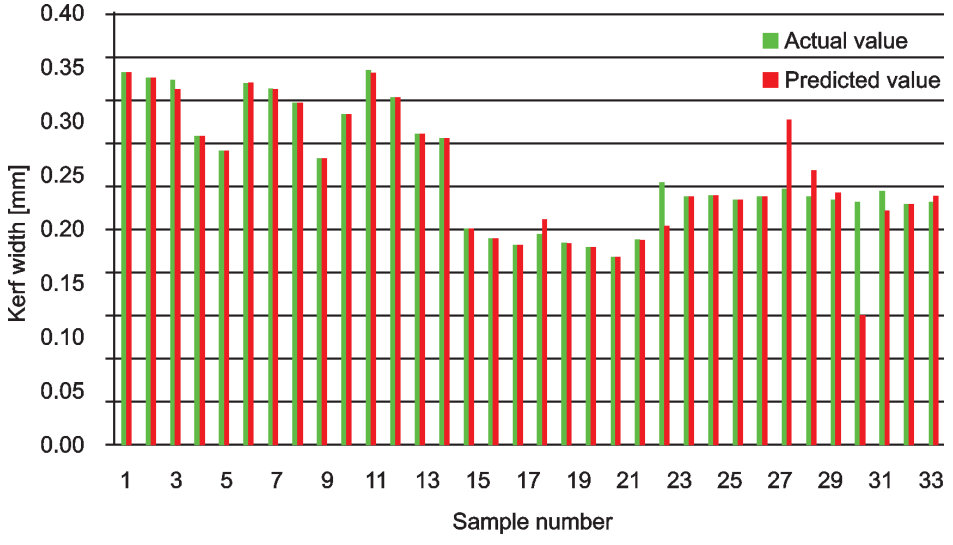

Fig. 4. *Actual and predicted values of BP-ANN training for kerf width*

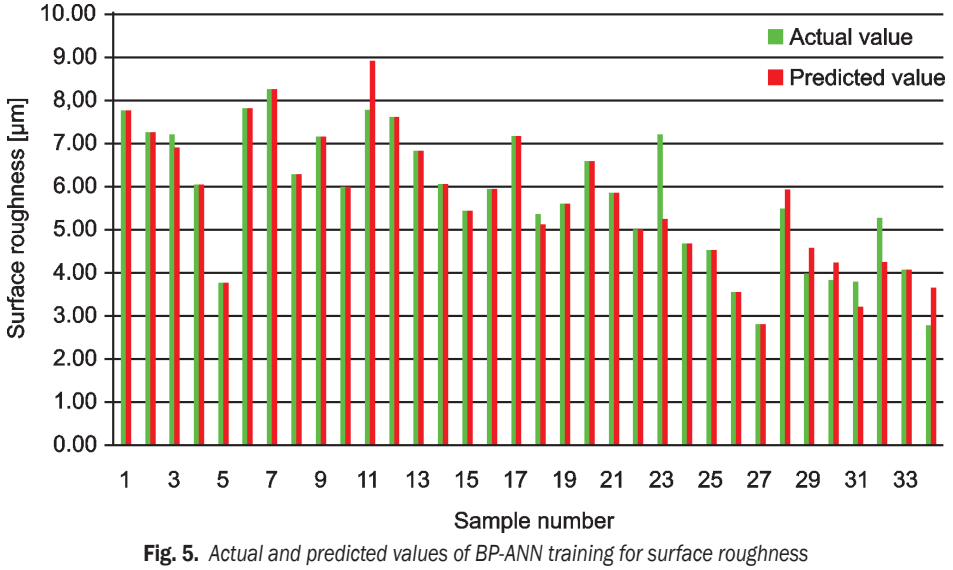

Fig. 5. *Actual and predicted values of BP-ANN training for surface roughness*

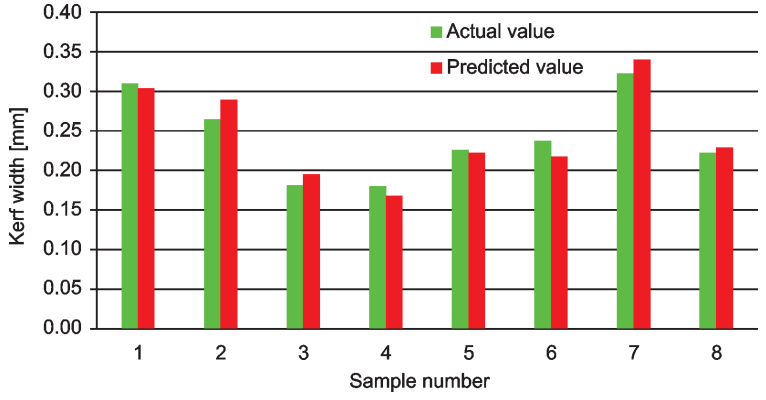

Fig. 6. *Actual and predicted values of BP-ANN testing for kerf width*

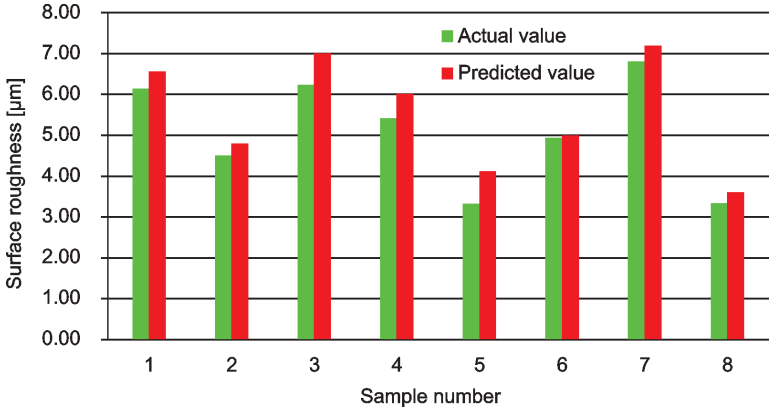

Fig. 7. *Actual and predicted values of BP-ANN testing for surface roughness*

but it can be concluded that the ANN model is adequate for predicting both of these laser cutting processes' performances.

In this work, it was also shown that in the field of experimental research the assist gas type has the most significant effect on the cut quality especially on the kerf width. The ability to predict cut quality even before machining based on the input process parameters such as laser power, cutting speed and assist gas type would give manufacturers the benefits in terms of cost and time savings and the possibility of selecting the appropriate laser cutting process parameters in order to obtained optimal quality characteristics.

In practice when we are cutting rare or even unknown material we need to obtain the input parameters, which will result in sufficient quality. The presented work enables possibility to get those parameters with fewer experiments and without need to analyse all possible mutual influences. In the future work, more detailed discussions should be considered on the effects of different process parameters such as assist gas pressure, focus position, stand-off, type material and material thickness on laser cutting quality characteristics such as heat-affected zone, microstructure and micro-hardness.

5 ACKNOWLEDGEMENT

The authors would like to thank the Ministry of Education, Science and Sport, Republic of Slovenia and the Federal Ministry of Education and Science, Bosnia and Herzegovina for their financial support of this study through the Bilateral Project entitled: "Development of an intelligent system for prediction of CO_2 laser cut quality". Also, thanks to the Department of Laser and Opto-Technologies at the University of Applied Science Jena, Germany where experimental work was performed.

6 REFERENCES

[1] Parandoush, P., Hossain, A. (2014). A review of modeling and simulation of laser beam machining. *International Journal of Machine Tools and Manufacture*, vol. 85, p. 135-145, **DOI:10.1016/j.ijmachtools.2014.05.008**.

[2] Klancnik, S., Brezocnik, M., Balic, J., Karabegovic, I. (2013). Programming of CNC milling machines using particle swarm optimization. *Materials and manufacturing processes*, vol. 28, no. 7, p. 811-815, **DOI:10.1080/10426914.2012.718473**.

[3] Hrelja, M., Klancnik, S., Balic, J., Brezocnik, M. (2014). Modelling of a turning process using the gravitational search algorithm. *International Journal of Simulation Modelling*, vol. 13, no. 1, p. 30-41, **DOI:10.2507/IJSIMM13(1)3.248**.

[4] Ficko, M., Palcic, I. (2013). Designing a layout using the modified triangle method, and genetic algorithms. *International Journal of Simulation Modelling*, vol. 12, no. 4, p. 237-251, **DOI:10.2507/IJSIMM12(4)3.244**.

[5] Syn, C.Z., Mokhtar, M., Feng, C.J., Manurung, Y.H.P. (2011). Approach to prediction of laser cutting quality by employing fuzzy expert system. *Expert Systems with Applications*, vol. 38, no. 6, p. 7558-7568, **DOI:10.1016/j.eswa.2010.12.111**.

[6] El-Labban, H.F., Mahmoud, E.R.I., Al-Wadai, H. (2014). Laser cladding of Ti-6Al-4V alloy with vanadium carbide particles. *Advances in Production Engineering & Management*, vol. 9, no. 4, p. 159-167, **DOI:10.14743/apem2014.4.184**.

[7] Begic, D., Kulenovic, M., Cekic, A., Bliedtner, J. (2009). CW CO2 laser cutting of tungsten alloy using O2 assist gas. *Proceedings of the 20th International DAAAM Symposium*, p. 1345-1346.

[8] Hasçalık, A., Ay, M. (2013). CO2 laser cut quality of Inconel 718 nickel–based superalloy. *Optics & Laser Technology*, vol. 48, p. 554-564, **DOI:10.1016/j.optlastec.2012.11.003**.

[9] Pandey, A.K., Dubey, A.K. (2012). Simultaneous optimization of multiple quality characteristics in laser cutting of titanium alloy sheet. *Optics & Laser Technology*, vol. 44, no. 6, p. 1858-1865, **DOI:10.1016/j.optlastec.2012.01.019**.

[10] Cekic, A., Begic-Hajdarevic, D., Kulenovic, M., Omerspahic, A. (2014). CO_2 laser cutting of alloy steels using N_2 assist gas. *Procedia Engineering*, vol. 69, p. 310-315, **DOI:10.1016/j.proeng.2014.02.237**.

[11] Tsai, M.-J., Li, C.-H., Chen, C.-C. (2008). Optimal laser-cutting parameters for QFN packages by utilizing artificial neural networks and genetic algorithm. *Journal of Materials Processing Technology*, vol. 208, no. 1-3, p. 270-283, **DOI:10.1016/j.jmatprotec.2007.12.138**.

[12] Yilbas, B.S., Karatas, C., Uslan, I., Keles, O., Usta, Y., Yilbas, Z., Ahsan, M. (2008). Wedge cutting of mild steel by CO2 laser and cut-quality assessment in relation to normal cutting. *Optics and Lasers in Engineering*, vol. 46, no. 10, p. 777-784, **DOI:10.1016/j.optlaseng.2008.04.019**.

[13] Yilbas, B.S., Akhtar, S., Keles, O. (2014). Laser cutting of triangular blanks from thick aluminum foam plate: Thermal stress analysis and morphology. *Applied Thermal Engineering*, vol. 62, no. 1, p. 28-36, **DOI:10.1016/j.applthermaleng.2013.09.026**.

[14] Avanish, K.D., Vinod, Y. (2008). Laser beam machining – A review. *International Journal of Machine Tools &* Manufacture, vol. 48, no. 6, p. 609-628, **DOI:10.1016/j.ijmachtools.2007.10.017**.

[15] Begic, D. (2010). *Experimental and Numerical Analysis of Influential Parameters on the Cut Quality in Metal Laser Cutting*. PhD thesis, University of Sarajevo, Sarajevo.

Strojniški vestnik - Journal of Mechanical Engineering 61(2015)12, 721-730
DOI:10.5545/sv-jme.2015.2674
Original Scientific Paper
Received for review: 2015-05-13
Received revised form: 2015-09-29
Accepted for publication: 2015-10-14

Natural Frequency Changes due to Severe Corrosion in Metallic Structures

Gilbert-Rainer Gillich* – Zeno Iosif Praisach – Vasile Iancu – Horia Furdui – Ionica Negru
"Eftimie Murgu" University of Resita, Faculty of Mechanical Engineering, Romania

Degradation of engineering structures due to corrosion affects their safety by reducing the cross-section of structural components and altering the material's mechanical characteristics. These parameter changes are observable in the shift of the natural frequencies. In the study presented in this paper, it was demonstrated that the kinetic energy distribution reflects the mass participation, thus being able to predict frequency changes due to mass loss, while the modal strain energy distribution can be properly used to indicate the location of the damage. As a result, two mathematical relations were developed by the authors, predicting the frequency changes due to the main effects of corrosion: loss of mass and loss of stiffness.

Keywords: corrosion, damage assessment, natural frequency, cantilever beam, mass loss

Highlights

- *The effect of corrosion damage upon the natural frequency of structures is analyzed.*
- *Two mathematical relations for the prediction of frequency changes due to stiffness diminishing a respective loss of mass are proposed.*
- *The frequency increase due to loss of mass is proportional with the square of the mode shape at the damage location.*
- *The frequency drop due to stiffness decrease is proportional with the square of the mode shape curvature at the damage location.*
- *Simulations made using the ANSYS software and experiments confirmed the results achieved by calculus using the contrived relations.*

0 INTRODUCTION

The interaction between engineering structures and the environment usually have corrosion as a consequence, producing important changes in the materials mechanical and physical properties and the structures geometry [1] and [2]. This leads to damage that often result in impairment of the structures functions. The corrosion process always starts from the components surface, but sometimes penetrates deep into the material.

A conventional criterion to classify the corrosion phenomena concerns the appearance of the corroded area [3]. In this regard, two basic forms of corrosion are defined: (a) generalized corrosion, which can be either uniform, when the component surface is affected at the same rate on a large area or non-uniform corrosion, which is characterized by variation of the corrosion rate in different regions of the surface; (b) localized corrosion, which is restricted to compact areas.

Some typical damage geometries and their models are illustrated in Fig. 1. Examining this figure, we can conclude that for uniform corrosion, pitting, erosion and cavitation corrosion, a loss of mass and a cross-section reduction are present. Therefore, these types of damage are best modeled by beams or plates with a stepwise variable thickness [4] and [5]. In the case of stress and fatigue corrosion, the cross-section reduction is very local, and no loss of mass is present. Hence, the damage influence upon the beam rigidity can be modeled as a decrease in the longitudinal elasticity modulus E.

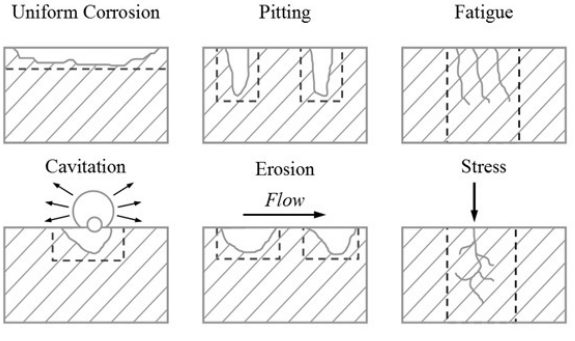

Fig. 1. *Typical corrosion geometries and the equivalent geometrical models*

Herein, only corrosion causing both losses of mass and rigidity is considered. The thickness loss produced to structural elements by corrosion leads to a reduced bearing area and, therefore, decreased structural performance. This results in the life-service limitation, as shown in [6] and [7]. In addition, changes in the structure's modal parameters occur,

*Corr. Author's Address: "Eftimie Murgu" University of Resita, Faculty of Mechanical Engineering, Traian Vuia Square 1-4, Resita, Romania, gr.gillich@uem.ro

mainly in the sense of natural frequency drops; these changes constitute the basic input if dynamic methods are applied to assess the damage. If cracks are present in the structure, the mass changes are insignificant and mainly neglected in most approaches.

In the case of generalized corrosion, it is impossible to neglect the loss of mass while this parameter becomes the most relevant one. Even if corrosion concerns the interest of researchers, because it is a major problem for structures, no reliable model for corroded structures is available.

In prior research, we considered the influence of transverse cracks, which did not produce loss of mass, upon the dynamic behavior of beams, and established a simple and reliable method to assess this type of damage [8]. The most recent investigations focused on the influence of both local and uniform corrosion on the beam dynamical behavior, with regard to the joined effect of stiffness change and loss of mass. This paper presents a behavioral model of corroded beams and the subsequent mathematical relations, as well as a procedure based on this model, used to improve damage detection methods.

1 ANALYTICAL INVESTIGATION

Since the natural frequency changes are the relevant features used for structural damage assessment, the aim of this section is to introduce two mathematical relations developed by the authors, indicating the changes due to stiffness decrease and loss of mass, respectively.

The case of a corroded cantilever beam is used for exemplification. Its geometrical asymmetry assures an unequivocal damage location definition. In its healthy state, the prismatic steel beam analyzed (Fig. 2) has the length L, the width B and the height H. As a consequence, the beam has the cross-section area $A = B{\cdot}H$ and the moment of inertia $I = (B{\cdot}H^3)/12$. The involved mechanical parameters are: the mass density ρ, the longitudinal elasticity modulus E and the Poisson ratio μ. In addition, the earth's gravity g is considered. The single load acting on the cantilever is its own mass.

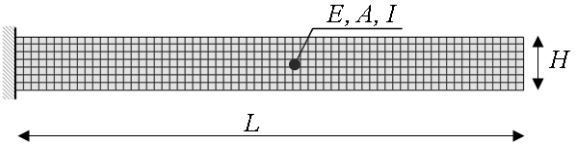

Fig. 2. *Cantilever beam model*

The natural frequencies f_i for the bending vibration modes of a cantilever beam are derived as:

$$f_i = \frac{\alpha_i^2}{2\pi}\sqrt{\frac{EI}{mL^3}}. \quad (1)$$

Here m is the beam mass and α_i are the wave numbers for the beam that resulted as solutions of the characteristic vibration equation.

That is, for the cantilever beam:

$$\cos\alpha\cosh\alpha + 1 = 0. \quad (2)$$

In the case of uniform corrosion, the cross-section is reduced to h on a segment of length ΔL. The geometrical model is presented in Fig. 3a. To separate the effect of the stiffness reduction from that of the mass loss, two individual models are proposed. In the model depicted in Fig. 3b, the loss of mass is considered by reducing the volumetric mass density in the corroded region, while maintaining constant stiffness.

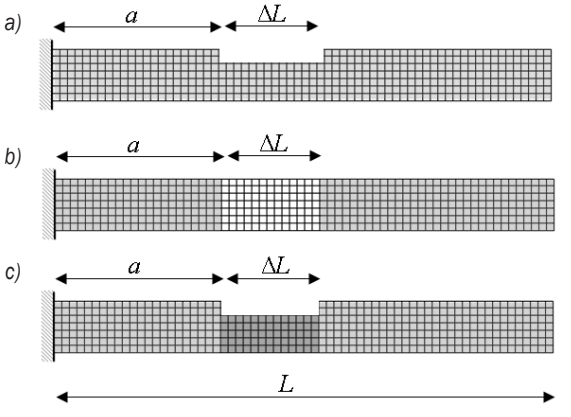

Fig. 3. *Corroded cantilever beam models*

Dissimilarly, to highlight just the effect of stiffness decreases, the model shown in Fig. 3c has an increased volumetric mass density in the corroded region.

The mass density is derived in both cases in such a way to assure the same beam mass.

1.1 Deriving the Loss of Mass Influence

The model presented in Fig. 3b is used to derive the effect of the mass loss on the natural frequencies.

First, we consider the cantilever beam as continuous and having no mass. A mass m_P located at the distance x from the fixed end covers in a quarter-period $T_i/4$ the distance $w_i(x)$. A mass m_E positioned at the free end cover in the same time distance $wi(L)$.

These distances depend on the bending vibration mode shape, defined as:

$$w_i(x) = \cos h\alpha_i x - \cos\alpha_i x - \\ -\frac{\cos\alpha_i L + \cos h\alpha_i L}{\sin\alpha_i L + \sin h\alpha_i L}(\sin h\alpha_i x - \sin\alpha_i x), \quad (3)$$

for the cantilever.

This fact is illustrated in Fig. 4 for the bending vibration mode three. The kinetic energy calculated from the mass m_P, the general case, is:

$$U_{Ki}(x) = \frac{m_P}{2}\left[\frac{w_i(x)}{T_i}\right]^2. \quad (4)$$

For the mass m_E, the kinetic energy results in:

$$U_{Ki}(L) = \frac{m_E}{2}\left[\frac{w_i(L)}{T_i}\right]^2. \quad (5)$$

To attain the same natural frequencies in both cases, the kinetic energies of the two models have to be equal. Eqs. (4) and (5) result in the dependency between two masses for the i^{th} vibration mode, which is:

$$m_{Ei} = m_P\left[\frac{w_i(x)}{w_i(L)}\right]^2 = m_P[\bar{w}_i(x)]^2. \quad (6)$$

With $\bar{w}_i(x)$ we denoted the dimensionless transverse displacement for a point located at the distance x from the fixed end; it takes values between null and the unit.

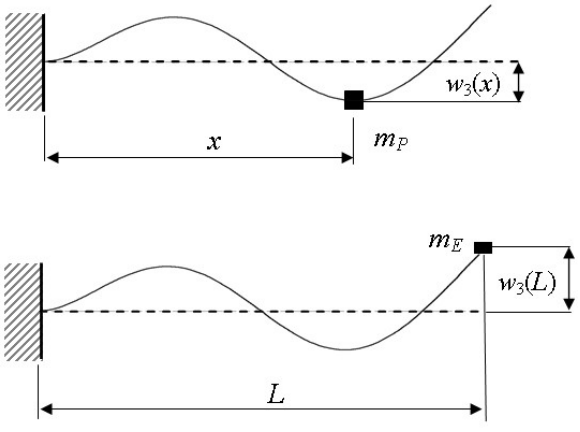

Fig. 4. *Two dynamic equivalent systems, having the mass located at different positions*

In concordance to Eq. (6), for any mass located at a distance x from the fixed end, an equivalent mass conventionally located on the free end can be derived. These masses are in a relation given by the normalized mode shape square $[\bar{w}_i(x)]^2$. From the dynamic point of view, the beam equivalent own mass is achieved by summarizing the equivalent masses of all beam slices. Fig. 5 exemplifies the case of bending vibration Mode 3.

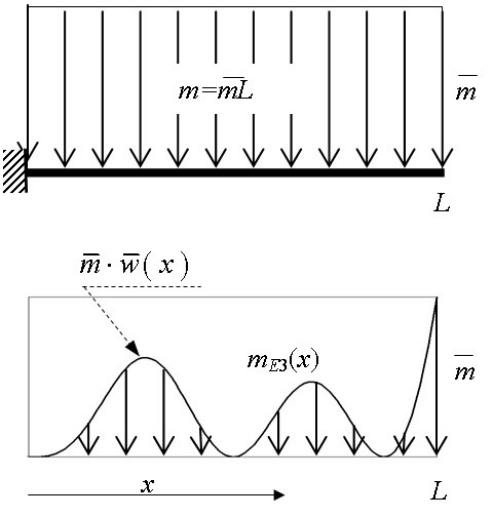

Fig. 5. *Cantilever beam statically load by a distributed inertia and the mass participation in the kinetic energy for Mode three*

In fact, the total equivalent mass m_i^{eq}, corresponding to the i^{th} bending vibration mode, is obtained by multiplying the beam's specific mass $\bar{m}$ with the area under the curve $[\bar{w}_i(x)]^2$. Consequently,

$$m_i^{eq} = \bar{m}L\int_0^L[\bar{w}_i(x)]^2\,dx = 0.25\bar{m}L. \quad (7)$$

The area under the entire curve $[\bar{w}_i(x)]^2$ is 0.25 for all bending vibration modes, because the curves have the same nature.

Hence, the frequency of the undamaged beam can be expressed, with regard to the equivalent mass, as:

$$f_i = \frac{\alpha_i^2}{2\pi}\sqrt{\frac{EI}{\bar{m}L^4}} = \frac{\alpha_i^2}{2\pi}\sqrt{\frac{EI}{4m_i^{eq}L^3}}. \quad (8)$$

The mass contribution to the total kinetic energy can be derived from Eq. (7) for any location along the beam. The participation of each slice regards the distance covered in a quarter of the period T_i, thus being different for the different vibration modes. Fig. 6 depicts the mass participation of 100 slices for the bending vibration mode three.

Let us consider now that the specific beam mass decreases due to uniform corrosion on a specific beam segment of length $\Delta L = b - a$. The consequence is a reduced specific mass $\bar{m}_R$ on that segment.

The equivalent mass contribution of the corroded segment is:

$$m_{Ri}^{eq} = \bar{m}_R L \int_a^b [\,\bar{w}_i(x)\,]^2\, dx = \bar{m}_R L \varsigma_i. \qquad (9)$$

Note that for corrosion extended on the whole beam surface, the mass participation coefficient is $\varsigma_i = 0.25$.

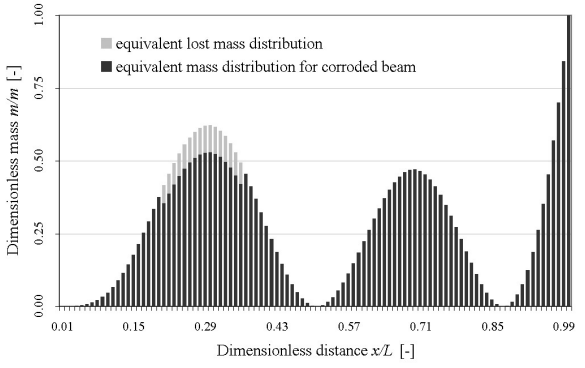

Fig. 6. *The mass participation for 100 slices to the total kinetic energy for vibration Mode 3*

Fig. 6 presents the mass participation for a beam having a corroded segment ($h = 0.9H$), located between $a = 0.2L$ and $b = 0.36L$. On that portion, less mass will contribute to the kinetic energy. The entire mass contribution for the corroded beam is marked with dark bars in Fig. 6.

The total equivalent specific mass, contributing to the kinetic energy, is found by summarizing the equivalent specific masses of the two healthy segments to that found for the corroded segment in Eq. (9). These are:

$$m_{Hi-1}^{eq} = \bar{m} L \int_0^a [\,\bar{w}_i(x)\,]^2\, dx = \bar{m} L \kappa_i, \qquad (10a)$$

$$m_{Hi-3}^{eq} = \bar{m} L \int_b^L [\,\bar{w}_i(x)\,]^2\, dx = \bar{m} L \sigma_i, \qquad (10b)$$

where κ_i and σ_i are the mass participation coefficient for the segments 0 to a respectively b to L.

We presumed the stiffness to be constant along the beam and the mass loss attributed to a decrease in the mass density, as illustrated in Fig. 3b. The natural frequencies for the beam with decreased mass are:

$$f_{Ri} = \frac{\alpha_i^2}{2\pi} \sqrt{\frac{EI}{4\left(m_{Hi-1}^{eq} + m_{Ri}^{eq} + m_{Hi-3}^{eq}\right) L^3}}, \qquad (11)$$

similar to:

$$f_{Ri} = \frac{\alpha_i^2}{2\pi} \sqrt{\frac{EI}{4\left(\kappa_i \bar{m} + \varsigma_i \bar{m}_R + \sigma_i \bar{m}\right) L^4}}. \qquad (12)$$

In regard to Eq. (8) and performing simple mathematical operations, the natural frequencies of the beam with the decreased mass result in:

$$f_{Ri} = f_i \sqrt{\frac{\bar{m}}{4\left(\kappa_i \bar{m} + \varsigma_i \bar{m}_R + \sigma_i \bar{m}\right)}}. \qquad (13)$$

The frequency increase caused by the loss of mass is:

$$\Delta f_{Ri} = f_i \left(\sqrt{\frac{\bar{m}}{4\left(\kappa_i \bar{m} + \varsigma_i \bar{m}_R + \sigma_i \bar{m}\right)}} - 1 \right). \qquad (14)$$

As a consequence, this has the relative frequency shift, attained by dividing the frequency increase to that of the healthy beam in the respective mode becomes:

$$\Delta \tilde{f}_{Ri} = \frac{\Delta f_{Ri}}{f_i} = \sqrt{\frac{\bar{m}}{4\left(\kappa_i \bar{m} + \varsigma_i \bar{m}_R + \sigma_i \bar{m}\right)}} - 1. \qquad (15)$$

The frequency increases for two damage scenarios are illustrated below:

- in the first scenario (Fig. 7) the mass loss is simulated for segments of length $0.1L$ and ten cases are analyzed, the location being successively replaced along the beam;
- in the second scenario (Fig. 8) the mass loss is simulated for segments of length $0.05L$ and twenty cases are analyzed, the location being again successively replaced along the beam.

From the two figures presented below, one can first observe that the frequency shift due to loss of mass depends on the corroded segment's position on the beam. These changes are directly related to the mass participation (or the square of the highest velocity achieved by each slice individually), which is presented in Fig. 6. This is particularly obvious in Fig. 8 and confirmed by the expression of the kinetic energy, containing the sum of all beam slice masses.

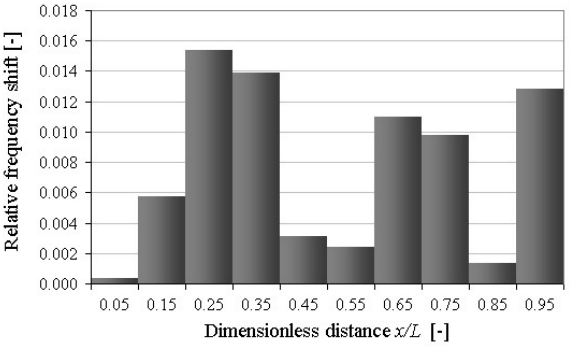

Fig. 7. *The relative frequency shift for Mode 3: mass loss on segments of length 0.1L*

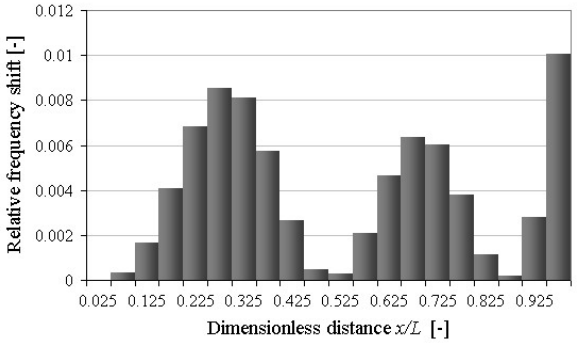

Fig. 8. *The relative frequency shift for Mode 3: mass loss on segments of length 0.05L*

Now, comparing the proportions between the bins in Fig. 7 and that of the homonym pair of bins in Fig. 8 a similarity is found, confirming the fact that the superposition principle is valid for the frequency shifts. This also can be deduced from Eq. (9).

1.2 Deriving the Loss of Stiffness Influence

The analysis made on the corroded beam by neglecting the mass decrease, according to the model presented in Fig. 3c, concerns only the moment of inertia I as a factor influencing the natural frequencies. This case is nominated as corrosion in this sub-section.

In previous research [10], we proved that the energy loss is proportional to the deflection increase. The loss of capacity to store energy, due to damage to the corroded beam, manifests as an apparent energy increase for a healthy beam (the opposite to Castgliano's theorem), because of the deflection under similar load increases in case of damage.

Three specific domains can be observed in Fig. 9: the two healthy segments having the moment of inertia $I=BH^3/12$, and the corroded segment with $I_C=Bh^3/12$.

Because we assume that the corroded segment has a higher mass density, the inertial forces will keep constant along the beam in order to compensate the mass loss. In the corroded region, the neutral axis is deviated to the new mid-cross-section.

While the mass distribution remains constant, the bending moment $M(x)$ is easily derived for the healthy cantilever beam, as it is known that it is proportional with the mode shapes' second derivative. Thus, the dimensionless bending moment is similar to the dimensionless curvature $\bar{M}_i(x) = \bar{w}_i''(x)$. Here, both terms of the relation are made dimensionless by the division to the highest value of the category, achieved at the fixed end: these are $M_i(0)$ and $w_i''(0)$.

In the case of a partial stiffness decrease, as shown in Fig. 9, it is convenient to consider the effective bending moment $M_{eff}(x)$. It is the moment acting on a presumed healthy beam, but producing a similar effect as $M(x)$ on the corroded one. The relation between the two bending moments is:

$$M_{eff}(x) = M(x)\frac{I_{\text{actual}}}{I_{\text{reference}}}. \tag{16}$$

As a consequence, this has a perturbation of the bending moment in the transition zones and an increase of it in the corroded region.

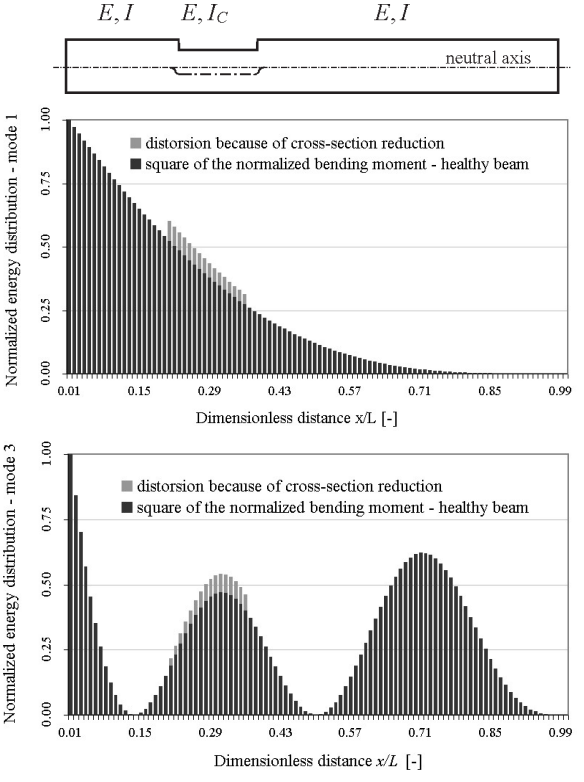

Fig. 9. *Typical regions for a corroded beam and the energy distributions for modes 1 and 3*

Furthermore, in Fig. 9, the apparent energy increase is presented for mode one (similar to the static load) and mode three. The distortion in the transition region can be neglected since the cross-section centers for the healthy and corroded segments are closely located.

The apparent energy increase is actually a decrease, while the beam is able to store less energy for a reduced cross-section. Thus, the energy loss ratio is derived from the corroded and healthy state, as:

$$\eta_i = \frac{\bar{U}_{Si}}{\bar{U}_i} = \frac{\frac{1}{2EI}\int_0^L \left[\bar{M}_{eff-i}(x)\right]^2 dx}{\frac{1}{2EI}\int_0^L \left[\bar{M}_i(x)\right]^2 dx}. \quad (17)$$

Both the actual and the effective moments are dimensionless.

The energy distribution along the beam for the analyzed case is, in the explicit form:

$$\bar{U}_{Si} = \frac{1}{2EI}\int_0^a \left[\bar{M}_i(x)\right]^2 dx + \\ + \frac{1}{2EI_C}\int_a^b \left[\bar{M}_i(x)\right]^2 dx + \frac{1}{2EI}\int_b^L \left[\bar{M}_i(x)\right]^2 dx, \quad (18)$$

where 0 to *a* and *b* to *L* are the healthy segments and *a* to *b* is the corroded one.

In accordance with Eq. (16), and considering the inverse effect of stiffness decrease to the stored energy, we can replace the actual bending moment in Eq. (17) by $M(x) = (I_C / I) M_C(x)$. Moreover, by adding and subtracting the strain energy of the healthy segment *a* to *b* in Eq. (18), one attains:

$$\bar{U}_{Si} = \bar{U}_i + \frac{1}{2EI_C}\int_a^b \frac{I_C^2}{I^2}\left[\bar{M}_i(x)\right]^2 dx - \\ - \frac{1}{2EI}\int_a^b \left[\bar{M}_i(x)\right]^2 dx, \quad (19)$$

or, in a comprehensive form:

$$\bar{U}_{Si} = \bar{U}_i - \left(1 - \frac{I_C}{I}\right)\frac{1}{2EI}\int_a^b \left[\bar{M}_i(x)\right]^2 dx. \quad (20)$$

Now, after substituting U_{Si} in Eq. (17) and reduction of the common factor, the energy loss ratio becomes:

$$\eta_i = \frac{\int_0^L \left[\bar{M}_i(x)\right]^2 dx}{\int_0^L \left[\bar{M}_i(x)\right]^2 dx} - \frac{I - I_C}{I}\frac{\int_a^b \left[\bar{M}_i(x)\right]^2 dx}{\int_0^L \left[\bar{M}_i(x)\right]^2 dx}. \quad (21)$$

Denoting $\tau_i = \int_a^b \left[\bar{M}_i(x)\right]^2 dx$, and knowing that $\int_0^L \left[\bar{M}_i(x)\right]^2 dx = 0.25$ as in the case of lateral deflection, the energy loss ratio is found as:

$$\eta_i = 1 - \frac{4\tau_i (I - I_C)}{I}. \quad (22)$$

From Eqs. (17) and (22), the relation between the natural frequencies for the beam with stiffness decrease and the healthy one results as:

$$\frac{f_{Si}}{f_i} = \sqrt{\frac{U_{Si}}{U_i}} = \sqrt{\eta_i} = \sqrt{1 - \frac{4\tau_i (I - I_C)}{I}}, \quad (23)$$

hence, the frequencies for the damaged beam are:

$$f_{Si} = f_i \frac{\sqrt{I - 4\tau_i (I - I_C)}}{\sqrt{I}}. \quad (24)$$

The frequency shift due to stiffness decrease results from Eq. (24), as:

$$\Delta f_{Si} = f_i - f_{Si} = f_i \left[1 - \frac{\sqrt{I - 4\tau_i (I - I_C)}}{\sqrt{I}}\right], \quad (25)$$

and as consequence the relative frequency shift is:

$$\Delta \tilde{f}_{Si} = \frac{\Delta f_{Si}}{fi} = \frac{\sqrt{I} - \sqrt{I - 4\tau_i (I - I_C)}}{\sqrt{I}}. \quad (26)$$

In the following, the frequency decrease is illustrated for two damage scenarios. First, the stiffness reduction manifests on a segment of length $0.1L$, and ten cases are analyzed. The damage location is successively replaced along the beam (see Fig. 10).

The second scenario considers a stiffness reduction on a segment of length $0.05L$ and twenty cases are analyzed, the location again being successively replaced along the beam. The results are presented in Fig. 11.

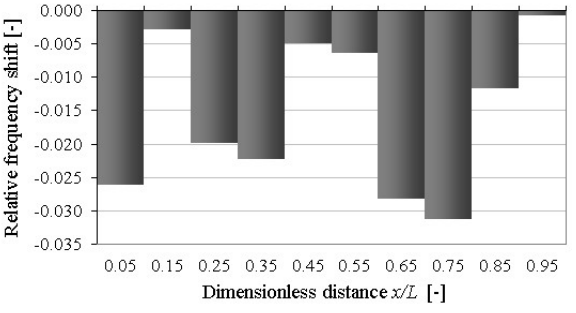

Fig. 10. *The relative frequency shift for mode 3: stiffness loss on segments of length 0.1L*

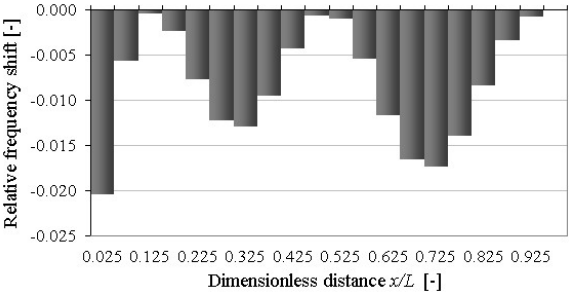

Fig. 11. *The relative frequency shift for mode 3: stiffness loss on segments of length 0.05L*

If the corrosion is extended on the whole beam surface, i.e. τ_i=0.25, by neglecting the loss of mass, one obtains the frequencies for the slimmer beam (with thickness h) as:

$$\hat{f}_{Si} = f_i \frac{\sqrt{I_C}}{\sqrt{I}}. \quad (27)$$

The frequencies of a corroded beam (with both loss of mass and stiffness decrease) derived from Eqs. (16) and (24) depend on the healthy beam's frequency and 3 parameters that characterize the damage geometry: a and b indicating the damage extend and $d = H - h$ as the damage depth. Therefore, it is possible to characterize any corrosion damage by patterns, defined as a sequence of frequency shifts of some bending vibration modes. Comparing these patterns with frequency shifts found from measurements the damage can be located and its severity evaluated **[9]** to **[11]**.

2 NUMERICAL VERIFICATION

In order to prove the validity of the contrived mathematical relations, which express the frequency changes due to mass and stiffness decrease, a finite element analysis was performed. First, the undamaged beam, as a reference, was investigated. Afterward, the corroded cantilever was considered, for three particular cases:

1. the beam with a corroded segment associated with loss of mass and stiffness, Fig. 3a;
2. the beam with constant stiffness having a segment presenting a loss of mass realized by the density alteration, Fig. 3b;
3. the beam having a segment with reduced stiffness, but with compensated loss of mass in order to assure the original mass, Fig. 3c.

The analysis was performed with SolidWorks software. Tetrahedral elements are taken, with the reference dimension of 6 mm. The resulted number of nodes is around 16,000 and the number of elements around 7,800 in all cases, assuring high precision.

The intact steel beam with a rectangular cross section has the following geometry: length L = 1 m, width B = 50 mm and height H = 5 mm. The physical-mechanical parameters are: the mass density ρ = 7850 kg/m^3, the longitudinal elasticity modulus $E = 2.0 \cdot 10^{11}$ N/m^2 and the Poisson ratio μ = 0.3. The Earth gravity acceleration is taken g = 9.806 m/s^2 and the mass of the beam results as being m = 1.9625 kg.

The parameters of the corroded region for three conceived damage scenarios are presented comprehensively in Table 1.

Table 1. *Damage geometrical parameters*

Case	Depth, D [mm]	Left limit, a [mm]	Right limit, b [mm]	Extent, ΔL [mm]
A	0.5	500	600	100
B	1	500	600	100
C	0.5	700	900	200

The first three frequencies for the weak-axis bending vibration modes are found using the Modal analysis module. Table 2 presents the results derived from the contrived relations, for the healthy beam and the three damage scenarios, while the results obtained by simulations are presented in Table 3. The fit between the results obtained analytically and by means of FEA confirm the validity of the relations.

Table 2. *Natural frequencies – analytically*

Mode i	Scenario	f_i [Hz]	f_{Ri} [Hz]	f_{Si} [Hz]	f_{Ci} [Hz]
1	A	4.077	4.0901	4.0589	4.072
	B		4.1034	4.0444	4.0708
	C		4.1668	4.0744	4.1642
2	A	25.550	25.779	24.840	25.069
	B		26.015	24.257	24.722
	C		25.739	25.246	25.435
3	A	71.539	71.652	71.138	71.251
	B		71.766	70.815	71.042
	C		72.070	68.788	69.319

The frequencies of the corroded beam from Table 2 are derived, involving the shifts due to the stiffness decrease and the mass loss, as:

$$f_{Ci} = f_i - \Delta f_{Ri} - \Delta f_{Si} = f_{Ri} + f_{Si} - f_i. \quad (28)$$

Table 3. *Natural frequencies – FEM simulations*

Mode i	Scenario	f_i^{FEM} [Hz]	f_{Ri}^{FEM} [Hz]	f_{Si}^{FEM} [Hz]	f_{Ci}^{FEM} [Hz]
1	A	4.092	4.1047	4.0669	4.08
	B		4.1181	4.0289	4.054
	C		4.1821	4.0885	4.178
2	A	25.639	25.870	24.732	24.973
	B		26.111	23.521	24.012
	C		25.708	25.225	25.314
3	A	71.792	71.902	71.280	71.416
	B		72.019	70.605	70.879
	C		72.335	68.329	68.941

To have an overview on the results, the relative frequency shifts are derived and compared. Eqs. (15) and (26) are again involved for the cases of mass loss

respectively stiffness decrease. If both changes occur, we use

$$\Delta\tilde{f}_{Ci}^{FEM} = \frac{f_{Ci}^{FEM} - f_i^{FEM}}{f_i^{FEM}} 100. \quad (29)$$

Table 4 presents the results achieved from the analytical study and Table 5 those from the FEM analysis.

Table 4. *Relative frequency shifts – analytical*

Mode i	Scenario	$\Delta\tilde{f}_{Ri}$ [%]	$\Delta\tilde{f}_{Si}$ [%]	$\Delta\tilde{f}_{Ci}$ [%]
1	A	0.321	–0.444	–0.122
	B	0.647	–0.799	–0.152
	C	2.202	–0.063	2.138
2	A	0.89	–2.778	–1.882
	B	1.819	–5.060	–3.240
	C	0.266	–1.189	–0.923
3	A	0.157	–0.560	–0.402
	B	0.317	–1.012	–0.694
	C	0.742	–3.845	–3.103

Table 5. *Relative frequency shifts – FEM analysis*

Mode i	Scenario	$\Delta\tilde{f}_{Ri}^{FEM}$ [%]	$\Delta\tilde{f}_{Si}^{FEM}$ [%]	$\Delta\tilde{f}_{Ci}^{FEM}$ [%]
1	A	0.312	–0.613	–0.293
	B	0.637	–1.540	–0.928
	C	2.203	–0.085	2.101
2	A	0.901	–3.534	–2.597
	B	1.843	–8.258	–6.345
	C	0.269	–1.613	–1.349
3	A	0.153	–0.711	–0.523
	B	0.317	–1.652	–1.271
	C	0.756	–4.823	–3.971

For a clear overview, the frequencies of the damaged beam are made dimensionless by dividing their values by the healthy beam's frequencies. The values, indicating a good concordance, are indicated in Fig. 12. A perfect fit is attained for the frequency increase due to mass loss derived by calculus and attained from the FEM. Regarding the case of stiffness decrease, the result varies, but with a value less than 3.5 %, which is achieved for Mode 2 of the beam with the deepest corrosion (the reason for this is the neglecting of the bending moment distortion). The correctness of the mathematical relations presented in Section 2 is confirmed.

The relative frequency shifts should be given a special attention. Their values are analogous for the two scenarios: A and B. The difference consists in their amplitudes, which are in a relation fixed by the damage severity (i.e. corrosion depth d). This shows that by normalizing the relative frequency shifts a sequence of values is achieved constituting a pattern that indicates the corroded region's location. Dissimilar is the case of Scenario C, which leads to a different pattern.

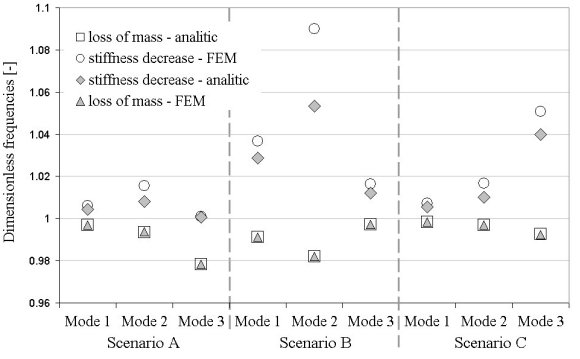

Fig. 12. *Ratios between the frequencies derived analytically and evaluated by FEM analysis*

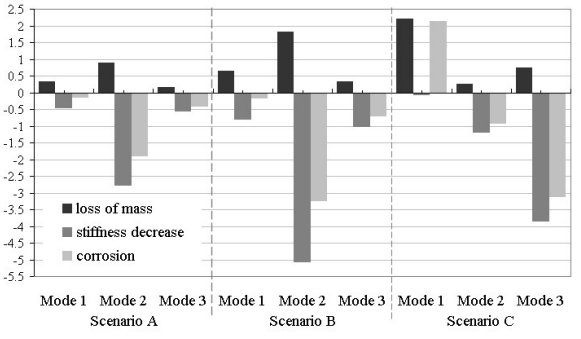

Fig. 13. *The relative frequency shifts*

Analyzing the frequencies of the beam in two damage locations, the results show that the position definitely determines the shift values. If a stiffness decrease affects an area near the contraflexure, less frequency drop is observed. In contrary, if the stiffness affects a region with important hogging, the drop is significant. The mass decrease leads to a frequency increase, which is in direct relation to the square of the mode shape value at the damage location.

3 LABORATORY EXPERIMENTS

The numerical analysis performed to prove the correctness of the theoretical findings was completed by experiments. These were performed on a similar cantilever, the three first natural frequencies for the healthy and corroded beam being aimed. To ensure proper rigidity for the clamped end, this was fixed in a milling machine vise, which is a component of the testing stand presented in Fig. 14.

The acquisition equipment consists of a laptop computer, an NI cDAQ-9172 compact chassis with NI 9234 signal acquisition modules and a unidirectional Kistler 8772 accelerometer, which is fixed close to the beam's free end. High precision in evaluating the natural frequencies is required since a low shift in frequency is expected. For this reason, a virtual instrument was developed in LabVIEW that permits acquiring the acceleration time history and the accurate evaluation of frequencies [12].

Fig. 14. *The experimental stand*

To simulate uniform corrosion, a discontinuity was produced by abrasion, the disruption having the parameter of scenario A in the numerical simulations section.

The measured frequencies f_i^M for the first six bending vibration modes, for the intact beam and the beam with simulated corrosion, are presented in Table 6. Furthermore, the resulted relative frequency shifts are indicated, as well as the values derived by means of FEM analysis for the damage depth d = 0.5 mm respectively d = 1 mm. The results, presented in Table 6 and Fig. 15, are in good correlation, confirming the validity of the proposed analytical relation for the prediction of frequency shifts.

Table 6. *Measured natural frequencies and the relative shifts for the measured and calculated frequencies*

Mode i	f_i^M [Hz]	f_{Ci}^M [Hz]	$\Delta\tilde{f}_{Ci}^M$ [%]	$\Delta\tilde{f}_{Ci}^{FEM}$ [%]	
				$d = 0.5$	$d = 1$
1	4.0199	3.9663	–0.347	–0.293	–0.928
2	25.192	23.535	–5.881	–2.597	–6.345
3	70.539	69.367	–0.928	–0.523	–1.271
4	138.23	132.54	–3.402	–1.506	–3.374
5	228.50	222.36	–1.961	–0.941	–2.125
6	341.34	332.46	–1.875	–0.990	–2.235

The frequency shifts derived by the FEA frame those from measurements, meaning the right location has been found. The damage depth, created between 0.5 and 1 mm, is correctly estimated as 0.8 mm. In contrast, by comparing the first three frequency shifts achieved by measurements with those in Table 5 for the case C, dissimilarity can be observed. This proves the univocal definition of locations by the relative frequency shifts.

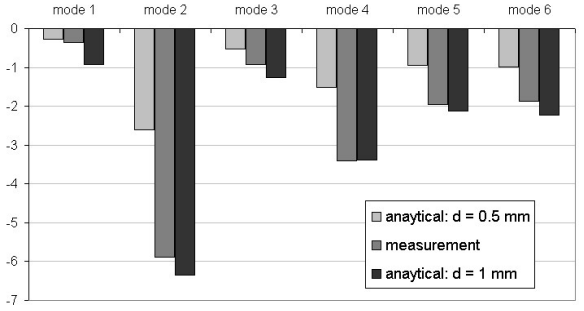

Fig. 15. *Calculated relative frequency shifts for the FEM analysis and the measurement results*

4 CONCLUSION

Two mathematical relations for the prediction of frequency changes due to stiffness diminishing a respective loss of mass are proposed. The first relation associates the effect of a local mass loss on the natural frequencies with the mode shape value corresponding to that location. The correlation between the frequency changes due to the stiffness decrease and the beam curvature was also found, and the second resulting relation was derived. It has to be mentioned that, due to the fact that in this second relation the effect of the bending moment distortion in the transition regions is neglected, deviations from the real frequency shifts can occur. This is a topic which is in our concern for feature research.

In order to reach the natural frequency values if both effects occur, the two relations have to be superimposed. Finite element analysis and experiments confirmed the correctness of these relations. Since the relations have as input the damage geometry and the healthy beams mode shape and curvature, these are easily adaptable for any boundary conditions.

The relative frequency shifts derived from these relations provide a simple way to describe the behavior of corroded beams. From these relations, a database containing numerous damage scenarios was realized. The corroded region in the three cases was successfully found with the involvement of this database.

5 ACKNOWLEDGEMENT

The work has been funded by the Ministry of European Funds through the Financial Agreement POSDRU/159/1.5/S/132395.

6 NOMENCLATURE

A	cross-section area of the healthy beam [m^2]
a	distance from the fixed end to the left corrosion limit [m]
B	beam width [m]
b	distance from the fixed end to the right corrosion limit [m]
d	corrosion depth [m]
E	Young's modulus [N/m^2]
f_i	i^{th} natural frequency [Hz]
$\tilde{f}_i$	relative frequency shift due to damage for the i^{th} vibration mode [%]
H	beam height [m]
h	height of the segment subjected to uniform corrosion [m]
I	moment of inertia [m^4]
L	beam length [m]
ΔL	length of segment subjected to uniform corrosion [m]
$M(x)$	bending moment at distance x from the fixed end [N·m]
$M_{eff}(x)$	effective bending moment x from the fixed end [N·m]
m_P	mass of a slice located at the distance x from the fixed [kg]
m_E	mass of a slice located at the free end [kg]
m_i^{eq}	equivalent mass of a beam segment for the i^{th} vibration mode [kg]
$\bar{m}$	specific mass [kg/m]
$\bar{m}_R$	reduced specific mass [kg/m]
T	period [s]
$w_i(x)$	beam deflection at distance x from the fixed end for the i^{th} vibration mode [m]
$w_i''(x)$	beam curvature at distance x from the fixed end for the i^{th} vibration mode [m^{-1}]
U_k	kinetic energy [kg·m^2/s^2]
α_i	wave number of the i^{th} vibration mode [-]
η	energy loss ratio [-]
ς_i, κ_i and σ_i	mass participation coefficients of beam segments for the i^{th} vibration mode [-]
ρ	volumetric mass density [kg/m^3]
μ	Poisson ratio [-]

subscripts indicates

i	the bending vibration mode number
H	the healthy beam/segment parameters
R	the beam/segment parameters with reduced specific mass
S	the beam/segment parameters with reduced specific stiffness
C	the parameters of the corroded beam/segment

superscript indicates

FEM	the results obtained by means of the FEM
M	the results obtained by measurements

7 REFERENCES

[1] ISO 8044 (1986). Corrosion of Metals and Alloys - Terms and Definitions. International Organization for Standardization, Geneva.

[2] Rahbar Ranji, A., Zakeri, A.H. (2010). Mechanical properties and corrosion resistance of normal strength and high strength steels in chloride solution. *Journal of Naval Architecture and Marine Engineering*, vol. 7, no. 2, p. 93-100, **DOI:10.3329/jname.v7i2.5309**.

[3] Landolfo, R., Cascini, L., Portioli, P. (2010). modeling of metal structure corrosion damage: A state of the art report, *Sustainability*, vol. 2, no. 7, p. 2163-2175, **DOI:10.3390/su2072163**.

[4] Bazant, Z.P. (1979). Physical model for steel corrosion in concrete sea structures-Theory. *Journal of the Structural Division*, vol. 105, no. 6, p. 1137-1153.

[5] Warkus, J., Raupach, M. (2010). Modelling of reinforcement corrosion – geometrical effects on macrocell corrosion. *Materials and Corrosion*, vol. 61, no. 6, p. 494-504, **DOI:10.1002/maco.200905437**.

[6] Apostolopoulos, C.A., Michalopoulos, D. (2007). Impact of corrosion on mass loss, fatigue and hardness of BSt500 Steel. *Journal of Materials Engineering and Performance*, vol. 16, no. 1, p. 63-67, **DOI:10.1007/s11665-006-9009-8**.

[7] Zhang, X.-Y., Li, S.-X., Liang, R., Akid, R. (2013). Effect of corrosion pits on fatigue life and crack initiation. *13th International Conference on Fracture*, Beijing.

[8] Gillich, G.R., Praisach, Z.I., Iavornic, C.M. (2012). Reliable method to detect and assess damages in beams based on frequency changes. *Proceedings of the ASME International Design Engineering Technical Conference*, Chicago, p. 129-137, **DOI:10.1115/DETC2012-70094**.

[9] Thambiratnam, D., Shih, H.W., Chan, T., Tan, Z.X. (2015). Vibration based structural health monitoring to evaluate the damage in flexural members. *International Journal of Mechanics*, vol. 9, p. 181-188.

[10] Gillich, G.R., Praisach, Z.I. (2013). Damage-patterns-based method to locate discontinuities in beams. *SPIE Proceedings*, art. no. 869532, **DOI:10.1117/12.2009122**.

[11] Song, Y.-Z., Bowen, C.R., Kim, H.A., Nassehi, A., Padget, J., Gathercole, N., Dent, A. (2014). Non-invasive damage detection in beams using marker extraction and wavelets. *Mechanical Systems and Signal Processing*, vol. 49, no. 1-2, p. 13–23, **DOI:10.1016/j.ymssp.2013.12.011**.

[12] Onchis-Moaca, D., Gillich, G.R., Frunza, R. (2012). Gradually improving the readability of the time-frequency spectra for natural frequency identification in cantilever beams. *Proceedings of the 20th European Signal Processing Conference*, p. 809-813.

Strojniški vestnik - Journal of Mechanical Engineering 61(2015)12, 731-740

DOI:10.5545/sv-jme.2015.2796 Original Scientific Paper
Received for review: 2015-06-26
Received revised form: 2015-09-11
Accepted for publication: 2015-10-06

Analysis of Flow Field and Pumping Performance for a Valveless Piezoelectric Pump with a Hemisphere-segment Group

Caiqi Hu[1] – Jing Ji[1,*] – Xiaoqi Hu[2] – Jude Liu[3] – Shengduo Li[1]

[1]Qingdao Agricultural University, College of Mechanical and Electrical Engineering, China
[2]Lishui University, College of Engineering and Design, China
[3]The Pennsylvania State University, Department of Agricultural and Biological Engineering, USA

The pumping and mixing performance of a valveless piezoelectric pump were proposed and studied. A hemisphere-segment group that was fixed in the pump played the role of a valve. Based on the theoretical analysis of the pumping performance, the changes of the fluid velocity field, pressure difference, the coefficient of resistance and flow rate were simulated with FLUENT. Simulation results revealed the relationships among the pressure field, flow rates, row and column numbers, and row and column intervals of the hemisphere-segment group. The simulation results indicated that increasing row and column numbers, increasing row intervals, and decreasing column intervals could all increase the flow resistance difference in pump flow field and thus increased the flow rate. It was also found that the pumping effect was significantly improved by increasing row number than increasing column number; the increasing of row and column intervals could increase the size and strength of the vortex, and then improve the mixing and stirring performance of this pump. Finally, simulation results were tested and verified through pump flow-rate experiments.

Keywords: hemisphere-segment group, array, valveless piezoelectric pump, simulation analysis, flow rate, mesh independence

Highlights

- *The changing pattern of the pumping and mixing performance for a new valveless pump was proposed.*
- *The pumping performance was analysed based on the theory of hydrodynamics.*
- *The changes of the fluid velocity field, pressure differences, the coefficient of resistance and flow rates vs. HSG dimensions and arrangement were simulated.*
- *Simulation results were tested and verified through pump flow rate experiments.*

0 INTRODUCTION

Traditional pumps use mechanical motion to create fluid flow. Unlike with the traditional pump, the principle of the valveless piezoelectric pump is to convert electrical energy into mechanical energy via the vibration of a piezoelectric vibrator. The resulting movement and force from this piezoelectric vibrator will then directly act on the fluid medium to create fluid flow [1]. Such a pump has no moving parts when controlling fluid in unidirectional flow. Thus, it has no mechanical wearing problems and lubrication requirements, as needed in traditional pumps [2]. Therefore, the valveless piezoelectric pump has advantages in low manufacturing costs [3], easy miniaturization, low energy consumption, and long service life, etc. [4]. It also has wide potential application in medical, health, mechanical, and electrical systems that require the miniaturization of mechanical components [5]. Moreover, the valveless piezoelectric pump has unique advantages, especially in the integrated piezoelectric mixing and conveying field for microflow liquid [6] and [7].

There are several types of no-moving-part valves with different structures for valveless piezoelectric pumps. Most previous studies were focused on valveless diffuser/nozzle-based fluid pumps [8]. For this type of pump, a pair of mutually inverted diffuser/nozzle tubes was externally fitted to both sides of the pump chamber to form a one-way flow [9]. These two external tubes occupied some space and hindered the pump's further integration and miniaturization. A piezoelectric mixing pump was put forward by Rife et al. [10]. To form a homogeneous mixture, the piezoelectric vibrator in that pump drove the blocks in the mixing pool and created vortexes. This device could only mix and stir fluids, and was not able to convey them. Another piezoelectric mixing pump was reported by Sheen et al. [11], which integrated the functions of fluid mixing and pumping; but the block structures of this pump used for mixing were complex. A valveless piezoelectric pump with unsymmetrical slope elements were presented by Xia et al. [12], which could realize the integration of mixing and conveying functions. The unsymmetrical slope elements in the pump chamber bottom played the role of a no-moving-part valve. Meanwhile when

*Corr. Author's Address: Qingdao Agricultural University, College of Mechanical and Electrical Engineering, Qingdao, China, hucaiqi@163.com

the fluid flowed through unsymmetrical slopes, the vortexes and turbulence were formed, and the fluid was fully mixed and stirred. However, the unsymmetrical slopes increased the complexity of the pump structure and thus could cause difficulties in manufacturing. The valveless piezoelectric pump with hemisphere-segment (VPPHS) contains a hemisphere segment as a no-moving-part valve. The hemisphere segment (HS) is a 1/4 sphere, which has features of a simple structure and good manufacturability. When the piezoelectric vibrator (PV) vibrates upward and downward in the pump chamber, the fluid is pumped because of flow resistance difference (FRD) between the round face and the spherical surface of HS [13]. For the valveless piezoelectric pump with a hemisphere-segment group (VPPHSG), however, some HSs are arranged in a certain way to function as a no-moving-part valve. When the fluid flows through the hemisphere-segment group (HSG), the fluid and those hemisphere segments, interact with each other and generate turbulences and vortexes, which form a very complex flow field and create pressure differences. As a result, the turbulence/vortex make the fluid mixed or blended, and the pressure difference generates fluid flow. Thus, it is imperative to understand the interactions between HSG parameters and fluid flow and quantify their impacts on pump flow field and flow rate.

In this paper a VPPHSG, which can mix, stir and convey fluid, was proposed and studied. The objectives of this research were (1) to theoretically analyse the pumping process and flow rate; (2) to develop models based on different row and column numbers and intervals of HSs and use these models to calculate and simulate the velocity and pressure of the flow field, HSG resistance coefficient (RC), and the pump flow rate; (3) Then the effect of varying HSG parameters on pumping performance, as well as the influence of those parameters on mixing and stirring effect was analysed; (4) to verify the pump flow rate simulation results with experimental results.

1 VALVE-LESS PUMP STRUCTURE

The structure of VPPHSG is shown in Fig. 1. All HSs are arranged in a rectangle. All row intervals of HSs are equal, as are all column intervals. All HSs are oriented in the same way. The flat semi-circular surface of HS is perpendicular to the center connection line of Tubes B and D. The spherical surface of HSs faces to the side of Tubes A, B and C. The diameters of Tubes A, B, C, and D are equal. The flat semi-circular surfaces of HSs face the side of tube D. Some dimensions of the pump used for simulation are listed in Table 1. When PV vibrates up and down in the pump chamber, the fluid is pumped in one way because of the FRD formed between the semi-circular plane and spherical surface of the HS [12]. Multiple HSs that are regularly arranged can undoubtedly amplify the FRD of a single HS and form a one-way flow from the side of Tubes A, B and C to the side of Tube D in the pump chamber. Thus, the pumping performance could be better with HSG as a no-moving-part valve than with a single HS as a no-moving-part valve. Three different liquids in different proportions can be fed into the pump chamber through three tubes (A, B and C). When different liquids flow through the complex flow field with HSG, these three liquids can be fully mixed and stirred because of turbulences and vortexes generated in the flow field. Mixed liquids are conveyed out through Tube D. The functions of mixing, stirring, and conveying are realized.

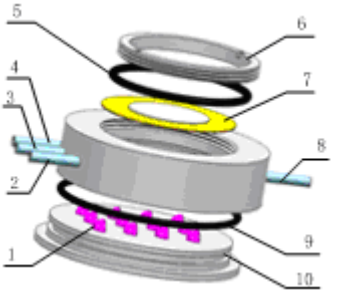

Fig. 1. *Valveless pump structure; 1. HSG; 2. Tube A; 3. Tube B; 4. Tube C; 5. upper seal ring; 6. screw pump cover; 7. PV; 8. Tube D; 9. lower seal ring; 10. pump seat*

To conduct theoretical analysis, when fluids are fed into the pumping chamber from Tubes A, B, and C and pumped out from tube D, this flow direction is defined as forward flow (FF); conversely, if the fluid flows into the pumping chamber from Tube D and comes out from tubes A, B, and C, it is defined as reverse flow (RF). Tubes A, B, and C are defined as inlet tubes, and tube D is defined as an outlet tube.

2 THEORETICAL ANALYSIS OF PUMPING

The pumping performance of a piezoelectric pump depends on the characteristics of the no-moving-part valve [14]. For the VPPHSG, the total pressure loss when fluid flows through HSG with m rows and n column HSs is related to the flow resistance coefficient (FRC), flow velocity, and fluid density. Their relationships can be expressed as follows:

$$\sum \Delta p_F = \sum \left(C_{DF} \right) \cdot \rho v_F^2 / 2, \tag{1}$$

$$\sum \Delta p_R = \sum \left(C_{DR} \right) \cdot \rho v_R^2 / 2, \tag{2}$$

where $\Sigma\Delta p_F$ and $\Sigma\Delta p_R$ are the total pressure loss of FF, RF, respectively, ΣC_{DF} and ΣC_{DR} are the total resistance coefficient of flow around HSG in FF, RF, respectively, v_F and v_R are the average velocity of FF, and RF, respectively, ρ is fluid density.

The total pressure loss is the sum of all HSs pressure loss, and the total resistance coefficient is the sum of all RCs. It can be expressed as follows:

$$\sum \Delta p_F = \sum_{i=1}^{m} \left(\sum_{j=1}^{n} \Delta p_{ijF} \right), \tag{3}$$

$$\sum \Delta p_R = \sum_{i=1}^{m} \left(\sum_{j=1}^{n} \Delta p_{ijR} \right), \tag{4}$$

$$\sum C_{DF} = \sum_{i=1}^{m} \left(\sum_{j=1}^{n} C_{DijF} \right), \tag{5}$$

$$\sum C_{DR} = \sum_{i=1}^{m} \left(\sum_{j=1}^{n} D_{DijR} \right). \tag{6}$$

The flow quantity Q of unit time for a pump can be expressed as follows **[15]** and **[16]**:

$$Q = \Delta V f \frac{\sum C_{DR} - \sum C_{DF}}{2 + \sum C_{DR} + \sum C_{DF}}, \tag{7}$$

where ΔV is the maximum variation of pump chamber volume in a vibration cycle of PV, and f is the vibration frequency of PV.

According to Eq. (7), when $\Sigma C_{DR} - \Sigma C_{DF} \neq 0$, $Q \neq 0$. This indicates that the one-way flow of fluid can be formed in the pump chamber. Because the HS has an asymmetric structure, and the resistances when fluid flowing around the spherical surfaces and the semi-circular plane of HS are unequal, the forward and reverse flow resistances of HSG are also unequal. This flow resistance difference makes the pump convey fluid in a single direction.

3 FLOW FIELD ANALYSIS

According to Eq. (7), when ΔV and f are constant, ΣC_{DR} and ΣC_{DF} will have a great influence on the pump flow rate. The row and column numbers, row and column intervals of HSG have a direct influence on the pump flow rate and the resistance difference. The flow field is complex because of the resistance that HSG creates on the fluid in the pump chamber. The analytical solution for the variations of velocity and pressure could not be obtained. The simulation with FLUENT is an effective method to study the velocity and pressure in a flow field. In the following, the flow fields with different row and column numbers and different intervals of HSG are simulated and analysed to obtain the influence of those factors on the pumping performance.

3.1 Numerical Mesh Analysis

In this research, the models of a valveless pump with HSG arranged in a rectangle were established in FLUENT. The structural and geometric parameters are shown in Table 1. The boundary conditions used for simulating the upward and downward cycle vibration of the piezoelectric vibrator was the sine function. The pressure at inlets and outlet was set at standard atmospheric pressure. The working medium of the pump was water, which was treated as a viscous incompressible Newtonian fluid.

This study included seven different models for simulating pump flow fields when the fluid flows through the hemisphere-segment group. To increase calculation efficiency, the unstructured mesh was found more suitable for this simulation. Therefore, it was used to construct the pump's internal flow field. Meanwhile, to receive more accurate flow field data, a smaller mesh and more elements per area or higher mesh density were used within the HSG and in those areas near the inlet and outlet of the pump.

Mesh independence was analysed based on different numbers of mesh elements. As an example, pump internal flow-field analysis results for a 3 by 4 HSG with fixed row interval (S = 12 mm) and column interval (H = 12 mm) are given in Fig. 2. This example included more than one different mesh densities or a different number of mesh elements.

The results of the simulation using the above models in Fig. 2 are given in Fig. 3. When increasing the number of mesh elements or mesh density, the

Table 1. *Pump structure parameters for simulation*

Name	Radius of HS	Diameter of tube A	Diameter of PV	Height of pump chamber	Pump chamber	
					Outer diameter	Inner diameter
Size [mm]	4	4	50	6	80	68

simulated flow rate decreases rapidly, and then tends to steady when the number of mesh elements is greater than 60,000. When increasing mesh elements from 613,865 to 1,344,625, the simulated flow rate was relatively constant. This is the evidence of mesh independence.

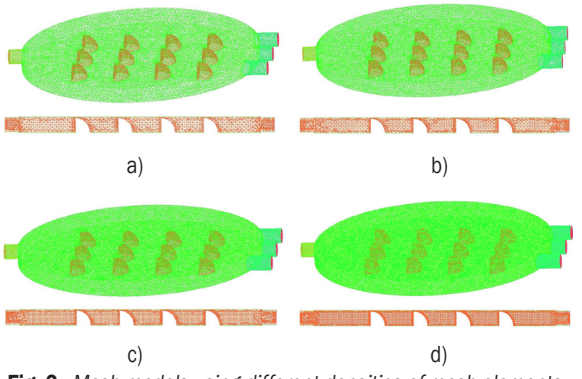

Fig. 2. *Mesh models using different densities of mesh elements; global mesh size is a) 0.4, b) 0.5, c) 0.4 and d) 0.3 and there are a) 613,865, b) 334,724, c) 613,865 and d) 1,344,625 mesh elements in the pump flow field*

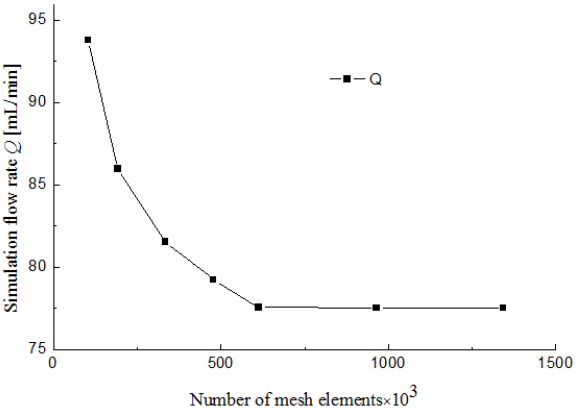

Fig. 3. *Curves of simulation flow rate with different number of mesh elements*

3.2 Turbulence Model Comparison

When the fluid flows through the HSG, turbulence including momentum diffusion and convection, an instantaneous and rapid variation of pressure and flow velocity will be formed due to interactions between fluid and all semi-hemispheres. Analytical solutions to this complex interaction become impossible. A numerical analysis tool, FLUENT was popularly applied to solve these problems. Acceptable simulation results can be achieved using this software. Two turbulence models, standard k–ε and *RNG* k–ε built in FLUENT, were used to compare pump flow simulation effectiveness.

Flow field simulation was conducted using HSGs of 3×1, 3×2, 3×3, and 3×4 for both standard k-ε and RNG k-ε models. Row and column intervals were kept constant at S=H=12 mm in this simulation. Comparisons of simulation results and experimental data are listed in Table 2. Results indicated that the standard k–ε and the *RNG* k–ε models had similar trends; but the *RNG* k–ε model had less error compared to the experimental results. Thus, the *RNG* k–ε turbulence model was used in the rest of this study. The variation of velocity, pressure, resistance coefficient and simulation flow rate were obtained from simultaneous solutions of continuity equation of numerical analysis, N–S equations, and an RNG k–ε turbulence model in FLUENT.

Table 2 *Comparison of measured flow rates and simulated using the standard k–ε and the RNG k–ε turbulence models*

RN or CN		Measured flow rate* [mL/min]	Standard k–ε model [mL/min]	RNG k–ε model [mL/min]
RN=3	CN=1	39.4(0.642#)	85.41	70.25
	CN=2	47.9(0.733#)	92.36	78.33
	CN=3	51.1(0.827#)	98.45	80.02
	CN=4	52.5(0.743#)	104.68	81.55

Notes: row number (RN); column number (CN);
* Mean value of ten replications; # Standard deviation

3.3 Flow Field and Flow Rate Analysis with Different Row, Column Number of HSG

3.3.1 Analysis of Velocity Field

Seven models for simulating pump flow fields were established and analysed. These seven models included pumps with 1×3, 2×3, 3×3, 4×3, 3×1, 3×2, and 3×4 HSGs. The velocity vector contours of the pump flow fields with HSGs 2×3, 3×2, 4×3, and 3×4 were selected as shown in Fig. 2. It can be seen that HSGs have different row and column numbers, with constant row and column intervals (S=H=12 mm).

The velocity fields of forward and reverse flow are shown in Fig. 4. The forward flows in Figs. 4a, c, e, g demonstrate that the fluid flows are blocked by the spherical surfaces of HSs, and the flow field are disturbed and formed a turbulent flow that increases the flow resistance. The flow velocity near the one-quarter spherical region reduces. Meanwhile, part of the water flows through the gaps between HSs and forms some small flow streams and vortexes, which cause the flow velocity to reduce in those gaps, while most of the surrounding fluid flows through those

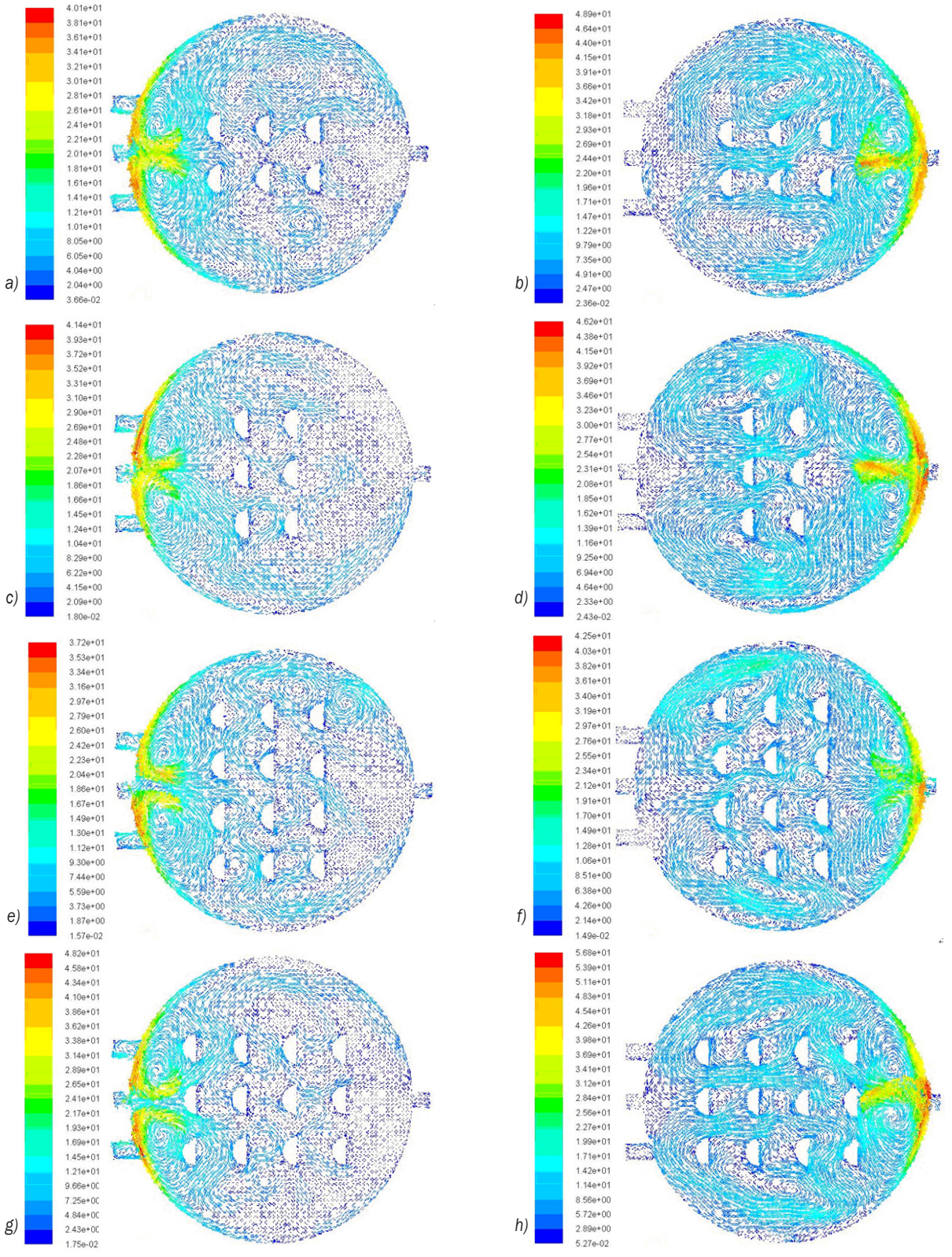

Fig. 4. *Variation of velocity vectors along with the variations of row and column number in HSGs; a) HSG 2×3 in forward flow, b) HSG 2×3 in reverse flow; c) HSG 3×2 in forward flow, d) HSG 3×2 in reverse flow; e) HSG 4×3 in forward flow, f) HSG 4×3in reverse flow, g) HSG 3×4 in forward flow, h) HSG 3×4 in reverse flow*

hemisphere-segments and the flow speed increases gradually. The reverse flows in Figs. 4b, d, f, h demonstrate that fluid flow can be stopped by the flat semi-circular surfaces of HSs; and the water level surges that creates flow resistance sharply increase and the flow velocity rapidly drops. At the same time, part of the lagged fluid is pushed into the gaps and formed stronger streams and larger vortexes. These vortexes circulate within the HSG and produce increased flow resistance. Increasing flow resistance results in further consumption of the fluid kinetic energy, which greatly reduces fluid velocity. In summary, in the reverse flow the HSG consumes more fluid kinetic energy than in forward flow. It indicates that the reverse-flow resistance is dramatically bigger than forward flow resistance, which further explains the essential reason that HSG can play the role of a no-moving-part valve.

3.3.2 Pressure and Resistance Coefficient Analysis

When the fluid flows around the HSG, the boundary layer will split into many vortexes and produce velocity fluctuations that result in the changes of flow resistance and pressure in front and back of the HSG.

In order to obtain the changes of flow resistance and pressure in front and back of the HSG, as shown in Fig. 5, planes a-a, b-b, which are respectively 10 mm from the spherical surface of the left column hemisphere-segments and the flat semi-circular surface of the right column hemisphere-segments in HSG, are taken as reference planes. The intersection points between the center line of each HS row and the reference planes are respectively defined as $P_i, P_i'(i=1,...,m)$, where m is the number of rows. Those points at the spherical surface side are expressed as P_i, while the points at the other side are written as P_i'. The average pressures on reference planes a-a and b-b are defined as $\overline{P}$ and $\overline{P'}$ respectively, and they are successively extracted from the corresponding flow field in Fig. 2. Hence, the pressure differences of the forward and reverse flowing around HSG are $\Delta p = \overline{P} - \overline{P'}$, $\Delta p' = \overline{P'} - \overline{P}$, respectively. The corresponding forward and reverse resistance coefficients can be calculated using Eqs. (1) and (2). The calculated results are shown in Table 3.

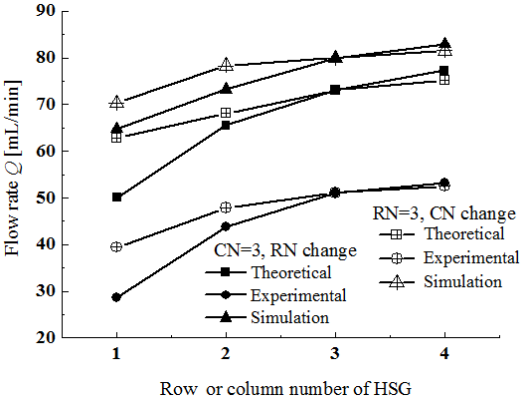

Fig. 5. *Pressure points distribution of specified plane related to HSG*

The results in Table 3 indicate that the pressure differences and resistance coefficients of forward and reverse flow around HSG increase along with the increasing of row number and column number. Moreover, the increase of pressure difference and resistance coefficient in the reverse flow is significantly greater than in forward flow.

3.3.3 Simulation Analysis of Pump Flow Rate

Based on the above simulation, the outlet flow rate was calculated. Fig. 6 shows the variation curves of the simulated flow rate when varying the flow resistance difference and row and column numbers of HSG. Through comparison and analysis, it can be found that the flow rate increases along with the increase of flow resistance difference, row and column numbers.

Table 3. *Comparison of resistance coefficients for HSG with different array*

Row number change	Flow direction	$PD_{\Delta p}$/(*pa*)	RC	FRD	Column number change	Flow direction	$PD_{\Delta p}$/(*pa*)	RC	FRD
1×3	forward	121960	3.072	0.8442	3×1	forward	207912	3.5952	1.2239
	reverse	254387	3.9163			reverse	224383	4.8191	
2×3	forward	175525	3.506	1.259	3×2	forward	235749	3.8934	1.4291
	reverse	311647	4.765			reverse	263553	5.3225	
3×3	forward	249761	4.172	1.6388	3×3	forward	267934	4.172	1.6378
	reverse	413443	5.8108			reverse	305365	5.8098	
4×3	forward	316005	4.643	1.9103	3×4	forward	326085	4.827	1.906
	reverse	512817	6.556			reverse	368279	6.733	

Remarks: pressure difference (PD); flow resistance difference (FRD); resistance coefficient (RC)

3.4 Influence Analysis of Row and Column Interval on Flow Field and Flow Rate

The hemisphere-segment array group of 3×4 is used as an example, and the fixed row interval S set at 8 mm, and column intervals H at 8 mm, 10 mm, 12 mm, and 14 mm respectively; fixed column interval H=10 mm, and row interval S=6 mm, 8 mm, 10 mm, 12 mm respectively. Thus, there were seven hemisphere-segment groups with different intervals. Seven models of pump flow field with different HSGs were established and simulated. The simulated data are shown in Table 4.

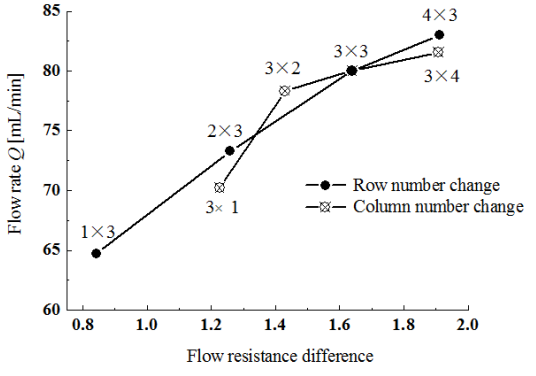

Fig. 6. *Variation curves of simulation flow rate along with the variations of flow resistance, row and column number in HSG*

From Table 4, it can be determined that the pressure differences, resistance coefficients, and simulation flow rates decrease specifically with the increasing of row interval; while increasing column interval the pressure differences, resistance coefficients and simulation flow rates increase. Through analysis, it can be known that the transverse interference and collision of fluid in the gaps of HSG will be weakened by increasing the row interval, and the flow in those gaps increase. Then the blocked fluid is evacuated. So, the fluid resistance is reduced, and the pressure loss and resistance coefficients is reduced. The increasing of column interval will weaken the covering flow effect of HSs in a longitudinal arrangement, and the other HSs behind the first column gradually leave the wake flow influence region of the first column hemisphere-segments, so the pressure difference and resistance coefficient gradually increase. The flow rate increases along with the increasing of flow resistance difference.

When the fluid flows through the region of HSG, turbulences and vortexes are generated that can helpfully mix the fluid with different components. The internal of dramatic turbulences and vortexes can be considered as a chaotic region. Because of multiple HSs arranged in transverse and longitudinal, the turbulences and vortexes generated by the fluid flowing through one or one row HSs have not yet spread out and then immediately are pushed into the influence region of next or next row HSs. In this way, multiple forms of chaos are generated. So, even if the "blind region" will be reduced or even disappear. Such turbulences and vortexes with overlays of layer upon layer can help fluids with different concentration,

Table 4. *Variation comparison of pressure difference, resistance coefficient and pump flow rate along with row, column interval variations*

Interval [mm]		Flow direction	$PD_{\Delta p}$/(*pa*)	FRC	FRD	Simulation flow rate [mL/min]
H = 8	S = 8	forward	238992	4.927	1.834	82.731
		reverse	289521	6.761		
	S = 10	forward	221196	4.862	1.7645	82.26
		reverse	270910	6.6265		
	S = 12	forward	206504	4.6333	1.6132	81.019
		reverse	242708	6.2465		
	S = 14	forward	200971	4.512	1.417	80.01
		reverse	239143	5.929		
S =10	H = 6	forward	72821	4.935	1.673	80.25
		reverse	154381	6.608		
	H = 8	forward	221196	4.862	1.7645	82.26
		reverse	270910	6.6265		
	H = 10	forward	260452	4.846	1.819	82.48
		reverse	378207	6.665		
	H = 12	forward	306045	4.9135	1.859	82.55
		reverse	482780	6.7725		

Remarks: pressure difference (PD); flow resistance difference (FRD); flow resistance coefficient (FRC)

density and viscosity to mix in a highly uniform manner.

4 EXPERIMENTAL VERIFICATION

4.1 Devices and Methods for Pump Flow Rate Test

The test of the pump flow rate was carried out at zero pressure difference between inlet and outlet. The pump flow rate test principle diagram is shown in Fig. 7. The water level in the reservoir (a measuring cup) was kept at the same height as the water level in three inlet tubes and one outlet tube. The signal generator and power amplifier provide the driving voltage and frequency to drive the prototype pump. The weight of the liquid flowing out of the pump chamber in a fixed time interval was measured with an electronic balance, which had a resolution of 0.01 g. The flow rate was repeatedly measured, and the average value was then calculated. Pure water was used as the pump fluid. The driving voltage and frequency were 160 V and 6 Hz, respectively. Pump flow rates were successively measured under different hemisphere-segment array groups with the following combinations of row and column numbers (row by column): 1×3, 2×3, 3×3, 4×3, 3×1, 3×2, 3×3, 3×4. Tests were also conducted for seven hemisphere-segment array groups 3×4 with different rows and column intervals (for fixed column interval H=8, row interval S=8, 10, 12, 14; fixed row interval S=10, column interval H=6, 8, 10, 12).

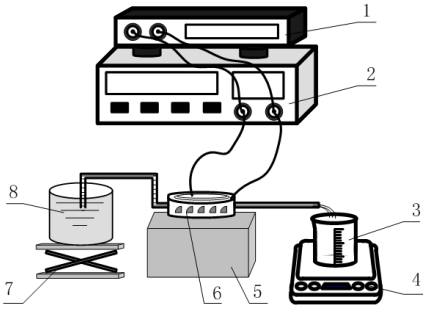

Fig. 7. *Pump flow rate test principle diagram*
1. power amplifier; 2. signal generator; 3. graduated glass; 4. electronic balance; 5. cushion block; 6. prototype pump 7. height-adjustable table; 8. reservoir

4.2 Comparisons of Pump Flow Rates

The theoretical pumping flow rate was calculated according to Eq. (7). The diameter of the piezoelectric vibrator is 50 mm. When the frequency f is 6 Hz the amplitude of the vibrator measured by CCD micro displacement sensor is 1.512 mm. The forward and reverse resistance coefficients are taken from Tables 3 and 4. By calculating and analysing the theoretical flow rates, experimental flow rates, and simulation flow rates are shown in Figs. 8 and 9. All experiments were conducted under the same conditions and repeated 10 times. The mean values of flow rate and standard deviations are shown in Tables 5 and 6.

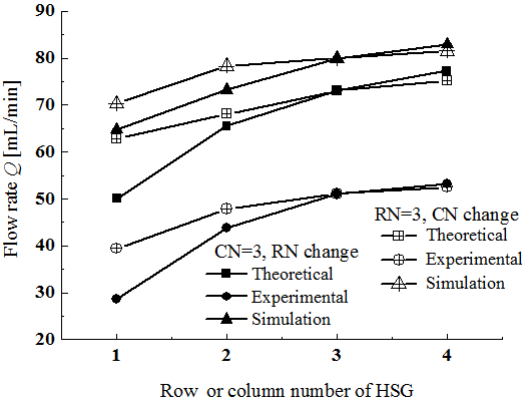

Fig. 8. *Curves of pump flow rate with different CN, RN of HSGs; column number (CN), row number (RN)*

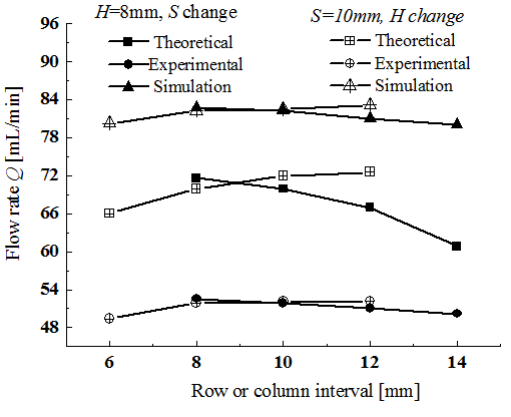

Fig. 9. *Curves of pump flow rate with different S, H of HSGs; column interval (H), row interval (S)*

Fig. 8 shows the curves of pump flow rates with different row and column numbers of HSGs. These curves indicate that theoretical, experimental and simulated flow rates all increase along with the increase of row or column number, and they have the same trend. The average deviations of simulation, theoretical flow rates relative to the experimental flow rates with different row number are 42.0 % and 34.3 %, respectively. The average deviations of simulation, theoretical relative to experimental flow rates with different column number are respectively 39.0 % and 31.8 %.

Table 5. *Mean value and standard deviation of ten repeated experimental results in Fig. 8*

RN or CN		Mean value of flow rate [mL/min]	Standard deviation
CN=3	RN=1	28.6	0.8310
	RN=2	43.9	0.7222
	RN=3	51.1	0.8267
	RN=4	53.2	0.7481
RN=3	CN=1	39.4	0.6422
	CN=2	47.9	0.7325
	CN=3	51.1	0.8267
	CN=4	52.5	0.7428

Notes: row number (RN), column number (CN)

Table 6. *Mean value and standard deviation of ten repeated experimental results in Fig. 9*

Interval [mm]		Mean value of flow rate [mL/min]	Standard deviation
H=8	S=8	52.6	0.6962
	S=10	51.9	0.7214
	S=12	51.08	0.7229
	S=14	50.2	0.7871
S=10	H=6	49.4	0.8690
	H=8	51.9	0.8143
	H=10	52.1	0.8022
	H=12	52.2	0.6465

Fig. 9 shows pump flow rate variation curves with different row and column intervals. It can be seen that the simulation, theoretical, and experimental flow rates all decrease along with the increase of row interval, and all increase along with the increase of column interval; the pump flow rates change slowly in the whole variation range of row and column interval. The average deviations of simulation, theoretical flow rates relative to experimental flow rates with different row interval are 37 % and 23.4 %, respectively. The average deviations of simulation, theoretical flow rates relative to experimental flow rates with different column interval are, respectively, 37.2 % and 27 %.

Comprehensively analysing Table 3 and Fig. 8, as well as Table 4 and Fig. 9, it can be shown that the simulation, theoretical, and experimental flow rates have the same variation trends. Moreover, all of the flow rates increase along with the increasing of flow resistance difference. When the change of flow resistance difference is small, the change of corresponding pump flow rate is al small. The simulation results had the same trend with measured ones. This could provide a guideline for pump designers and researchers. It is also valuable for other researchers in attempting improve their work in the future. Some researchers in reference **[5]** indicated that the relative error between theoretical and experimental results could be as high as 90 %; but the same trend could be used to verify the concept of the design. For the deviations of simulation and theoretical flow rates relative to experimental flow rates in this research, the reasons can be concluded as the following:

(1) Theoretical flow rate expressions and simulation flow rate are derived and analysed according to the simplified model. Moreover, it is ignored that a large amount of heat energy is consumed due to shock waves, turbulence, and fluctuations in the actual transient flow field, so the mechanical energy is no longer conserved. This causes the theoretical and simulation flow rates bigger than the experimental flow rate.

(2) In experiments, boundary layers of the flow field separate and split into many vortexes after the fluid flowing around the hemisphere-segment group, which causes fluid energy loss, so the experimental flow rate is smaller than theoretical and simulation flow rates.

(3) In addition, the errors caused by the vortex circuitously flowing, colon, bubbles, pump sealing, experiment environment and other factors randomly occur, and cannot be quantified by theory or experiments, which directly affect the theoretical analysis and experimental results.

5 CONCLUSIONS

Through theoretical research, simulation analysis, and experimental verification, we have studied in depth the flow field and pumping performance of a valveless piezoelectric pump with HSG. The conclusions are as follows:

(1) The influence of the HSG's different row and column number on pumping performance is simulated and analysed. Moreover, the variation laws of velocity, pressure difference, and resistance coefficient along with the variations of row and column number are obtained. The increasing of row and column number directly increases flow resistance difference of HSG. The pump flow rate increases with the increasing of flow resistance difference. At the same time, it is found that the pump flow rate is bigger by increasing the row number than by increasing the column number, and the pumping performance is better improved by increasing the row number than by increasing the column number.

(2) The influence of the HSG's different row and column intervals on pumping performance is simulated and analysed. Moreover, the variation

laws of velocity, pressure difference, flow rate and resistance coefficient along with the variations of row and column intervals are obtained. It is found that the influence of interval change on flow resistance difference and pump flow rate is not significant, but the interval changes have a large influence on the size and strength of vortexes in flow field. The flow field will generate more and stronger vortexes by increasing the row and column intervals of HSG and the fluid can be well blended. Thus, the function of mixing fluid for a valveless piezoelectric pump with HSG can be well realized.

(3) The pumping performance experiments were carried out with different row and column numbers, and different row and column intervals of HSGs. The variation trend of simulation, theoretical and experimental flow rates was the same, and the reason for the deviations was explained. Finally, simulation results were verified through pump flow rate experiments.

6 ACKNOWLEDGMENTS

This project was supported by National Natural Science Foundation of China (No.51375227, 51475221), Zhejiang Provincial Natural Science Foundation of China (No. LY13E050015), and Application Type University Construction Project of Qingdao Agricultural University.

7 REFERENCES

[1] Izzo, I., Accoto, D., Menciassi, A., Schmitt, L., Dario, P. (2007). Modelling and experimental validation of a piezoelectric micropump with novel no-moving-part valves. *Sensors and Actuators A: Physical*, vol. 133, no. 1, p. 128-140, **DOI:10.1016/j.sna.2006.01.049**.

[2] Zhang, J.H., Li, Y.L., Xia, Q.X. (2007). Analysis of the pump volume flow rate and tube property of the piezoelectric valve-less pump with Y-shape tubes. *Chinese Journal of Mechanical Engineering*, vol. 43, no. 11, p. 136-141, **DOI:10.3901/JME.2007.11.136**. (in Chinese)

[3] Zhang, J.H., Lu, J.ZH., Xia, Q.X., Kou, J., Ren, G. (2008). Working principle and characteristics of valve-less piezoelectric pump with Y-shape tubes for transporting cells and macromolecule. Chinese Journal of Mechanical Engineering, vol. 44, no. 9, p. 92-99, **DOI:10.3901/JME.2008.09.092.** (in Chinese)

[4] Morris, C.J., Forster, F.K. (2003). Low-order modelling of resonance for fixed-valve micropumps based on first principles. *Journal of Microelectromechanical Systems*, vol. 12, no. 3, p. 325-334, **DOI:10.1109/JMEMS.2003.809965**.

[5] Huang, Y., Zhang, J.H., Hu, X.Q., Xia, Q.X., Huang, W.Q., Zhao, C.S. (2010). Dynamics analysis and experiment on the fishtailing type of valveless piezoelectric pump with rectangular vibrator. *Science China Technological Sciences*, vol. 53, no. 12, p. 3241-3247, **DOI:10.1007/s11431-010-4176-0**.

[6] Huang, J., Zhang, J.H., Xun, X.C., Wang, S.Y. (2013). Theory and experimental verification on valveless piezoelectric pump with multistage Y-shape treelike bifurcate tubes. *Chinese Journal of Mechanical Engineering*, vol. 26, no. 3, p. 462-468, **DOI:10.3901/CJME.2013.03.462**.

[7] Huang, J., Zhang, J.H., Wang, S.Y., Liu, W.D. (2014). Analysis of the flow rate characteristics of valveless piezoelectric pump with fractal-like Y-shape branching tubers. *Chinese Journal of Mechanical Engineering*, vol. 27, no. 3, p. 628-634, **DOI:10.3901/CJME.2014.03.628**.

[8] Stemme, E., Stemme, G. (1993). A valve-less diffuser/nozzle-based fluid pump. *Sensors and Actuators A: Physical*, vol. 39, no. 12, p. 159-167, **DOI:10.1016/0924-4247(93)80213-Z**.

[9] Nguyen, N-T., Huang, X. (2000). Numerical simulation of pulse-width-modulated micropumps with diffuser/nozzle elements. *Technical Proceedings of the International Conference on Modeling and Simulation of Microsystems*, p. 636-639.

[10] Rife, J.C., Bell, M.I. Horwitz, J.S., Kabler, M.N., Auyeung, R.C.Y., Kim, W.J. (2000). Miniature valveless ultrasonic pumps and mixers. *Sensors and Actuators A: Physical*, no. 86, no. 1-2, p. 135-140, **DOI:10.1016/S0924-4247(00)00433-7**.

[11] Sheen, H.J., Hsu, C.J., Wu, T.H., Chu, H.C., Chang, C.C., Lei, U. (2008). Experimental study of flow characteristics and mixing performance in a PZT self-pumping micromixer. *Sensors and Actuators A: Physical*, no. 139, no. 1-2, p. 237-244, **DOI:10.1016/j.sna.2007.02.031**.

[12] Xia, Q.X., Zhang, J.H., Lei H, Cheng W. (2009). Theoretical analysis and experimental verification on flow field of piezoelectric pump with unsymmetrical slopes element. *Chinese Journal of Mechanical Engineering*, vol. 22, no. 5, p. 735-744, **DOI:10.3901/CJME.2009.05.735**. (in Chinese)

[13] Ji, J., Zhang, J.H., Xia, Q.X., Wang, S.Y., Huang, J., Zhao, C.S. (2014). Theoretical analysis and experimental verification on valve-less piezoelectric pump with hemisphere-segment bluff-body. *Chinese Journal of Mechanical Engineering*. vol. 27, no. 3, p. 595-605, **DOI:10.3901/CJME.2014.03.595**.

[14] Singhal, V., Garimella, S.V., Murthy, J.Y. (2004). Low Reynolds number flow through nozzle-diffuser elements in valveless micropumps. *Sensors and Actuators A: Physical*, vol. 113, no. 2, p. 226-235, **DOI:10.3901/CJME.2014.03.595**.

[15] Zhang, J.H., Wang, S.Y., Yang, D.P. (1999). A study on a valveless, piezoelectric diffuser/nozzle-based fluid pump: analysis of vibration and the changed amount of the chamber volume. *Piezoelectric & Acoustooptics,* vol. 21, no. 6, pp. 459-460 (in Chinese).

[16] Zhang, J.H., Wang, S.Y. (2001). Study of piezoelectric valveless diffuser/nozzle-based fluid pump: one-way flow principle and the pump flow. *Piezoelectric & Acoustooptics*, vol. 23, no. 1, p. 23-25. (in Chinese)

Strojniški vestnik - Journal of Mechanical Engineering 61(2015)11, 741-750

DOI:10.5545/sv-jme.2015.2610 Original Scientific Paper
Received for review: 2015-04-16
Received revised form: 2015-07-17
Accepted for publication: 2015-09-02

Artificial Neural Networks to Estimate the Thermal Properties of an Experimental Micro-Alloyed Steel and Their Application to the Welding Thermal Analysis

Edgar López-Martínez[1,*] – Héctor Javier Vergara-Hernández[2] – Sergio Serna[3] – Bernardo Campillo[1,4]

[1] National Autonomous University of Mexico, Faculty of Chemistry, Mexico
[2] Morelia Institute of Technology, Metallurgy Science Postgraduate Programme, Mexico
[3] State Autonomous University of Morelos, Research Center in Engineering and Applied Sciences, Mexico
[4] National Autonomous University of Mexico, Institute of Physical Sciences, Mexico

The effect of welding thermal cycles on the microstructure and micro-hardness of the heat-affected zone (HAZ) of an experimental micro-alloyed steel was studied. Due to the experimental difficulties involved in acquiring the thermal cycles, these were determined by applying the solutions of Rosenthal's equations for thick and thin plates. However, to perform this thermal analysis, it requires knowledge of the thermal properties of the micro-alloyed steel; therefore, the implementation of two artificial neural networks (ANNs) was proposed as tool to estimate the thermal conductivity and the heat capacity as a function of the chemical composition and temperature. The ANNs were trained with information obtained from the literature review and then tested with steels that were not used for the training step, but with thermal properties known. A good approximation between the actual and the estimated properties was observed.

It was determined that the microstructural characteristics of the welding zone are a function of the thermal cycles, although there is no great difference in micro-hardness. Martensite was not observed in the welding zone; therefore, the welds of this steel, under these welding conditions, could not be susceptible to hydrogen induced cracking (HIC).

Keywords: heat capacity, thermal conductivity, micro-alloyed steel, heat-affected zone, artificial neural network

Highlights

- *The design of two artificial neural networks was proposed to determine the thermal properties as a function of the chemical composition and temperature of metallic materials.*
- *The thermal conductivity and heat capacity of metallic materials can be estimated as a function of temperature.*
- *The high temperatures reached in the coarse-grained heat-affected zone induced grain growth, which together with the high cooling rate (69 K/s), favoured the formation of bainite.*
- *There is no great difference in micro-hardness in the welding zone.*

0 INTRODUCTION

In manufacturing processes such as solidification, metal forming, welding and powder metallurgy, heat transfer phenomena are involved. For a suitable design and/or analysis of one of these processes, it is necessary to know the thermal properties of the materials. For example, in the heat treatment process designs, it is necessary to know the thermal conductivity and the heat capacity, since the thermal cycles that develop during the process will produce a microstructural change, which will affect the mechanical properties and mechanical behaviour.

Micro-alloyed steels or high-strength low-alloy steels are a special type of structural steels that obtain their outstanding final mechanical properties by thermomechanical treatments and accelerated cooling. However, to achieve a final shape or final component, such as in the field installation of pipelines, these steels are subjected to several welding thermal cycles, and then they can suffer several microstructural changes in the welding zone. Due to the experienced thermal cycles, the base material microstructure can be partially or completely modified to produce a fusion zone (FZ) or weld metal (WM), and a heat-affected zone (HAZ), which leads the welding zone to present different mechanical properties, toughness, and susceptibility to hydrogen-induced cracking (HIC) [1] to [3]. Moreover, mathematical modelling has become a powerful tool to analyse the effect of thermal cycles on the microstructure, mechanical properties, and mechanical behaviour of welded products [4], where it is necessary to know or estimate the thermal properties such as the thermal conductivity and the heat capacity. Usually, the thermal conductivity is determined at steady state by using the guarded-comparative-longitudinal heat-flow technique in heating and the heat capacity is determined at a high heating rate by using differential scanning calorimetry.

Artificial neural networks (ANNs) have been used to solve many problems, in the social and economic sciences as well as health sciences. In

*Corr. Author's Address: National Autonomous University of Mexico, Av. Universidad 3000, Mexico City 04510, Mexico, edgar0902@comunidad.unam.mx

metallurgy, ANNs have been used to model the transition temperature from ductile to brittle in steel [5]; the determination of static recrystallization of hot-deformed steels [6]; the determination of residual stress [7]; the correlation of processing parameters and properties [8]; the microstructural determinations [9]; predicting the behaviour of corrosion-fatigue [10]; modelling toughness of micro-alloyed steels [11]; predict migration energies of vacancies [12]; the prediction of the grain boundary energy [13], and the prediction of steel surface roughness [14]. In the welding process, ANNs have been used to predict the welding-induced angular distortion [15]; the occurrence in solidification cracking [16]; to calculate output parameters of friction-stir welding [17]; to predict the hardness of HAZ for in-service welded pipelines [18].

An ANN is a structure composed of nodes or neurons interconnected and arranged in layers to which weight factors are assigned . Each node in each layer is connected to other nodes in other layers by applying the sum of the weights in a transfer function. The basic architecture of an ANN is composed of three types of layers: input layer, hidden layer and output layer, although an ANN can have more than one hidden layer.

To build an ANN, a database is first required, which is divided into two parts: one for the training step and the other for the testing step. The training step consists of feeding the ANN with information from both the independent and dependent variables, i.e. the input neuron and output neuron signals. Each input is weighted and transformed by a transfer function. With the implementation of a learning rule, the weights of the input neurons are adjusted and the process is repeated until a minimum error is obtained between output neurons and the actual values, so it is said that the ANN has been trained. In the testing step, the ANN is fed with input neurons, but not with output neurons. If the results obtained with the ANN are similar to those actual values, it is said that the ANN has been successfully tested.

Because artificial neural networks have been able to estimate the thermal properties of different systems [19] to [21], it was proposed to use them to estimate the thermal conductivity and the heat capacity of an experimental micro-alloyed steel as a function of temperature, and apply them to the thermal analysis of the HAZ. It was decided to design two ANNs, one to estimate the thermal conductivity and the other to estimate the heat capacity. The input neurons in both ANNs were the chemical composition and temperature, and the output neurons were the thermal conductivity and the heat capacity.

1 METHODOLOGY

1.1 Database

The estimation of thermal conductivity is a function of temperature and phases, and these in turn are a function of temperature and chemical composition, which means that a composition of functions exists:

$$k = k(T, \phi), \tag{1}$$

$$\phi = \phi(T, \mu), \tag{2}$$

where k is the thermal conductivity, T is the temperature, ϕ are the phases and μ is the chemical composition. From this, we can see that the thermal conductivity is a function of the temperature and chemical composition:

$$k = k(T, \mu). \tag{3}$$

We can deduce that when the thermal conductivity is determined as a function of the temperature and chemical composition, implicitly the contributions of each phase to the property are considered. The same analysis can be made for the heat capacity.

Table 1. *Minimum and maximum values of chemical composition, the temperature and the thermal conductivity values*

Variable	Minimum	Maximum
%Fe	16.2	100
%C	0.00	1.70
%Mn	0.00	6.00
%Ni	0.00	63.0
%Mo	0.00	4.80
%V	0.00	3.00
%Cr	0.00	30.4
%Cu	0.00	0.64
%Al	0.00	4.50
%Nb	0.00	3.00
%Si	0.00	3.50
%W	0.00	18.5
%Ti	0.00	1.40
%Co	0.00	46.6
Temperature [K]	273	1473
Thermal conductivity [W/(m K)]	10.9	80.2

In research, these properties are used for thermal analysis in unstable state during heating and cooling; however, the relative amount of phases during heating to a given temperature, may differ in the relative amount of phases during cooling at the

same temperature [22], i.e., the thermal properties would be different. It can be concluded that the thermal properties are also a function of the heating and cooling rate, but because there are no studies or data regarding this function, it might be assumed that this function has no influence in the system. Therefore, one search was conducted in the literature to build two databases for metallic materials: one for the thermal conductivity, and the other for the heat capacity, both as a function of the chemical composition and temperature. A careful examination was conducted in order to attain sufficient information to ensure that the chemical composition of the micro-alloyed steel under study was within the limits of the compositions of the collected metallic materials. The collected information for the thermal conductivity and the heat capacity database was conducted by using 395 metallic materials for the former and 176 metallic materials for the latter. Tables 1 and 2 represent the summary for the thermal conductivity and the heat capacity, respectively. In Fig. 1, the behaviour of these two properties for certain selected metallic materials (in this case, steels) are presented. Regarding the thermal conductivity, a greater effect of the chemical composition is observed at low temperatures, being larger for steels with higher contents of alloying elements. Moreover, in relation to the heat capacity, the alloying elements can decrease this property at temperatures between 900 K and 1100 K. This temperature range corresponds to the transformation zone to form austenite; therefore, increasing the heat capacity may be referred to the latent heat of transformation [23].

Table 2. *Minimum and maximum values of chemical composition, the temperature and the heat capacity values*

Variable	Minimum	Maximum
%Fe	21.0	100
%C	0.00	1.70
%Mn	0.00	13.0
%Ni	0.00	60.0
%Mo	0.00	3.60
%Cr	0.00	29.0
%Cu	0.00	0.64
%Al	0.00	4.50
%Nb	0.00	0.90
%Si	0.00	2.00
%W	0.00	18.5
%Ti	0.00	0.60
Temperature [K]	293	1273
Heat capacity [W/(m K)]	402	960

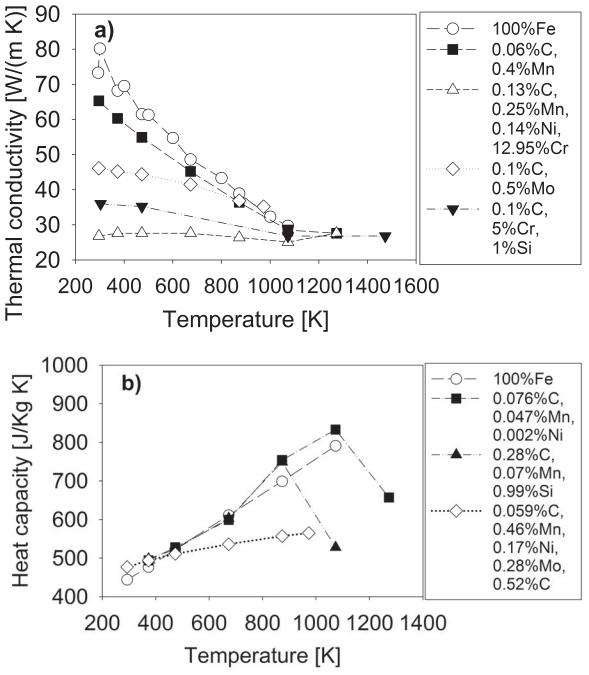

Fig. 1. *Thermal properties as a function of temperature for some steels; a) thermal conductivity, b) heat capacity*

1.2 Design of the ANNs

The ANNs were developed as generalizations of mathematical models of biological neuron systems. The basic unit of an ANN is an elementary processor called a neuron or node, which has the ability to count a weighted sum of its inputs (Eq. (4)), and then apply a transfer function to obtain a signal which is transmitted to another neuron:

$$\left(net\right)_j = \sum_{i=1}^{n} w_{ij} x_i + b, \tag{4}$$

where $(net)_j$ is the weighted sum of the j^{th} neuron for all the n input neurons, w_{ij} is the weight between the neurons of the previous layer and the neurons of the computing layer, b is the bias and x_i is the signal from the i-input neuron.

A transfer function is a function that processes the weighted sum and gives the output signal of the jth neuron. In this work, the sigmoid function was used as a transfer function:

$$f\left(net\right)_j = \frac{1}{1+e^{-\left(net\right)_j}}. \tag{5}$$

Through a learning algorithm, the ANNs parameters are adjusted to minimize the mean square error function (E) (Eq. (6)) between the actual outputs and estimate outputs:

$$E = \frac{1}{2}\sum\left(actual\_ouput - estimated\_output\right)^2. \quad (6)$$

Once the error is computed, the weights are updated one-by-one through a back-propagation with a momentum-learning algorithm by Eq. (7):

$$\Delta w_{ij}(i) = -\gamma \frac{\partial E}{\partial w_{ij}} + \alpha \Delta w_{ij}(i-1), \quad (7)$$

where $\Delta w_{ij}(i)$ and $\Delta w_{ij}(i–1)$ are the new and old changes in the weight of the i connection, and γ and α are known as the learning rate and the momentum respectively. In this equation, the function of the momentum is to accelerate the learning rate [14].

In this paper, the design of two ANNs of the multilayer perceptron with a back propagation and momentum learning rule and sigmoid transfer function was proposed. This approach has given good results in predictions based in ANN [9] and [24]. The first ANN was designed to estimate the thermal conductivity, and the second to estimate the heat capacity. In the first, a total of 15 input neurons were used (14 for the chemical composition and 1 for temperature); in the second ANN, a total of 13 input neurons were used (12 for chemical composition and 1 for temperature). All these neurons, both input and output were normalized by using Eq. (8):

$$x_N = \frac{x - x_{\min}}{x_{\max} - x_{\min}}, \quad (8)$$

where x_N is the normalized value of the x neuron, whose maximum and minimum values are $x_{\max}$ and $x_{\min}$ respectively.

Each of the neurons of the input layer corresponds to an input variable (chemical composition and temperature), and each neuron of the output layer corresponds to each output variable (heat capacity or thermal conductivity). Both ANNs were trained with a single hidden layer and different numbers of neurons in this layer. Fig. 2 shows the general architecture of the ANNs.

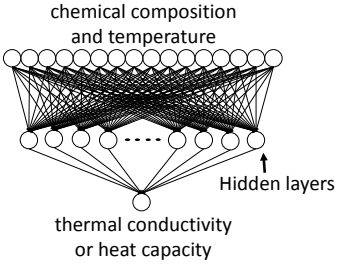

Fig. 2. *Architecture of the ANNs to estimate thermal conductivity and heat capacity*

Each database was divided into two parts. The first one (80 % of the information) was used for the training step, and the second one (20 % of the information) was used for the testing step.

1.3 Materials and Experimental Procedure

We worked with an experimental micro-alloyed steel designated as B2 (yield strength: 788 MPa), which was processed by a thermomechanical process for 11-mm thick producing plates. The chemical composition of the steel is: 0.03%C, 0.24%Si, 1.03%Mn, 0.42%Cr, 0.17%Mo, 1.30%Ni, 0.02%Nb and 0.02%Ti. In order to obtain the carbon equivalent, the Ito-Besseyo for low-C ranges steels was used:

$$P_{cm} = \%\mathrm{C} + \frac{\%\mathrm{Si}}{30} + \frac{\%\mathrm{Mn} + \%\mathrm{Cu} + \%\mathrm{Cr}}{20} + \frac{\%\mathrm{Ni}}{60} + \frac{\%\mathrm{Mo}}{15} + \frac{\%\mathrm{V}}{10} + 5(\%\mathrm{B}). \quad (9)$$

For this steel, the carbon equivalent is 0.15, which indicates that it does not have a tendency to form martensite during the cooling cycle; therefore, preheating was not performed.

In order to determine the effect of thermal cycles produced by welding on microstructure and micro-hardness in this experimental micro-alloyed steel, on a plate of 110 mm × 110 mm × 11 mm, with the gas tungsten arc welding (GTAW) process, an arc was created to simulate a one-pass welding without filler material, which means that a real weld was not made. To ensure the high quality of welding, the welding torch was adapted to a plasma cutting device as shown schematically in Fig. 3. As a result of this adjustment, the welding speed and the distance between the electrode and the plate were settled, keeping them constant. Table 3 shows the parameters used for welding in a single pass. After welding, the plate was left to cool down to room temperature.

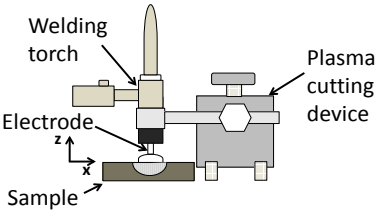

Fig. 3. *Adaptation of the welding torch to plasma cutting device*

To determine the effect of thermal cycles developed during the welding process on the microstructure, a metallographic preparation of welding was performed. This preparation consisted

of obtaining a sample in the transverse direction, in an area away from the boundaries of the beginning and end of the welding zone. To obtain the sample a diamond wheel cutting machine was used (Buehler Isomet 1000), with a controlled low speed to avoid any microstructural changes.

To reveal the microstructure using light microscopy, grinding, polishing, and etching were performed. The sequence of etching was a) 2 % nital during 5 s, b) 2% picral during 3 s and c) 1 % metabisulfite during 20 s. The average grain size in the HAZ was measured by the linear intercept method (ASTM E112). Finally, in accordance with ASTM 384, micro-hardness tests were performed using a Shimadzu Microhardness tester, model HMV-2. The profile of Vickers micro-hardness (HV 0.1) was measured in the welding zone from the FZ to the BM. The measurements were made with a separation of approximately 2.5 footprints.

Table 3. *Welding parameters used*

Current [A]	200
Welding velocity [cm/min]	18
Current type	Direct current electrode negative
Electrode	Tungsten with 2 % Rhodium
Electrode tip shape	pointed
Electrode diameter [mm]	3.18
Distance between plate and electrode [mm]	1.00

1.4 Determination of the Thermal Cycles

It is known that the mechanical properties are functions of the microstructure, and this is a function of the experimental thermal cycles. For this reason, the proposed method by Poorhaydari et al. **[25]** was used to determine the thermal cycles developed during welding, since the experimental determination is a complicated task. The method consists of applying a weight factor to Rosenthal's analytical solutions for thin and thick plates, since most of the welds exhibit an intermediate behaviour between these two categories. This weight factor is determined by:

$$F = \frac{\left(W_{\exp} - W_{Thick-plate}\right)}{\left(W_{Thin-plate} - W_{Thick-plate}\right)}, \qquad (10)$$

where, $W_{\exp}$ is the thickness of the experimentally determined HAZ; $W_{\text{Thin-plate}}$ and $W_{\text{Thick-plate}}$ are the thicknesses of the HAZ which are determined from Rosenthal's solutions for thin plate and thick plates, respectively. The weight factor, F, varies from 0 to 1. Values near 0 indicate that the problem is approaching a thick plate, and conversely, when F takes values close to 1, the problem is approaching a thin plate. $W_{\text{Thin-plate}}$ and $W_{\text{Thick-plate}}$ are determined, knowing that in the boundaries between the FZ and the HAZ, and between the HAZ and the BM, the peak temperatures reached during the welding process are known, and which correspond to the melting temperature and the critical temperature A_{c1}, respectively. Poorhaydari showed that the important parameters such as peak temperature and the cooling time between 1073 K and 773 K (commonly known as $t_{8/5}$) can be estimated by weighting the solutions of thick plates and thin plates; that these parameters can be used to correlate microstructure studies and modelling and simulation.

2 RESULTS AND ANALYSIS

After several ANNs with different neurons in the hidden layer were trained, the best fits between the actual and the estimated thermal properties were obtained with 8 neurons. The results of this step for the two ANNs are shown in Fig. 4.

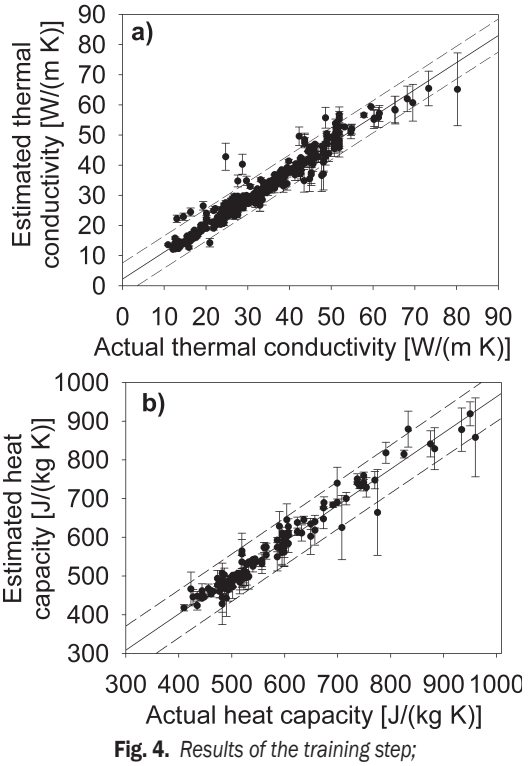

Fig. 4. *Results of the training step; a) thermal conductivity, b) heat capacity*

In this figure, the actual thermal conductivity and the actual heat capacity are compared with those

estimated with the ANNs. In the case of the thermal conductivity, it can be seen that with values higher than 60 W/(m K), an underestimation occurs for this property, but below this value most of the estimated values are close to actual values. For the case of heat capacity, it is observed that at values greater than 800 J/(kg K), there are both underestimation and overestimation of the data.

To determine the efficiency of the ANNs, the linear correlation coefficients were calculated, which are 0.94 for the thermal conductivity and 0.95 for the heat capacity. With these, it is considered that the ANNs have been trained.

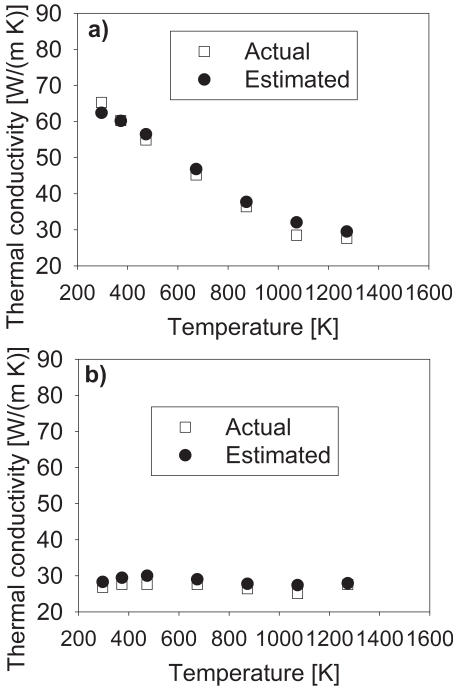

Fig. 5. *Comparison of actual and estimated thermal conductivity by using the ANN, for two different steels; a) 0.06%C, 0.4%Mn; b) 0.13%C, 0.25%Mn, 0.14%Ni, 12.95%Cr*

Once the ANNs have been trained, the thermal properties of the metallic materials that were not used in the training step were estimated in the testing step, but their actual thermal properties are already known. In Fig. 5, the actual and the estimated thermal conductivity by using the ANN are compared for two steels with different thermal behaviour as a function of temperature. In this figure, it can be seen that the ANN was able to estimate the thermal conductivity for both a non-alloy steel (Fig. 5a) and an alloyed steel (Fig. 5b). For the alloyed steel (i.e. ferritic stainless steel), the conductivity is not a strong function of temperature, which could be due to the fact that the ferritic phase is presented in all this temperature range. As in the case of the thermal conductivity, Fig. 6 compares the actual and the estimated heat capacity by using the respective ANN for two different steels that have different thermal behaviour as a function of temperature. As can be seen in Fig. 1b, heat capacity, depending on the steel, may or may not present a maximum around 900 K and 1100 K, which (as already mentioned), it may be due to the latent heat; however, the ANN is able to estimate this behaviour (Fig. 6a). As can be observed from Fig. 6, a good approximation between the actual and the estimated heat capacity is obtained. With these results, it is considered that the ANNs have been tested.

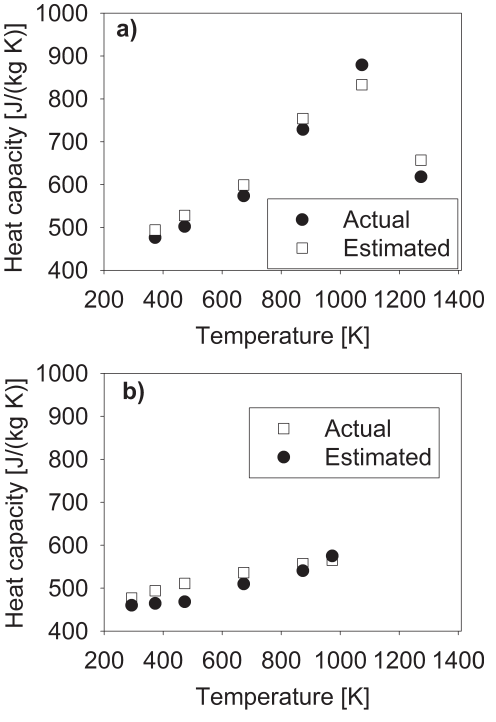

Fig. 6. *Comparison of actual and estimated heat capacity by using the ANN, for two different steels; a) 0.08%C, 0.05%Mn, 0.002Ni, b) 0.059%C, 0.46%Mn, 0.17%Ni, 0.28%Mo, 0.52%Cr*

Once the ANNs were trained and tested, the thermal properties of the micro-alloyed steel under study were estimated. The chemical composition of the micro-alloyed steel and the range of temperatures between 298 K and 1473 K, for the thermal conductivity, and the range of temperatures between 298 K and 1273 K for the heat capacity, were used as input neurons to estimate these thermal properties. Fig. 7 presents the results of the estimated thermal conductivity and the estimated heat capacity. From Fig. 7a, a maximum value of thermal conductivity

about 46 W/(m K) at room temperature is observed, with a tendency to decrease with the temperature until a stable value of approximately of 30 W/(m K) at 1073 K. Regarding the heat capacity (Fig. 7b), a high dependence on this property with temperature can be seen, reaching a maximum of 800 J/(kg K) at 1073 K; after this temperature, a decrease in this property is observed, until a minimum value of 402 J/(kg K) at 1273 K. With these results, it can be seen that this steel has thermal properties similar to that of an alloyed steel.

Fig. 8 presents the microstructures produced by the effect of the welding thermal cycles. The BM, the subzones of the HAZ: inter-critical heat effected zone (ICHAZ), recrystallization heat-affected zone (RCHAZ), coarse grained heat-affected zone (CGHAZ), partially melted heat-affected zone (PMHAZ), and the FZ can be seen. In the BM, microstructural changes are not observed, because the peak temperature reached in this zone was lower than the transformation critical temperature A_{c1}. The microstructure in this zone is composed mainly of acicular ferrite (AF) and quasi-polygonal ferrite (QPF), in addition to the presence of precipitates, which appear as dark particles on etchings with picral. The peak temperatures attained at the ICHAZ were between A_{c1} and A_{c3}; thus, a fraction of the ferrite of the original microstructure was transformed to austenite during heating; during the cooling cycle, the austenite transformed to ferrite. Additionally, in this subzone it can be seen a refining ferrite grain size, untransformed QPF and growth and agglomeration of

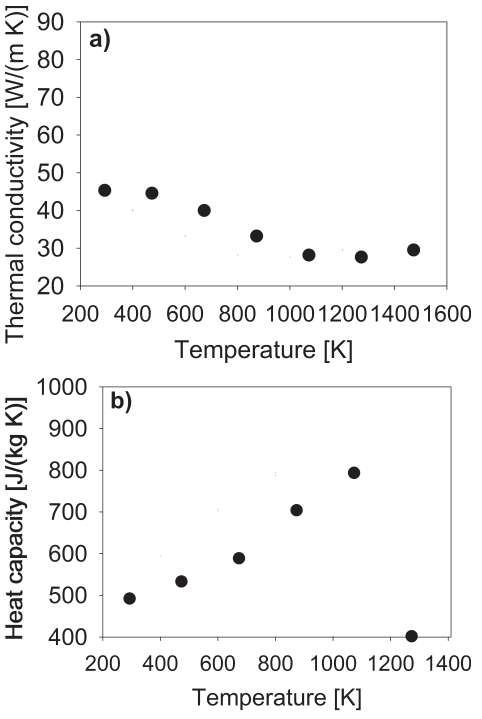

Fig. 7. *Estimated thermal properties for the experimental micro-alloyed steel; a) thermal conductivity, and b) heat capacity, by using the two ANNs*

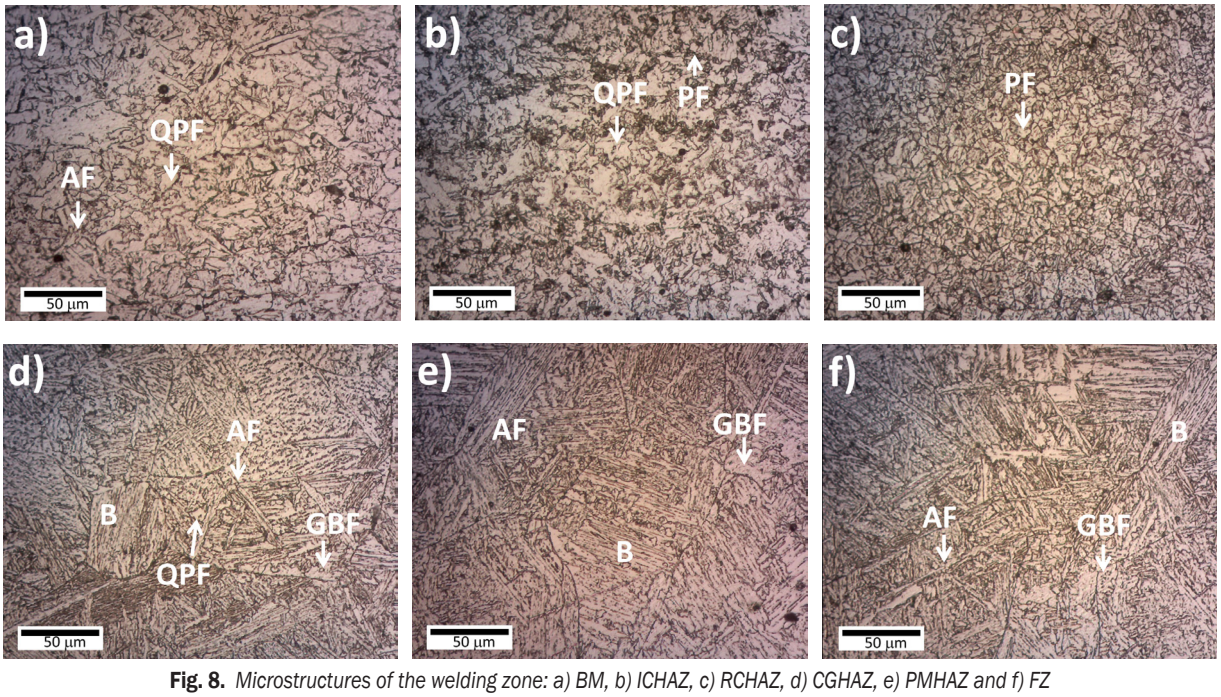

Fig. 8. *Microstructures of the welding zone: a) BM, b) ICHAZ, c) RCHAZ, d) CGHAZ, e) PMHAZ and f) FZ*

precipitates. The RCHAZ reached a peak temperature above A_{c3} but lesser than 1473 K; thus, all the original microstructure transformed to austenite during heating, resulting in the final refined microstructure of polygonal ferrite (PF) grains. In the CGHAZ, a grain coarsening with a microstructure of AF, QPF, grain boundary ferrite (GBF) and bainite (B) can be seen. In the PMHAZ, epitaxial grains and columnar grains that grew in the direction of the heat extraction are observed, in which these grains are composed of a mixture of AF, GBF and B. In the FZ, AF, GBF and B can be seen.

From Fig. 9, it can be seen that the micro-hardness increases in the HAZ from the BM to FZ. In the case of the RCHAZ, this increment is due to the grain refinement, but for the case of the CGHAZ, the increase in micro-hardness is mainly due to the formation of bainite, since in this subzone the grain is over 20 times higher.

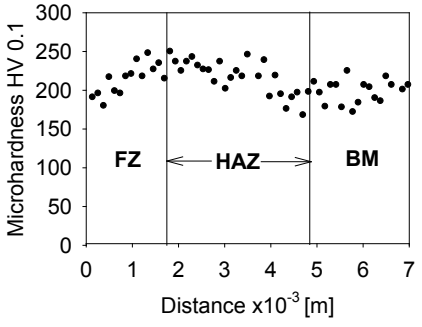

Fig. 9. *Microhardness profile measured in the welding zone*

Once the thermal properties of the experimental micro-alloyed steel were obtained, these were used to determine the peak temperatures and thermal cycles experimented in the HAZ, by solving the Rosenthal's equations and the method proposed by Poorhaydari et al. **[25]**. Fig. 10 shows the peak temperatures determined in the HAZ and BM, and its relationship with the grain size. It is noted that in the CGHAZ, a grain size between 30 μm and 115 μm was obtained; in the RCHAZ a grain size between 5 μm and 20 μm. From this same figure, it can be seen that the grain grew rapidly in the CGHAZ. According to the carbonitride dissolution temperature (Eq. (11) **[26]**), which for this steel is 1273 K, this rapid growth is due to the dissolution of these precipitates **[27]** and **[28]**.

$$\log\left(\left[Nb\right]\left[C+\frac{12N}{14}\right]\right)=2.26-\frac{6770}{T}. \qquad (11)$$

The temperature reached at the BM is less than 993 K, and for this, it did not cause microstructural changes; thus, the micro-hardness was not affected. In the same Fig. 10, the CGHAZ corresponded to peak temperatures between 1473 K and 1807 K; such temperatures cause a coarsening and dissolution of precipitates; grain growth was thus promoted.

From the thermal analysis, the cooling rates experimented in the CGHAZ and RCHAZ were of 69 K/s and 45 K/s, respectively. Thermal analysis showed that the high temperatures reached in the CGHAZ (between 1473 K and 1807 K) induced grain growth, which together with the high cooling rate (69 K/s), favoured the bainite formation. Furthermore, the peak temperatures reached in the RCHAZ (between 996 K and 1473 K), promoted the recrystallization with a grain size between 5 μm and 20 μm; this together with the lower cooling rate (45 K/s) inhibited the formation of bainite.

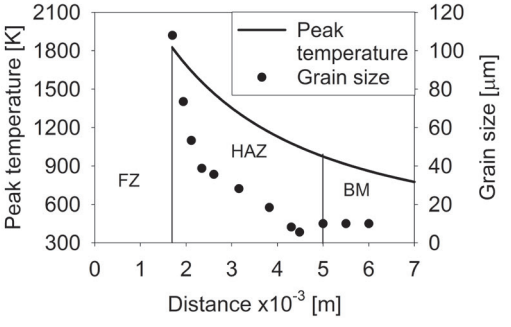

Fig. 10. *Determined peak temperatures and grain size*

3 CONCLUSIONS

Two ANNs were designed, trained and tested to estimate the thermal conductivity and the heat capacity of metallic materials as a function of chemical composition and temperature. The linear correlation coefficients obtained from the comparison between the actual and the estimated values are 0.94 and 0.95 for the thermal conductivity and the heat capacity, respectively.

By testing the ANNs, it was observed that these are able to estimate the thermal properties of any ferrous material that is within the boundaries of the chemical composition and temperature of the database.

Once the ANNs were tested, they were used to predict the thermal properties of an experimental micro-alloyed steel, and these properties were used to estimate the thermal cycles experimented in the HAZ of this same steel. It was observed that the microstructural features and the micro-hardness of the HAZ are functions of the experimented thermal

cycles. The microstructure in the HAZ changes from acicular ferrite, polygonal ferrite, grain boundary ferrite and bainite in the CGHAZ to polygonal ferrite in the RCHAZ. Additionally, in the HAZ and FZ, martensite was inhibited. Due to these microstructures that are functions of the thermal cycle, the CGHAZ showed the hardest zone, although there is no great difference of micro-hardness in the welding zone.

4 ACKNOWLEDGEMENTS

The authors are grateful to CONACyT (grant 178777 and 178511) for the financial support and for the scholarship (No 174555) to E. L.-M. The authors would also like to thank to UNAM PAPIIT grant IN118714 for the final support, and I. Puente-Lee and O. Flores from Faculty of Chemistry-UNAM.

5 REFERENCES

[1] Zinn, W., Scholtes, B. (2002). Residual stress formation processes during welding and joining. Totten, G., Howes, M., Inoue, T. (Eds.) *Handbook of Residual Stress and Deformation of Steel*, ASM International, Ohio, p. 391-397.

[2] Francis, J.A., Bhadeshia, H.K.D.H., Withers P.J. (2007). Welding residual stresses in ferritic power plant steels. *Materials Science and Technology*, vol. 23, no. 9, p. 1009-1020, **DOI:10.1179/174328407X213116**.

[3] Ismar, H., Burzic, Z., Kapor, N., Kokelj, T. (2012). Experimental investigation of high-strength structural steel welds. *Strojniški vestnik - Journal of Mechanical Engineering*, vol. 58, no. 6, p. 422-428, **DOI:10.5545/sv-jme.2011.281**.

[4] de Meester, B. (2001). Development of base materials for welding. *Science and Technology of Welding and Joining*, vol. 6, p. 159-167, **DOI:10.1179/13621710110153870**.

[5] Nazari, A., Milani, A.A., Zakeri, M. (2011). Modeling ductile to brittle transition temperature of functionally graded steels by artificial neural networks. *Computational Materials Science*, vol. 50, p. 2028-2037. **DOI:10.1016/j.commatsci.2011.02.003**.

[6] Lin, Y.C., Liu, G., Chen, M.-S., Zhong, J. (2009). Prediction of static recrystallization in a multi-pass hot deformed low-alloy steel using artificial neural network. *Journal of Materials Processing Technology*, vol. 209, p. 4611-4616, **DOI: 0.1016/j.jmatprotec.2008.10.020**.

[7] Kafkas, F., Karataş, Ç., Sozen, A., Arcaklioğlu E., Saritaş S. (2007). Determination of residual stresses based on heat treatment conditions and densities on a hybrid (FLN2-4405) powder metallurgy steel using artificial neural network. *Materials & Design*, vol. 28, p. 2431-2442, **DOI:10.1016/j.matdes.2006.09.003**.

[8] Hwang, R.-C., Chen, Y.-J., Huang, H.-C. (2010). Artificial intelligent analyzer for mechanical properties of rolled steel bar by using neural networks. *Expert Systems with Applications*, vol. 37, p. 3136-3139, **DOI: 10.1016/j.eswa.2009.09.069**.

[9] Sidhu, G., Bhole, S.D., Chen, D.L., Essadiqi E. (2011). Determination of volume fraction of bainite in low carbon steels using artificial neural networks. *Computational Materials Science*, vol. 50, p. 3377-3384, **DOI:10.1016/j.commatsci.2011.06.032**.

[10] Haque, M.E., Sudhakar, K.V. (2001). Prediction of corrosion–fatigue behavior of DP steel through artificial neural network. *International Journal of Fatigue*, vol. 23, p. 1-4, **DOI:10.1016/S0142-1123(00)00074-8**.

[11] Çöl, M., Ertunç, H.M., Yılmaz, M. (2007). An artificial neural network model for toughness properties in microalloyed steel in consideration of industrial production conditions. *Materials & Design*, vol. 28, p. 488-495, **DOI:10.1016/j.matdes.2005.09.001**.

[12] Castin, N., Fernández, J.R., Pasianot, R.C. (2014). Predicting vacancy migration energies in lattice-free environments using artificial neural networks. *Computational Materials Science*, vol. 84, p. 217-225, **DOI:10.1016/j.commatsci.2013.12.016**.

[13] Echeverri Restrepo, S., Tamayo Giraldo, S., Thijsse, B.J. (2014). Using artificial neural networks to predict grain boundary energies. *Computational Materials Science*, vol. 86, p. 170-173, **DOI:10.1016/j.commatsci.2014.01.039**.

[14] Saric, T., Simunovic, G., Simunovic, K. (2013). Use of Neural Networks in Prediction and Simulation of Steel Surface Roughness. *International Journal of Simulation Modelling*, vol. 12, p. 225-236, **DOI: 10.2507/ijsimm12(4)2.241**.

[15] Seyyedian, Choobi, M., Haghpanahi, M., Sedighi, M. (2012). Prediction of welding-induced angular distortions in thin butt-welded plates using artificial neural networks. *Computational Materials Science*, vol. 62, p. 152-159, **DOI:10.1016/j.commatsci.2012.05.032**.

[16] Ichikawa, K., Bhadeshia, H.K.D.H., MacKay, D.J.C. (1996). Model for solidification cracking in low alloy steel weld metals. *Science and Technology of Welding and Joining*, vol. 1, p. 43-50, **DOI:10.1179/stw.1996.1.1.43**.

[17] Manvatkar, V.D., Arora, A., De, A., DebRoy, T. (2012). Neural network models of peak temperature, torque, traverse force, bending stress and maximum shear stress during friction stir welding. *Science and Technology of Welding and Joining*, vol. 17, p. 460-466, **DOI:10.1179/1362171812y.0000000035**.

[18] Nolan, D., Sterjovski, Z., Dunne, D. (2005). Hardness prediction models based on HAZ simulation for in-service welded pipeline steels. *Science and Technology of Welding and Joining*, vol. 10, p. 681-694, **DOI:10.1179/174329305x65069**.

[19] Erzin, Y., Rao, B.H., Singh, D.N. (2008). Artificial neural network models for predicting soil thermal resistivity. *International Journal of Thermal Sciences*, vol. 47, p. 1347-1358, **DOI:10.1016/j.ijthermalsci.2007.11.001**.

[20] Eslamloueyan, R., Khademi, M.H. (2009). Estimation of thermal conductivity of pure gases by using artificial neural networks. *International Journal of Thermal Sciences*, vol 48, p. 1094-1101, **DOI:10.1016/j.ijthermalsci.2008.08.013**.

[21] Gitifar, V., Abbasi, A., Setoodeh, P., Poursadegh, M., Sahebnazar, Z., Alamdari, A. (2014). Modeling and analysis of the thermal conductivities of air saturated sandstone, quartz and limestone using computational intelligence. *International Journal of Thermal Sciences*, vol. 83, p. 45-55, **DOI:10.1016/j.ijthermalsci.2014.04.015**.

[22] Vuherer, T., Dunđer, M., Milović, L.J., Zrilić, M., Samardžić, I. (2013). Microstructural Investigation of the Heat-Affected

Zone of Simulated Welded Joint of P91 Steel. *Metalurgija*, vol. 52, p. 317-320.

[23] Ortin, J., Planes, A. (1988). Thermodynamic analysis of thermal measurements in thermoelastic martensitic transformations. *Acta Metallurgica*, vol. 36, p. 1873-1889, **DOI:10.1016/0001-6160(88)90291-X**.

[24] Brahme, A., Winning, M., Raabe, D. (2009). Prediction of cold rolling texture of steels using an Artificial Neural Network. *Computational Materials Science*, vol. 46, p. 800-804, **DOI:10.1016/j.commatsci.2009.04.014**.

[25] Poorhaydari, K., Patchett, B.M., Ivey, D.G. (2005). Estimation of Cooling Rate in the Weldign of Plates with Intermediate Thickness. *Welding Journal*, p. 149-155.

[26] Gladman T. (1997). *The Physical Metallurgy of Microalloyed Steels*, The Institute of Materials, London.

[27] Shome, M., Gupta, O.P., Mohanty, O.N. (2004). Effect of simulated thermal cycles on the microstructure of the heat-affected zone in HSLA-80 and HSLA-100 steel plates. *Metallurgical and Materials Transactions A*, vol. 35A, p. 985-996, **DOI:10.1007/s11661-004-0025-8**.

[28] Lei, X.W., Wang, H.H., Wu, K.M., Shirzadi, A.A., Yin, Y.Q., Wu, N.C. (2014). In situ observation of bainite to austenite transformation of microalloyed high strength steel during simulated welding cycle. *Science and Technology of Welding and Joining*, vol. 19, p. 402-407, **DOI:10.1179/1362171814y.0000000205**.

Vsebina

Strojniški vestnik - Journal of Mechanical Engineering
letnik 61, (2015), številka 12
Ljubljana, december 2015
ISSN 0039-2480

Izhaja mesečno

Razširjeni povzetki (extended abstracts)

Strojniški vestnik - Journal of Mechanical Engineering 61(2015)12, SI 127

Prejeto v recenzijo: 2015-06-24
Prejeto popravljeno: 2015-09-15
Odobreno za objavo: 2015-10-14

Lasersko podprto brušenje cirkonijevega oksida (ZrO_2) – priprava vzorca na vrhnji plasti in vrednotenje zmogljivosti

Xiaohong Zhang[1,2,*] – Zhaohui Deng[3] – Yinhui Ren[2] – Genyu Chen[2] – Wei Liu[3] – Gaofeng Zhang[4]

[1]Kolidž za strojništvo, Institut za znanost in tehnologijo v Hunanu, Kitajska
[2]Kolidž za strojništvo in tehniko vozil, Univerza v Hunanu, Kitajska
[3]Državni laboratorij province Hunan za visokoučinkovito in natančno obdelavo materialov, težavnih za odrezavanje, Kitajska
[4]Kolidž za strojništvo in tehniko vozil, Univerza v Xiangtanu, Kitajska

Kljub vse večjemu povpraševanju po izdelkih iz cirkonijevega dioksida je širjenje uporabe omejeno zaradi majhnih stopenj odvzema materiala in visokih stroškov obdelave, ki presegajo 75 % stroška komponente. Razrešitev težav, povezanih z natančnostjo in učinkovitostjo obdelave keramike ZrO_2, je zato pomembna za proizvodno industrijo.

Za tradicionalno lasersko podprto brušenje (LAG) so značilne omejene možnosti uporabe hladilne tekočine in površinske/podpovršinske razpoke, ki se tvorijo zaradi akumulacije toplote. Te težave predstavljajo ozko grlo pri praktični uporabi LAG in zato je predlagana nova strategija za lasersko pripravo površine keramike ZrO_2 na mokro brušenje (LIDWG). Cilj LIDWG je nadzorovano poškodovanje vrhnje plasti v enakomernih vzorcih kot priprava na visokoučinkovito brušenje. Proces LIDGW je sestavljen iz dveh različnih podprocesov: priprave in brušenja.

Članek obravnava nekatere ključne parametre obdelave, ki določajo mikrotopografijo in porazdelitev luknjic po vrhnji plasti, in sicer na podlagi mehanizmov oblikovanja luknjic s posameznimi laserskimi impulzi ter mehanizmov interakcije med sosednjimi točkami. Za enakomerno razporeditev luknjic je bil uporabljen pulzni vlakenski laser z nadzorom povprečne moči P_{avg}, razdalje defokusiranja z, stopnje prekrivanja laserskih točk U_S in stopnje prekrivanja laserskih sledilnih linij U_L. Nato je bil uporabljen tridimenzionalni (3D) mikroskop z ultraveliko globino polja (ULDF) za opazovanje nastanka luknjic, razporeditve in porazdelitve kombinacij luknjic. Podana je primerjava in diskusija razlik v brusilnih silah po laserski pripravi površine na mokro brušenje (LIDWG) in pri konvencionalnem brušenju (CG).

S povprečno močjo laserja (P_{avg}) 50 W in ustrezno gostoto moči laserja (I_p) približno $10{,}58\times10^7$ W/cm^2 je bila dosežena zadovoljiva laserska impulzna priprava površine keramike ZrO_2 in manj je bilo poškodb. Enakomerna porazdelitev lasersko izdelanih luknjic je bila dosežena pri stopnji prekrivanja U_S in U_L v višini 20 %. Uspešnost uporabljene strategije je dokazal primerjalni eksperiment brušenja. Normalne in tangencialne sile pri brušenju LIDWG so bile manjše kot pri konvencionalnem brušenju, največje zmanjšanje maksimalnih povprečnih normalnih (tangencialnih) sil pa je znašalo 59,2 % (62,9 %). To je mogoče pripisati manjšemu trenju ter boljšemu učinku mazanja/hlajenja zaradi spremembe načina odnašanja in možnosti shranjevanja brusilne tekočine v luknjicah.

Študija je bila usmerjena v natančen nadzor nad globino poškodovane plasti in mehanizmi odstranjevanja materiala, ki se pojavljajo v razmerah LIDWG. V nadaljnjem delu bo uporabljena metodologija enotne zasnove za preučitev laserske priprave in mokrega brušenja pri različnih procesnih spremenljivkah. Predlagan bo tudi pameten model za optimizacijo procesnih spremenljivk in kartiranje kompleksnih nelinearnih relacij med procesnimi spremenljivkami in želenimi rezultati.

Članek poroča o raznih eksperimentih z različnimi parametri brušenja, kot so hitrost brusilnega koluta, podajalna hitrost mize, globina brušenja in hitrost obdelovanca, z namenom obvladovanja površinske hrapavosti, preostalih napetosti in podpovršinskih poškodb. Pri manjših globinah brušenja in večjih hitrostih koluta je bil dokazano dosežen duktilen način odnašanja materiala. Slabost postopka je v majhni produktivnosti in v velikih stroških. Obdelava LIDWG omogoča v primerjavi s tradicionalnimi postopki brušenja keramike ZrO_2 večje stopnje odnašanja materiala pri brušenju, izognemo pa se tudi večjim silam pri brušenju, višjim temperaturam, obrabi brusilnega koluta ter napakam zaradi obrabe brusilnega koluta in krhkega odnašanja materiala.

Ključne besede: lasersko izdelane luknjice, priprava vrhnje plasti, porazdelitev, mokro brušenje, sila pri brušenju, cirkonijev oksid

*Naslov avtorja za dopisovanje:Kolidž za strojništvo, Institut za znanost in tehnologijo v Hunanu, Kitajska. jansbomb@126.com

Strojniški vestnik - Journal of Mechanical Engineering 61(2015)12, SI 128

Prejeto v recenzijo: 2015-06-19
Prejeto popravljeno: 2015-09-04
Odobreno za objavo: 2015-10-14

Avtomatsko razpoznavanje zvokov strojev v hrupnem delovnem okolju

Primož Lipar* – Mirko Čudina – Peter Šteblaj – Jurij Prezelj
Univerza v Ljubljani, Fakulteta za strojništvo, Slovenija

Postopki za avtomatizirano zaznavanje napak v končni kontroli izdelka, ali v samem proizvodnem procesu, so vse pogostejši. V ta namen so primerne metode, ki lahko na podlagi zvočnega signala, izdelka, stroja, naprave ali obdelovalnega postopka določijo njihova trenutna stanja. V tem delu so predstavljene metode za razpoznavanje različnih zvokov strojev, naprav in obdelovalnih postopkov, ki jih lahko uporabimo celo za nadzor celotnega proizvodnega procesa. Metode temeljijo na transformaciji biometrične zaznave govora, oziroma identifikacije govorcev, na identifikacijo različnih zvokov strojev, naprav in obdelovalnih postopkov z uporabo algoritmov za identifikacijo oseb na podlagi govornega signala.

Pri procesu identifikacije zvočnega signala ločimo fazo parametrizacije in fazo klasifikacije. V fazi parametrizacije se s pomočjo metode koeficientov frekvenčnega kepstra (KFC) iz zvočnih signalov izlušči le značilne lastnosti (značilke) posameznega zvoka stroja. Pri KFC metodi se za govorne signale uporablja filtre z melodično razporeditvijo centralnih frekvenc. Takšna razporeditev je neposredno povezana z naravo človeškega govora in slušnega sistema. Ker se človeški govor razlikuje od zvoka strojev in naprav, ki so v osnovi manj dinamični in manj barviti, smo poleg melodične predlagali še linearno in logaritemsko razporeditev centralnih frekvenc filtrov.

V procesu klasifikacije ločimo fazo učenja in fazo razpoznavanja. V fazi učenja se na podlagi znanih značilk izdelajo statistični modeli zvokov, ki jih generira posamezni vir. V fazi razpoznavanja pa algoritem razvršča značilke neznanega zvočnega signala v posamezne razrede. Za klasifikacijo zvočnega signala sta bila uporabljena dva algoritma; algoritem K-najbližjih sosedov (KNS) in na novo predlagani algoritem, ki temelji na več-variacijski Gaussovi porazdelitvi (VGP). VGP je, za razliko od KNS, parametrična metoda. V fazi razpoznave se z razvrščanjem neznanih značilk v obstoječe statistične modele, meri stopnja ujemanja s posameznim modelom.

Za praktični primer klasifikacije smo posneli zvok petih različni strojev in zvok v industrijski hali, kjer je prisotnih več zvokov iz več različnih strojev in naprav. Zvok industrijske hale smo uporabili kot šum, ki smo ga dodajali v čiste zvočne signale strojev. S primerno obdelavo signalov smo vsem petim zvočnim signalom strojev zagotovili enako razmerje signal/šum (RSŠ) 7 dB, 2 dB in –2 dB. Signali z različnimi RSŠ so služili kot osnova pri izvedbi testa robustnosti KNS in VGP metode.

Rezultati testa robustnosti kažejo, da je parametrizacija zvokov strojev s KFK metodo najbolj učinkovita pri uporabi linearne razporeditve filtrov. Uspešnost klasifikacije je bila pri obeh metodah (KNS in VGP) zelo dobra, tudi pri nizkem RSŠ. Zato lahko zaključimo, da se z KFK parametrizacijo ter VGP in KNS metodo lahko uspešno ločuje med različnimi zvoki strojev in naprav oziroma njihovimi stanji. Za delovanje v realnem času pa je VGP parametrična metoda primernejša, saj je čas določevanja oziroma identifikacije mnogo krajši kot pri metodi KNS.

Predlagana metoda, se lahko uporabi tudi za zaznavanje napak v proizvodnem procesu, za odkrivanje napak na izdelkih v končni kontroli kakovosti, za markiranje okoljskega hrupa pri meritvah v naravnem in življenjskem okolju, itd. V prihodnosti nameravamo raziskati še ostale metode za parametrizacijo ter njihov vpliv na uspešnost razpoznave, ter nadgraditi obstoječ sistem za klasifikacijo z metodo mešanice Gaussovih porazdelitev.

Ključne besede: zvok strojev, klasifikacija zvoka strojev, KNS klasifikator, VGP klasifikator, koeficienti frekvenčnega kepstra

*Naslov avtorja za dopisovanje: Univerza v Ljubljani, Fakulteta za strojništvo, Aškerčeva 6, 1000 Ljubljana, Slovenija, primoz.lipar@fs.uni-lj.si

Strojniški vestnik - Journal of Mechanical Engineering 61(2015)12, SI 129

Prejeto v recenzijo: 2015-06-05
Prejeto popravljeno: 2015-09-03
Odobreno za objavo: 2015-10-14

Analiza koeficienta Coulombovega trenja pri preoblikovanju pločevine DC05

Gillo Giuliano*
Univerza v Cassinu, Italija

Članek predstavlja analizo koeficienta Coulombovega trenja pri preoblikovanju pločevine po metodi končnih elementov in na podlagi eksperimentalnih rezultatov Erichsenovega testa. Kadarkoli je orodje med preoblikovanjem v stiku z obdelovancem, se med pločevino in orodjem pojavijo tangencialne torne sile. Trenje vpliva na tok kovine, na stroške in kakovost izdelkov ter na obrabo orodja, zato ga zmanjšujemo z uporabo maziv.

Za natančno analizo procesov preoblikovanja pločevine se najpogosteje uporablja metoda končnih elementov. Analiza po metodi končnih elementov zahteva modeliranje mehanskih lastnosti kovinske pločevine ter trenja med pločevino in orodji, ki se uporabljajo v procesu preoblikovanja. V eksperimentalno-numeričnem pristopu je bil uporabljen standardni Erichsenov test za določitev koeficienta Coulombovega trenja na stiku med orodjem za prebijanje in pločevino. Nekateri vidiki Erichsenovega testa za merjenje trenja na stiku so bili preučeni po metodi končnih elementov. Med različnimi modeli trenja, ki so opisani v literaturi, je Coulombov model najprimernejši za postopek hladnega preoblikovanja, kjer je pločevina v intenzivni interakciji z orodjem. Za izračun koeficienta trenja se uporabi Erichsenov standardni test, ki je v primerjavi z ostalimi bistveno preprostejši in obenem omogoča določitev lastnosti pločevinastega materiala.

Članek opisuje identifikacijo koeficienta Coulombovega trenja pri preoblikovanju pločevine na podlagi primerjave numeričnih in eksperimentalnih rezultatov. Na napravi za preoblikovanje, ki je bila zasnovana v laboratoriju na Univerzi v Cassinu, so bili opravljeni eksperimenti z orodjem za prebijanje iz nerjavnega jekla in jekleno pločevino DC05. DC05 je maloogljično jeklo, ki ni podvrženo staranju ter je še posebej primerno za globoki vlek in za posebne aplikacije, kot so avtomobilske komponente in karoserijski deli, konstrukcijski elementi, gospodinjski aparati ipd. Vzorci so bili preizkušeni brez mazanja in z mastjo LB4 (litijeva mast, ki vsebuje trdno mazivo MoS_2). Koeficient Coulombovega trenja je znašal 0,29 v nemazanih pogojih in 0,17 pri uporabi masti LB4. Opravljeni sta bili dve numerični simulaciji Erichsenovega testa z omenjenima vrednostma koeficienta trenja. Rezultati numerične simulacije v primerjavi z rezultati eksperimentov podcenjujejo debelino na vrhu vzorca (z napako v višini 14 % oz. 9 % v pogojih brez mazanja in z mazanjem) in precenjujejo razdaljo (z napako v višini 12 % oz. 2 %). Numerični rezultati se torej dobro ujemajo z eksperimentom, še posebej pri uporabi masti LB4.

Opravljena je bila preprosta analiza koeficienta Coulombovega trenja pri preoblikovanju pločevine z uporabo standardnega Erichsenovega testa. Ugotovljene vrednosti koeficienta trenja so bile uporabljene pri numerični simulaciji Erichsenovega testa. Numerični rezultati se dobro ujemajo z rezultati eksperimenta, zlasti pri uporabi masti LB4.

Ključne besede: koeficient Coulombovega trenja, preoblikovanje pločevine, metoda končnih elementov, Erichsenov test, togo-plastično vedenje, pločevina DC05

*Naslov avtorja za dopisovanje: Univerza v Cassinu, DICeM, via Di Biasio, 43, 03043 Cassino, (FR) Italija, giuliano@unicas.it

Strojniški vestnik - Journal of Mechanical Engineering 61(2015)12, SI 130

Prejeto v recenzijo: 2015-05-29
Prejeto popravljeno: 2015-09-15
Odobreno za objavo: 2015-11-09

Napovedovanje kakovosti laserskega reza volframove zlitine z uporabo nevronske mreže

Simon Klancnik[1] – Derzija Begic-Hajdarevic[2,*] – Matej Paulic[1] – Mirko Ficko[1] – Ahmet Cekic[2] – Maida Cohodar Husic[2]

[1] Univerza v Maribor, Fakulteta za strojništvo, Slovenija
[2] Univerza v Sarajevu, Fakulteta za strojništvo, Bosna in Hercegovina

V članku analiziramo vpliv procesnih parametrov na kakovost laserskega razreza pločevine iz volframove zlitine (W ≈ 92.5 %, preostanek Fe in Ni) z debelino 1 mm. Zlitina se uporablja na različnih področjih, na primer v medicinskih aplikacijah, v avtomobilski in v letalski industriji. Eksperimente smo izvedli z uporabo CO_2 laserja proizvajalca Rofin (model DC020), z nazivno izhodno močjo 2000 W v načinu CW pri valovni dolžini 10.6 μm ter visokokakovostnim žarkom (faktor kakovosti laserskega žarka K = 0.95). Eksperimenti so bili opravljeni v Nemčiji na Visoki šoli v Jeni. Za usmerjanje laserskega žarka je bila uporabljena ZnSe leča s fokusno razdaljo 127 mm. Pomožni plin je bil uporabljen soosno z laserskim žarkom skozi šobo z izhodnim premerom 2 mm. Položaj šobe, tlak pomožnega plina ter goriščna razdalja so bili skozi celoten eksperiment konstantni. Vrednosti teh procesnih parametrov so bile izbrane na podlagi predhodnih eksperimentalnih študij. Pri določevanju optimalnih procesnih parametrov smo upoštevali naslednja merila: širino reza, kakovost površine reza ter ostanek taline na spodnjem robu reza. V raziskavi smo spreminjali tri vhodne procesne parametre: moč laserja, hitrost rezanja ter vrsto pomožnega plina (kisik, dušik in zrak). Delovno območje rezalnih hitrosti smo izbrali na podlagi predhodnih eksperimentov za vsak pomožni plin in moč laserja. Za ocenjevanje kakovosti laserskega razreza smo v okviru opravljene raziskave uporabili širino reza ter povprečno hrapavost površine. Hrapavost površine reza je bila izmerjena vzdolž reza približno na sredini debeline pločevine kot povprečna hrapavost R_a z uporabo merilnika hrapavosti Taylor-Hobson. Širino reza smo izmerili z uporabo Zeissovega optičnega mikroskopa Stemi opremljenega z video kamero in lečami za povečave.

V obstoječi literaturi ni mogoče zaslediti večjega števila raziskav na področju uporabe CO_2 laserja za razrez ognjevzdržnih materialov. V raziskavi smo za napovedovanje kakovosti CO_2 laserskega razreza pločevine iz volframove zlitine uporabili model umetne nevronske mreže, z učnim algoritmom vzvratnega širjenja. Nevronska mreža ima tri nevrone na vhodni plasti ter dva nevrona na izhodni plasti. Sestavljena je iz štirih skritih plasti, in sicer osem nevronov v prvi skriti plasti, petnajst nevronov v drugi skriti plasti, pet nevronov v tretji skriti plasti ter dva nevrona v četrti skriti plasti. Takšno topologijo nevronske mreže smo izbrali na podlagi testiranj različnih topologij. Izkazala se je kot najučinkovitejša za reševanje našega problema, saj smo z njo dosegli najmanjšo povprečno napako napovedovanja. Za učenje nevronske mreže smo uporabili podatke pridobljene na podlagi opravljenega eksperimenta. Celotna baza eksperimenta je bila sestavljena iz 42 vzorcev, od tega smo 34 vzorcev uporabili za učenje nevronske mreže, 8 naključno izbranih vzorcev pa smo uporabili za testiranje učinkovitosti naučene nevronske mreže. Povprečna napaka napovedovanja je bila 5,5 % za širino reza ter 9,5 % za kakovost površine. Iz rezultatov je očitno, da je napaka napovedovanja za širino reza manjša kot napaka pri napovedovanja hrapavosti površine, vendar lahko iz rezultatov sklepamo, da je razviti ANN model primeren za napovedovanje obeh veličin.

V delu je predstavljeno, da je imela izbira pomožnega plina največji vpliv na kakovost reza, zlasti na širino reza. Napovedovati kakovost reza pred dejansko izvedbo reza, predstavlja za uporabnike korist v smislu znižanja stroškov in prihranka časa. Z razvitim modelom lahko uporabnik pred izvedbo laserskega razreza izbere rezalno hitrost, moč laserja ter vrsto pomožnega plina tako, da so dosežene optimalne karakteristike laserskega razreza.

Ko v praksi režemo redek ali celo neznan material, moramo najprej določiti procesne parametre tako, da bomo dosegli zadostno kakovost razreza. Predstavljeno delo omogoča določitev teh parametrov z izvedbo manjšega števila eksperimentov in brez potrebe po analizi vseh možnih medsebojnih vplivov. V prihodnosti bi bilo smiselno raziskave na tem področju razširiti na raziskovanje vpliva različnih procesnih parametrov, kot je tlak pomožnega plina, goriščni položaj leče, položaj šobe, vrsta in debelina materiala, na različne karakteristike kakovosti razreza, kot je toplotno vplivna cona, mikrostruktura in mikrotrdota.

Ključne besede: laserski razrez, umetna nevronska mreža, volframova zlitina, hrapavost površine, širina reza, procesni parametri

*Naslov avtorja za dopisovanje: Univerza v Sarajevu, Fakulteta za strojništvo, Vilsonovo setaliste 9, Sarajevo, Bosna in Hercegovina, begic@mef.unsa.ba

Strojniški vestnik - Journal of Mechanical Engineering 61(2015)12, SI 131

Prejeto v recenzijo: 2015-05-13
Prejeto popravljeno: 2015-09-29
Odobreno za objavo: 2015-10-14

Spremembe lastnih frekvenc zaradi hude korozije kovinskih konstrukcij

Gilbert-Rainer Gillich* – Zeno Iosif Praisach – Vasile Iancu – Horia Furdui – Ionica Negru
Univerza Eftimie Murgu v Resiti, Fakulteta za strojništvo, Romunija

Degradacija tehničnih konstrukcij zaradi korozije vpliva na njihovo varnost, saj zmanjšuje presek nosilnih komponent in spreminja mehanske lastnosti materiala. Te spremembe parametrov lahko spremljamo prek premika lastnih frekvenc. Namen članka je predstavitev matematičnih relacij, ki napovedujejo spremembe frekvenc zaradi splošne ali lokalne korozije na podlagi znane izgube mase in zmanjšanja upogibne togosti. Analitična raziskava se začne z vplivom mase rezin na različnih mestih nosilca. Rezultati so pokazali, da položaj rezine določa količino energije, ki prispeva k celotni energiji, shranjeni v nosilcu v danem vibracijskem načinu. Količina energije v različnih načinih se razlikuje in je odvisna od kvadrata oblike načina na mestu rezine. Na ta način je bilo pokazano, da porazdelitev kinetične energije odraža prispevek mase v celotni shranjeni energiji in tako omogoča napovedovanje spremembe frekvenc zaradi izgubljene mase. Drugi pristop je bil usmerjen v raziskovanje vpliva zmanjšanja togosti na lastne frekvence. Efektivni upogibni moment je definiran kot moment, ki zagotavlja enak učinek (enak upogib) na zdravem nosilcu kot realni moment na korodiranem nosilcu. Ob zmanjšanju prereza v dani rezini nosilca lahko v tem območju pričakujemo povečanje efektivnega momenta in s tem povečanje deformacijske energije. Dejanski učinek nezveznosti je zmanjšanje energije in kot kazalec položaja napake je bila zato opredeljena modalna porazdelitev deformacijske energije. Ti dve relaciji med strukturnimi spremembami in frekvenčnim premikom sta bili izraženi v obliki matematičnih formul, ki omogočajo napovedovanje frekvenčnih sprememb zaradi glavnih učinkov korozije – izgube mase in zmanjšanja togosti. Omeniti je treba, da niso bile upoštevane perturbacije efektivnega upogibnega momenta v prehodnih območjih, ki se nahajajo v bližini mest zmanjšanega prereza. Pri rezultatih, izpeljanih iz teh relacij, lahko zato pričakujemo manjše napake pri izgubi togosti.

Točnost pridobljenih matematičnih relacij je bila preučena na primeru konzolnega nosilca z numerično simulacijo in z eksperimentalnimi rezultati. V ta namen so bili razviti trije modeli po metodi končnih elementov z različnimi vrednostmi in mesti zmanjšanja prereza. Zasnovani so bili tudi modeli, ki individualno obravnavajo izgubo mase in zmanjšanje togosti. Primerjava računskih rezultatov na podlagi izpeljanih relacij in rezultatov simulacij po metodi končnih elementov je pokazala dobro korelacijo pri izgubi mase in zadovoljivo ujemanje pri zmanjšanju togosti. Napake napovedi zmanjšanja togosti so še vedno sprejemljive pri koroziji v manjšem obsegu in pri pomembnem zmanjšanju preseka. Boljši rezultati so bili pridobljeni pri razširjeni koroziji z majhno globino, saj je tam prehod efektivnega upogibnega momenta bolj gladek kot pri hudi lokalni koroziji.

Preizkušen je bil tudi realen korodiran nosilec. Primerjava z rezultati numeričnih simulacij je pokazala, da so modeli po MKE zanesljivi in da dobro odražajo vedenje realnih sistemov. Zato je popolnoma upravičen zaključek, da izpeljane matematične relacije dajejo točne rezultate.

Relacije, predstavljene v tem članku, omogočajo napovedovanje premika frekvenc pri znanih spremembah konstrukcij ter omogočajo ustvarjanje podatkovnih baz z referenčnimi vrednostmi za možne scenarije poškodb. Vrednotenje korozije tako na podlagi teh informacij postane obraten problem, ki je enostavno rešljiv s statističnimi metodami.

Ključne besede: vrednotenje korozije, konzolni nosilec, izguba mase, zmanjšanje togosti, premik lastnih frekvenc

*Naslov avtorja za dopisovanje: Univerza Eftimie Murgu v Resiti, Fakulteta za strojništvo, Traian Vuia Square 1-4, Resita, Romunija, gr.gillich@uem.ro

Strojniški vestnik - Journal of Mechanical Engineering 61(2015)12, SI 132

Prejeto v recenzijo: 2015-06-26
Prejeto popravljeno: 2015-09-11
Odobreno za objavo: 2015-10-06

Analiza pretočnega polja in črpalne zmogljivosti brezventilske piezoelektrične črpalke s skupino poloblastih segmentov

Caiqi Hu[1] – Jing Ji[1,*] – Xiaoqi Hu[2] – Jude Liu[3] – Shengduo Li[1]

[1] Kolidž za strojništvo in elektrotehniko, Kmetijska univerza Qingdao, Kitajska
[2] Kolidž za inženiring in dizajn, Univerza Lishui, Kitajska
[3] Državna univerza v Pensilvaniji, Oddelek za kmetijski in biološki inženiring, ZDA

Prednost brezventilske piezoelektrične črpalke s skupinami poloblastih segmentov (VPPHSG) pred ostalimi brezventilskimi črpalkami je v preprosti zgradbi in v dobri izvedljivosti. Poloblasti segmenti (HS) pri VPPHSG so razporejeni tako, da delujejo kot ventil brez premikajočih se delov.

Ko se fluid pretaka prek skupine poloblastih segmentov (HSG), nastanejo v interakciji fluida in poloblastih segmentov turbulence in vrtinci, ki ustvarijo zelo kompleksno pretočno polje in tlačne razlike. Te turbulence oziroma vrtinci povzročijo mešanje fluida in tlačno razliko, ki ustvari pretok skozi črpalko. Zato je pomembno poznavanje interakcij med parametri HSG in pretokom fluida za kvantifikacijo njihovega vpliva na pretočno polje črpalke in pretoke, ki je nujno pri snovanju in raziskavah tovrstnih brezventilskih črpalk. V dostopni literaturi ni bilo mogoče najti študij, ki bi kvantitativno opisovale razmerja med pretoki in konstrukcijskimi parametri črpalke, vključno z dimenzijami in razporeditvijo HSG.

V tej raziskavi je bila preučena zmogljivost črpanja in mešanja brezventilske piezoelektrične črpalke na podlagi teorije hidrodinamike in z uporabo numeričnih metod za simulacijo pretočnih polj. Na osnovi teoretične analize zmogljivosti črpanja, sprememb v hitrostnem polju fluida in tlačnih razlik je bila simulirana odvisnost koeficienta upora in pretokov v odvisnosti od dimenzij in razporeda HSG s komercialno profesionalno programsko opremo FLUENT.

Rezultati simulacije so razkrili kvantitativna razmerja med tlačnim poljem, pretoki, številom vrst in stolpcev ter intervali med vrstami in stolpci v HSG. Rezultati simulacije so pokazali, da se lahko pretok poveča z večjo razliko v pretočnem uporu pretočnega polja, ki je mogoče zagotoviti s povečanjem števila vrst in stolpcev, s povečanjem intervala med vrsticami, ali pa z zmanjšanjem intervala med stolpci. Ugotovljeno je bilo tudi, da je učinek črpanja bistveno večji v primeru, da se poveča število vrst, kot pa če se poveča število stolpcev. Povečanje intervalov med vrstami in stolpci lahko poveča velikost in jakost vrtinca v črpalki ter tako izboljša učinkovitost mešanja črpalke. Rezultati simulacije so bili preizkušeni in verificirani z eksperimenti, v katerih je bil ugotovljen pretok črpalke. Raziskava je pokazala, da imajo simulacija, teoretična analiza in rezultati eksperimentov enak trend, čeprav so bila odstopanja simuliranih pretokov od izmerjenih razmeroma velika. Simulacija pretočnega polja črpalke je torej lahko učinkovit pripomoček za snovanje v fazi izdelave koncepta, velike razlike med simuliranimi in izmerjenimi rezultati pa postavljajo omejitve glede uporabnosti te metode v inženirski praksi. Razvita in uspešno preizkušena je bila simulacija pretočnega polja v tovrstni brezventilski črpalki.

Za izboljšanje uspešnosti simulacij bodo potrebne še dodatne študije in za verifikacijo simulacije se lahko uporabi druga programska oprema. Predlagan in preučen je bil spreminjajoč vzorec zmogljivosti črpanja in mešanja za brezventilsko piezoelektrično črpalko s HSG. Pomen te raziskave je v simulaciji edinstvenega pretočnega polja črpalke s spreminjajočim se številom vrst in stolpcev oz. intervalom med vrstami in stolpci v HSG. Rezultati simulacije lahko dajo smernice za preučevanje mešanja in zmogljivosti črpanja mikrotokov ali malih tokov fluidov. Ta simulacija je dragocena tudi pri preverjanju inovativnih konceptov zasnove črpalk.

Ključne besede: skupina poloblastih segmentov, polje, brezventilska piezoelektrična črpalka, mešanje, pretok

*Naslov avtorja za dopisovanje:Kolidž za strojništvo in elektrotehniko, Kmetijska univerza Qingdao, Qingdao, Kitajska, hucaiqi@163.com

Strojniški vestnik - Journal of Mechanical Engineering 61(2015)12, SI 133

Prejeto v recenzijo: 2015-04-16
Prejeto popravljeno: 2015-07-17
Odobreno za objavo: 2015-09-02

Umetne nevronske mreže za ocenjevanje toplotnih lastnosti eksperimentalnega mikrolegiranega jekla in njihova uporaba pri toplotni analizi varjenja

Edgar López-Martínez[1,*] – Héctor Javier Vergara-Hernández[2] – Sergio Serna[3] – Bernardo Campillo[1,4]

[1] Mehiška avtonomna nacionalna univerza, Fakulteta za kemijo, Mehika
[2] Inštitut za tehnologijo Morelia, Podiplomski program metalurgije, Mehika
[3] Avtonomna univerza zvezne države Morelos, Raziskovalno središče za tehniko in aplikativne vede, Mehika
[4] Mehiška avtonomna nacionalna univerza, Inštitut za fiziko, Mehika

Izdelava jeklenih metalurških komponent zahteva poznavanje toplotnih lastnosti v funkciji temperature. Pri procesih, kot sta varjenje in toplotna obdelava jekel, je nujno poznavanje toplotne prevodnosti in specifične toplote za snovanje, simulacijo in izbiro ciklov segrevanja in ohlajevanja, od katerih bo odvisna mikrostruktura in posledično mehanske lastnosti materiala. Namen predstavljene študije je ocenitev teh toplotnih lastnosti in njihova uporaba pri toplotni analizi toplotno vplivanega področja pri varjenju eksperimentalnega mikrolegiranega jekla.

Toplotna analiza varjenja vključuje določanje dejanskih toplotnih ciklov. Zaradi težav, ki se pojavljajo pri eksperimentalnem določanju teh ciklov, pa so bili le-ti opredeljeni z uporabo utežnih faktorjev na Rosenthalovih analitičnih rešitvah. Ker smo delali z eksperimentalnim jeklom, toplotne lastnosti niso znane. Umetne nevronske mreže (ANN) so se izkazale za zmogljivo orodje za napovedovanje parametrov ter simulacijo in odpravljanje težav pri tehniških aplikacijah, zato je bila sprejeta odločitev, da bosta za oceno omenjenih toplotnih lastnosti zasnovani dve ANN.

Za določitev toplotnih lastnosti v funkciji kemične sestave in temperature sta predlagani dve ANN v zasnovi večslojnega perceptrona z vzvratnim učenjem, momentnim učnim pravilom in sigmoidno prenosno funkcijo. Na podlagi podatkov iz literature sta bili zgrajeni dve zbirki podatkov kovinskih materialov. Obe ANN sta bili naučeni in preizkušeni z eno skrito plastjo in različnim številom nevronov v tej plasti. Ko sta bili obe ANN naučeni in preizkušeni, so bile ocenjene toplotne lastnosti eksperimentalnega mikrolegiranega jekla. Kemična sestava mikrolegiranega jekla, toplotna prevodnost v temperaturnem območju od 298 K do 1473 K in specifična toplota v temperaturnem območju od 298 K do 1273 K so bile uporabljene kot vhodni nevroni za ocenjevanje teh toplotnih lastnosti. Le-te so bile nato uporabljene za določitev vršnih temperatur in toplotnih ciklov v toplotno vplivanem področju (TVP) z uporabo utežnega faktorja na Rosenthalovih analitičnih rešitvah za tanke in debele plošče.

Po učenju več ANN z različnim številom nevronov v skriti plasti je bilo ugotovljeno najboljše ujemanje med dejanskimi in ocenjenimi toplotnimi lastnostmi pri osmih nevronih. Za določitev učinkovitosti ANN sta bila izračunana koeficienta linearne korelacije, ki znašata 0,94 za toplotno prevodnost in 0,95 za specifično toploto. Sledi sklep, da sta ANN naučeni. V fazi preizkušanja so bile ocenjene tiste toplotne lastnosti kovinskih materialov, ki niso bile uporabljene pri učenju. Dejanske vrednosti toplotnih lastnosti so znane in rezultati kažejo, da sta ANN uporabni za ocenjevanje toplotne prevodnosti in specifične toplote.

Toplotna analiza je pokazala, da visoke temperature v grobozrnatem TVP (med 1473 K in 1807 K) spodbujajo rast zrn, ki skupaj s hitrim ohlajanjem (69 K/s) privede do formiranja bainita. Vršne temperature v rekristalizacijskem TVP (med 996 K in 1473 K) pospešujejo rekristalizacijo z velikostjo zrn med 5 μm in 20 μm, kar skupaj z majhno hitrostjo ohlajevanja (45 K/s) preprečuje formiranje bainita.

Privzeto je bilo, da so toplotne lastnosti samo funkcija kemične sestave in temperature, ne pa tudi prisotnih faz, o katerih ni informacij.

Toplotne lastnosti kovinskih materialov je mogoče ocenjevati le v območju temperatur in kemičnih sestav, ki ustreza razponu vrednosti v uporabljeni zbirki podatkov.

S predstavljeno zasnovo ANN je mogoče oceniti toplotno prevodnost in specifično toploto vsakega kovinskega materiala s kakršnokoli kemično sestavo in temperaturo znotraj območja vrednosti, iz katerih je bila sestavljena zbirka podatkov.

Ključne besede: specifična toplota, toplotna prevodnost, mikrolegirano jeklo, toplotno vplivano področje, umetna nevronska mreža, varjenje

*Naslov avtorja za dopisovanje: Mehiška avt. nacionalna univerza, Fakulteta za kemijo, Av. Universidad 3000, Mexico City, Mehika, edgar0902@comunidad.unam.mx

Doktorske disertacije, znanstveno magistrsko delo

DOKTORSKE DISERTACIJE

Na Fakulteti za strojništvo Univerze v Ljubljani so obranili svojo doktorsko disertacijo:

- dne *2. novembra 2015* **Aleš ZALAZNIK** z naslovom: »Vpliv temperature na velikociklično utrujanje izdelkov v frekvenčnem prostoru« (mentor: prof. dr. Marko Nagode);

V doktorski disertaciji je predstavljena metodologija, ki že v zgodnjih fazah razvoja izdelka omogoča hitro in enostavno napoved utrujenostne poškodbe izdelka v frekvenčnem prostoru ob sočasnem upoštevanju vpliva spremembe temperature obremenjevanja. Predlagana metoda je razvita iz originalne Dirlikove metode. Primerna je za ocenjevanje velikosti utrujenostne poškodbe izdelka, ki je podvržen stacionarnim normalno porazdeljenim obremenitvam s srednjo vrednostjo nič. Metoda sloni na teoriji velikocikličnega utrujanja materiala.

Pri napovedi utrujenostne poškodbe izdelka morajo biti poznane vhodne obremenitve, ki so podane v obliki temperaturno odvisnih gostot močnostnih spektrov napetostne obremenitve in temperaturne zgodovine obremenitev. S pomočjo spektralne analize se iz gostot močnostnih spektrov obremenitve najprej ocenijo spektralni momenti in parametri frekvenčnih širin. V naslednjem koraku sledi določitev porazdelitve amplitud obremenitvenih ciklov. S pomočjo utežnih faktorjev je popisan vpliv temperaturne obremenitve, ki deluje na izdelek. Ob poznanih temperaturno odvisnih S-N krivuljah in ob uporabi Palmgren-Minerjevega pravila se lahko oceni velikost utrujenostne poškodbe.

Predlagana metoda je bila teoretično, eksperimentalno validirana in podkrepljena še z numeričnimi simulacijami. Metoda se je izkazala kot uspešna pri napovedovanju velikosti utrujenostne poškodbe;

- dne *5. novembra 2015* **Janez SUŠNIK** z naslovom: »Lasersko pretaljevanje in oplastenje aluminijevih zlitin« (mentor: izr. prof. dr. Roman Šturm, somentor: prof. dr. Janez Grum);

V doktorskem delu je predstavljeno lasersko pretaljevanje in oplastenje aluminijeve zlitine AlSi12CuNiMg s pulznim Nd:YAG laserjem. V prvem delu smo s postopkom laserskega pretaljevanja povečali trdoto površinskega sloja. Optimalne pogoje laserskega pretaljevanja smo določili z merjenjem značilnosti modificiranega površinskega sloja, kot so trdota, mikrostruktura, dimenzije, hrapavost. S pomočjo teh značilnosti smo določili optimalno absorpcijsko sredstvo za povečanje absorptivnosti laserske svetlobe v površino aluminijeve zlitine. Temperaturo vzorca, njegovo ukrivljenost in zaostale napetosti smo merili, da bi določili optimalni način vodenja laserskega snopa po površini vzorca.

V drugem delu smo raziskali vpliv naknadnega staranja na velikost trdote in zaostalih napetosti v pretaljenem površinskem sloju. Vplivne parametre staranja smo ovrednotili s statistično analizo variance. Ugotovili smo dodaten dvig trdote in ugodno znižanje zaostalih napetosti zaradi staranja.

V tretjem delu smo za še dodatno izboljšanje trdote v površinskem sloju aluminijeve zlitine le to oplastili s keramičnima sestavinama TiC in TiB_2. Na osnovi mikrostrukturnih analiz, meritev trdote in dimenzij oplastenega sloja smo za pulzni Nd:YAG laser majhnih moči določili optimalne pogoje laserske obdelave. S pomočjo nanoindeterja smo določili tudi modul elastičnosti in koeficient trenja oplastenega sloja ter lasersko pretaljenega sloja;

- dne *9. novembra 2015* **Tomaž ŠUKLJE** z naslovom: »Toplotni odziv prilagodljivih gradnikov fasadnega ovoja stavb« (mentor: prof. dr. Sašo Medved, somentor: izr. prof. dr. Ciril Arkar);

V delu je numerično in eksperimentalno raziskan toplotni odziv mikrometeorološkega sloja, ki ga oblikujeta ozelenjena ali razvita bionična fasada in osnovni fasadni gradnik stavbe. Toplotni odziv mikrometeorološkega sloja je opredeljen v obliki parametričnih modelov, ki so bili izdelani na osnovi razvitih numeričnih modelov ter metode inverznega modeliranja. Vsi parametrični modeli so validirani z eksperimenti v naravnem in laboratorijskem okolju. Predstavljen je postopek, s katerim je, na osnovi inverznega modeliranja, mogoče za poljubno ozelenjeno ali bionično fasado opredelili virtualne toplotno-fizikalne in optične lastnosti. Tako nadomestimo mikrometeorološki sloj s homogenim slojem, kar omogoča vrednotenje dinamičnega toplotnega odziva prilagodljivih gradnikov fasadnega ovoja stavb s standardiziranimi metodami. Raziskan in parametrično ovrednoten je tudi vpliv mikrometeorološkega sloja na nestacionarni prenos toplote v ovoju stavbe in mikroklimatskih razmer v urbanem okolju. Dokazano je, da ozelenjene in bionične fasade bistveno vplivajo na blaženje toplotnega otoka v mestih.

*

Na Fakulteti za strojništvo Univerze v Mariboru je obranil svojo doktorsko disertacijo:

● dne *20. novembra 2015* **Andrej CUPAR** z naslovom: »Razvoj metodologije za razvrstitev zaznavnih ploskev pri oblikovanju izdelkov« (mentor: izr. prof. dr. Zoran Stjepanović);

Disertacija obravnava problematiko vrednotenja površja. To površje je lahko elementarna ploskev, ploskev, sestavljena iz elementarnih ploskev, 3D skenogram ali mrežni model. Uporabljamo izraz zaznavne ploskve, ki predstavljajo površje, ki ključno vpliva na zaznavanje izdelka z uporabniškega vidika. Pri tem nas ne zanima estetska vrednost teh ploskev, ampak metodologija, ki omogoča vrednotenje.

Za ta namen smo predstavili metodologijo n×n, ki se izvaja hkrati v programskem okolju Rhinoceros (RH) in dodatku Grasshopper (GH). V GH je nastavljena procedura z uporabo standardnih gradnikov GH. Rezultat te analize je najprej n×n matrika, v kateri so zbrane n×n razdalje, ki so v nadaljevanju normirane in zbrane v normalizirani n×n matriki. Iz normirane n×n matrike izhajajo izračuni za lastnosti CASP. S temi štirimi lastnostmi lahko ovrednotimo vsako površje; označujejo pa ukrivljenost, pospešenost, simetrijo in proporcionalnost. Rezultati so primerljivi samo pri elementarnih ploskvah. Elementarna ploskev je ploskev, ki ima podobno ukrivljenost ali predstavlja oblikovno značilnost ali del oblikovne značilnosti. Pri kompleksnih ali sestavljenih ploskvah lahko rezultate primerjamo samo za določen tip objektov; na primer samo za obraze. Sicer kompleksne ploskve segmentiramo in razdelimo na elementarne.

Prikazanih je tudi nekaj vmesnih razvojnih faz, v katerih smo uporabili drugačne analitične postopke, ki smo jih na koncu opustili. Vseeno lahko z njimi analiziramo geometrijo, le povezati in aktivirati je potrebno ustrezne gradnike v GH; kot je recimo izris in analiza linije prereza ali prerez dveh prostorskih teles.

V eksperimentalnem delu je zbranih nekaj praktičnih primerov uporabe CASP in postopki za izboljšavo dizajnerskega procesa za nadaljnjo uporabo. Prikazana je uporaba CASP metode na sedežih profesionalnih tekmovalnih koles, na računalniških miškah, na obrazih, na zadku avtomobila Tushek & Spigel – TS 600 in na obrezilnih orodjih za industrijske stiskalnice. Predstavljena je metoda, ki smo jo poimenovali DEGI, kjer uporabimo obstoječo geometrijo in jo vgradimo v nov izdelek.

*

ZNANSTVENO MAGISTRSKO DELO

Na Fakulteti za strojništvo Univerze v Mariboru je z uspehom zagovarjal svoje magistrsko delo:

● dne *5. novembra 2015* Damijan ŠVAJNCER BUTINAR z naslovom: »Kriteriji za presojo okvirjev terenskih motociklov« (mentor: izr. prof. dr. Stanislav Pehan)

Information for Authors

All manuscripts must be in English. Pages should be numbered sequentially. The manuscript should be composed in accordance with the Article Template given above. The maximum length of contributions is 10 pages. Longer contributions will only be accepted if authors provide juastification in a cover letter. For full instructions see the Information for Authors section on the journal's website: http://en.sv-jme.eu .

SUBMISSION:

Submission to SV-JME is made with the implicit understanding that neither the manuscript nor the essence of its content has been published previously either in whole or in part and that it is not being considered for publication elsewhere. All the listed authors should have agreed on the content and the corresponding (submitting) author is responsible for having ensured that this agreement has been reached. The acceptance of an article is based entirely on its scientific merit, as judged by peer review. Scientific articles comprising simulations only will not be accepted for publication; simulations must be accompanied by experimental results carried out to confirm or deny the accuracy of the simulation. Every manuscript submitted to the SV-JME undergoes a peer-review process.

The authors are kindly invited to submit the paper through our web site: http://ojs.sv-jme.eu. The Author is able to track the submission through the editorial process - as well as participate in the copyediting and proofreading of submissions accepted for publication - by logging in, and using the username and password provided.

SUBMISSION CONTENT:

The typical submission material consists of:

- A **manuscript** (A PDF file, with title, all authors with affiliations, abstract, keywords, highlights, inserted figures and tables and references),
- Supplementary files:
  - a **manuscript** in a WORD file format
  - a **cover letter** (please see instructions for composing the cover letter)
  - a ZIP file containing **figures** in high resolution in one of the graphical formats (please see instructions for preparing the figure files)
  - possible **appendicies** (optional), cover materials, video materials, etc.

Incomplete or improperly prepared submissions will be rejected with explanatory comments provided. In this case we will kindly ask the authors to carefully read the Information for Authors and to resubmit their manuscripts taking into consideration our comments.

COVER LETTER INSTRUCTIONS:

Please add a **cover letter** stating the following information about the submitted paper:

1. Paper **title**, list of **authors** and their **affiliations**.
2. **Type of paper**: original scientific paper (1.01), review scientific paper (1.02) or short scientific paper (1.03).
3. A **declaration** that neither the manuscript nor the essence of its content has been published in whole or in part previously and that it is not being considered for publication elsewhere.
4. State the **value of the paper** or its practical, theoretical and scientific implications. What is new in the paper with respect to the state-of-the-art in the published papers? Do not repeat the content of your abstract for this purpose.
5. We kindly ask you to suggest at least two **reviewers** for your paper and give us their names, their full affiliation and contact information, and their scientific research interest. The suggested reviewers should have at least two relevant references (with an impact factor) to the scientific field concerned; they should not be from the same country as the authors and should have no close connection with the authors.

FORMAT OF THE MANUSCRIPT:

The manuscript should be composed in accordance with the Article Template. The manuscript should be written in the following format:

- A **Title** that adequately describes the content of the manuscript.
- A list of **Authors** and their **affiliations**.
- An **Abstract** that should not exceed 250 words. The Abstract should state the principal objectives and the scope of the investigation, as well as the methodology employed. It should summarize the results and state the principal conclusions.
- 4 to 6 significant **key words** should follow the abstract to aid indexing.
- 4 to 6 **highlights;** a short collection of bullet points that convey the core findings and provide readers with a quick textual overview of the article. These four to six bullet points should describe the essence of the research (e.g. results or conclusions) and highlight what is distinctive about it.
- An **Introduction** that should provide a review of recent literature and sufficient background information to allow the results of the article to be understood and evaluated.
- A **Methods** section detailing the theoretical or experimental methods used.
- An **Experimental section** that should provide details of the experimental set-up and the methods used to obtain the results.
- A **Results** section that should clearly and concisely present the data, using figures and tables where appropriate.
- A **Discussion** section that should describe the relationships and generalizations shown by the results and discuss the significance of the results, making comparisons with previously published work. (It may be appropriate to combine the Results and Discussion sections into a single section to improve clarity.)
- A **Conclusions** section that should present one or more conclusions drawn from the results and subsequent discussion and should not duplicate the Abstract.
- **Acknowledgement** (optional) of collaboration or preparation assistance may be included. Please note the source of funding for the research.
- **Nomenclature** (optional). Papers with many symbols should have a nomenclature that defines all symbols with units, inserted above the references. If one is used, it must contain all the symbols used in the manuscript and the definitions should not be repeated in the text. In all cases, identify the symbols used if they are not widely recognized in the profession. Define acronyms in the text, not in the nomenclature.
- **References** must be cited consecutively in the text using square brackets [1] and collected together in a reference list at the end of the manuscript.
- **Appendix(-icies)** if any.

SPECIAL NOTES

Units: The SI system of units for nomenclature, symbols and abbreviations should be followed closely. Symbols for physical quantities in the text should be written in italics (e.g. *v*, *T*, *n*, etc.). Symbols for units that consist of letters should be in plain text (e.g. ms^{-1}, K, min, mm, etc.). Please also see: http://physics.nist.gov/cuu/pdf/sp811.pdf .

Abbreviations should be spelt out in full on first appearance followed by the abbreviation in parentheses, e.g. variable time geometry (VTG). The meaning of symbols and units belonging to symbols should be explained in each case or cited in a **nomenclature** section at the end of the manuscript before the References.

Figures (figures, graphs, illustrations digital images, photographs) must be cited in consecutive numerical order in the text and referred to in both the text and the captions as Fig. 1, Fig. 2, etc. Figures should be prepared without borders and on white grounding and should be sent separately in their original formats. If a figure is composed of several parts, please mark each part with a), b), c), etc. and provide an explanation for each part in Figure caption. The caption should be self-explanatory. Letters and numbers should be readable (Arial or Times New Roman, min 6 pt with equal sizes and fonts in all figures). Graphics (submitted as supplementary files) may be exported in resolution good enough for printing (min. 300 dpi) in any common format, e.g. TIFF, BMP or JPG, PDF and should be named Fig1.jpg, Fig2.tif, etc. However, graphs and line drawings should be prepared as vector images, e.g. CDR, AI. Multi-curve graphs should have individual curves marked with a symbol or otherwise provide distinguishing differences using, for example, different thicknesses or dashing.

Tables should carry separate titles and must be numbered in consecutive numerical order in the text and referred to in both the text and the captions as Table 1, Table 2, etc. In addition to the physical quantities, such as *t* (in italics), the units [s] (normal text) should be added in square brackets. Tables should not duplicate data found elsewhere in the manuscript. Tables should be prepared using a table editor and not inserted as a graphic.

REFERENCES:

A reference list must be included using the following information as a guide. Only cited text references are to be included. Each reference is to be referred to in the text by a number enclosed in a square bracket (i.e. [3] or [2] to [4] for more references; do not combine more than 3 references, explain each). No reference to the author is necessary.

References must be numbered and ordered according to where they are first mentioned in the paper, not alphabetically. All references must be complete and accurate. Please add DOI code when available. Examples follow.

Journal Papers:

Surname 1, Initials, Surname 2, Initials (year). Title. Journal, volume, number, pages, DOI code.

[1] Hackenschmidt, R., Alber-Laukant, B., Rieg, F. (2010). Simulating nonlinear materials under centrifugal forces by using intelligent cross-linked simulations. *Strojniški vestnik - Journal of Mechanical Engineering,* vol. 57, no. 7-8, p. 531-538, DOI:10.5545/sv-jme.2011.013.

Journal titles should not be abbreviated. Note that journal title is set in italics.

Books:

Surname 1, Initials, Surname 2, Initials (year). Title. Publisher, place of publication.

[2] Groover, M.P. (2007). *Fundamentals of Modern Manufacturing*. John Wiley & Sons, Hoboken.

Note that the title of the book is italicized.

Chapters in Books:

Surname 1, Initials, Surname 2, Initials (year). Chapter title. Editor(s) of book, book title. Publisher, place of publication, pages.

[3] Carbone, G., Ceccarelli, M. (2005). Legged robotic systems. Kordić, V., Lazinica, A., Merdan, M. (Eds.), Cutting Edge Robotics. Pro literatur Verlag, Mammendorf, p. 553-576.

Proceedings Papers:

Surname 1, Initials, Surname 2, Initials (year). Paper title. Proceedings title, pages.

[4] Štefanić, N., Martinčević-Mikić, S., Tošanović, N. (2009). Applied lean system in process industry. *MOTSP Conference Proceedings*, p. 422-427.

Standards:

Standard-Code (year). Title. Organisation. Place.

[5] ISO/DIS 16000-6.2:2002. *Indoor Air – Part 6: Determination of Volatile Organic Compounds in Indoor and Chamber Air by Active Sampling on TENAX TA Sorbent, Thermal Desorption and Gas Chromatography using MSD/FID.* International Organization for Standardization. Geneva.

WWW pages:

Surname, Initials or Company name. Title, from http://address, date of access.

[6] Rockwell Automation. Arena, from *http://www.arenasimulation.com,* accessed on 2009-09-07.

EXTENDED ABSTRACT:

When the paper is accepted for publishing, the authors will be requested to send an **extended abstract** (approx. one A4 page or 3500 to 4000 characters). The instruction for composing the extended abstract are published on-line: http://www.sv-jme.eu/information-for-authors/ .

COPYRIGHT:

Authors submitting a manuscript do so on the understanding that the work has not been published before, is not being considered for publication elsewhere and has been read and approved by all authors. The submission of the manuscript by the authors means that the authors automatically agree to transfer copyright to SV-JME when the manuscript is accepted for publication. All accepted manuscripts must be accompanied by a Copyright Transfer Agreement, which should be sent to the editor. The work should be original work by the authors and not be published elsewhere in any language without the written consent of the publisher. The proof will be sent to the author showing the final layout of the article. Proof correction must be minimal and executed quickly. Thus it is essential that manuscripts are accurate when submitted. Authors can track the status of their accepted articles on http://en.sv-jme.eu/.

PUBLICATION FEE:

Authors will be asked to pay a publication fee for each article prior to the article appearing in the journal. However, this fee only needs to be paid after the article has been accepted for publishing. The fee is 240.00 EUR (for articles with maximum of 6 pages), 300.00 EUR (for articles with maximum of 10 pages), plus 30.00 EUR for each additional page. The additional cost for a color page is 90.00 EUR. These fees do not include tax.

Strojniški vestnik -Journal of Mechanical Engineering
Aškerčeva 6, 1000 Ljubljana, Slovenia,
e-mail: info@sv-jme.eu

9 770039 248001
ISSN 0039-2480

http://www.sv-jme.eu

Contents

Papers